Technische Universität Braunschweig

Mingjie Wang

Experimental determination of cross sections for ionization of DNA constituents by proton impact

Dissertation
Braunschweig 2017

Berichte aus dem **Institut für Elektrische Messtechnik und Grundlagen der Elektrotechnik**

Band 56

Hrsg. Prof. Dr. Meinhard Schilling

Experimental determination of cross sections for ionization of DNA constituents by proton impact

Von der Fakultät für Elektrotechnik, Informationstechnik, Physik
der Technischen Universität Carolo-Wilhelmina zu Braunschweig

zur Erlangung des Grades eines Doktors

der Ingenieurwissenschaften (Dr.-Ing.)

genehmigte Dissertation

von Mingjie Wang

aus Hangzhou

eingereicht am: 13.04.2017

mündliche Prüfung am: 20.06.2017

1. Referent: Prof. Dr. Meinhard Schilling
2. Referent: Prof. Dr. Jochen Litterst
3. Referent: Dr. Hans Rabus

Druckjahr: 2017

Dissertation an der Technischen Universität Braunschweig,
Fakultät für Elektrotechnik, Informationstechnik, Physik

Abstract

This thesis presents a complete set of proton-impact ionization cross section data of DNA constituents determined at the Physikalisch-Technische Bundesanstalt (PTB). The cross section data describe the probabilities for the ionization of gas-phase tetrahydrofuran, pyrimidine and trimethyl phosphate that are structural analogues to the base, sugar, and phosphate residue of the DNA, respectively. Total, single-differential and double-differential ionization cross sections were determined, whereby the differential description refers to the energy or angular dependence of electron emission. Double-differential cross sections were measured for impact energies between 75 keV and 3000 keV over an angular range between 15° and 150° in 15° intervals. Both single-differential and total ionization cross sections were derived by integration of the measured double-differential cross sections.

The measurements of double-differential cross sections were carried out using a crossed-beam arrangement in a high-vacuum chamber. The proton beam, which perpendicularly crosses an effusive gas jet target of DNA constituents inside the chamber, was generated either by the 3.75 MV Van de Graaff accelerator of the PTB ion accelerator facility (PIAF) or a newly developed 155 kV ion accelerator. In the measurement a newly constructed electron spectrometer was used to detect the secondary electrons produced by proton collisions with the target molecules. The energy of the secondary electrons was selected by a hemispherical electron energy analyzer, which was mounted on a turntable to allow the spectrometer to rotate around the axis of the gas jet. Hence, the energy spectra could be recorded at defined observation angles with respect to the proton beam. These spectra were converted into absolute cross section values via a normalization procedure based on previously published absolute electron-impact cross section data.

The experimentally determined cross section data were compared to various theoretical approaches, such as the classical Rutherford formula and several quantum-mechanical methods, namely the Hansen-Kocbach-Stolterfoht model (HKS), a semi-empirical model based on the dielectric response function (DRF) and an ab initio model based on the first Born approximation with corrected boundary conditions (CB1). The comparison to the CB1 and DRF models shows a good agreement with experimental data in a broad range of emission angles and energies of the secondary electrons. All proton-impact ionization cross sections obtained in this work have been integrated in the GEANT4-DNA and PTra track structure codes to improve the estimation of radiation damage to DNA in ion-beam cancer therapy.

Kurzfassung

In dieser Arbeit wurde ein vollständiger Satz von Wechselwirkungsquerschnitten für die Ionisierung von DNA-Bestandteilen durch Protonen mit einem neu entwickelten experimentellen Aufbau an der Physikalisch-Technischen Bundesanstalt (PTB) bestimmt. Die ermittelten Wirkungsquerschnitte beschreiben die Wahrscheinlichkeiten für die Ionisierung von Tetrahydrofuran, Pyrimidin und Trimethyl-phosphat in der Gasphase, die strukturelle Analoga der Nukleobasen, der Deoxyribose und des Phosphatrestes der DNA sind. Bestimmt wurden totale, einfach-differenzielle und doppelt-differenzielle Ionisierungsquerschnitte, wobei die differenzielle Beschreibung sich auf die energie- und winkelabhängige Elektronenemission bezieht. Doppelt-differenzielle Ionisierungsquerschnitte wurden für Stoßenergien zwischen 75 keV und 3000 keV über einen Winkelbereich zwischen 15° und 150° in 15° Intervallen gemessen. Sowohl die einfach-differenziellen als auch die totalen Ionisierungsquerschnitte wurden durch Integration aus den gemessenen doppelt-differenziellen Wirkungsquerschnitten abgeleitet.

Die Messungen der doppelt-differenziellen Ionisierungsquerschnitte wurden in einer Hochvakuumkammer durchgeführt, in der ein Protonenstrahl einen effusiven Gasstrahl von DNA-Bestandteilen kreuzt. Der Protonenstrahl wurde hierbei entweder durch einen neu aufgebauten 155 kV-Beschleuniger oder durch den 3.75 MV-Van-de-Graaff-Beschleuniger der PTB Ionenbeschleunigeranlage (PIAF) erzeugt. Bei der Messung wurde ein neu aufgebautes Elektronenspektrometer verwendet, um die bei Protonenkollisionen mit den Gasmolekülen erzeugten Sekundärelektronen zu detektieren. Die Energie der Sekundärelektronen wurde durch einen halbkugelförmigen Elektronenenergieanalysator selektiert, der auf einem Drehtisch so montiert war, dass das Spektrometer um die Achse des Gasstrahls gedreht werden konnte

und damit die Energiespektren bei definierten Beobachtungswinkeln im Bezug auf den Protonenstrahl aufgenommen werden konnten. Aus diesen Spektren wurden die Absolutwerte der Ionisierungsquerschnitte durch ein Normierungsverfahren unter Bezugnahme auf zuvor veröffentlichte absolute Daten von Elektronenstoß-Wirkungsquerschnitten bestimmt.

Die experimentell ermittelten Ionisierungsquerschnitte wurden mit verschiedenen theoretischen Verfahren verglichen. Diese umfassten die klassische Rutherford-Formel und mehrere quantenmechanische Methoden, wie das Hansen-Kocbach-Stolterfoht-Modell (HKS), ein semi-empirisches Modell auf der Grundlage der dielektrischen Antwortfunktion (DRF), sowie ein ab-initio Modell basierend auf der ersten Born-Näherung mit korrigierten Randbedingungen (CB1). Der Vergleich mit CB1- und DRF-Modell zeigt eine gute Übereinstimmung mit den experimentellen Daten in einem breiten Bereich von Emissionswinkeln und Energien der Sekundärelektronen. Die in dieser Arbeit erhaltenen Protonenstoß-Ionisierungsquerschnitte wurden mittlerweile in die GEANT4-DNA- und PTra-Spurstrukturcodes aufgenommen, um die Vorhersage von Strahlenschäden an der DNA in der Ionenstrahl-Krebstherapie zu verbessern.

Table of Contents

Symbols

B_i

Binding energy of i-th subshell electron

B_x, B_y, B_z

Orthogonal component of the magnetic field

E_R

Rydberg energy

F_{Salin}

Salin factor

I_{FC}

Beam current measured with the Faraday cup

I_x, I_y, I_z

Currents flowing through the Helmholtz coils

K_{CRR}

Retard ratio of the electron energy analyzer

K_n

Knudsen number, characterizes the type of flow

L_{int}

Length of interaction zone

L_x, L_y, L_z

Side lengths of the square Helmholtz coil

M_p

Mass of the incident particle

N_{int}

Target number in the interaction zone

R_0

Mean radius of the electron energy analyzer

T_g

Gas temperature in the vacuum chamber

T_p

Primary energy of the incident particle

T

Reduced primary energy of the incident particle

V_0

Potential between the outer and inner hemispheres of the electron energy analyzer

V_{int}

Volume of the interaction zone

W_{BE}

Electron energy at the binary-encounter peak

W_p

Pass energy of the electron energy analyzer

W

Kinetic energy of the secondary electron

Z_p

Nuclear charge of the incident particle

Ω

Solid angle into which the secondary electrons are ejected

$\dot{N}_p$

Number of incident particles per time

$\dot{N}_s$

Number of secondary electrons per time

$\dot{S}_{\text{pump}}$

Nominal pumping speed of the turbomolecular pump

ℓ_t

Length of the tube

M_{gas}

Mass of the target gas molecules

$\eta(W)$

Detection efficiency of the electron energy analyzer

γ_t

Tube's aspect ratio

$\hbar$

Reduced Planck constant

λ_r

Mean free path of the vapor molecules in the reservoir

λ_t

Mean free path for the interaction of a projectile with the gas jet

μ_0

Magnetic constant

ρ_t

Number density of target particles

σ_{ion}

Total ionization cross section

θ_{BE}

Polar ejection angle at the binary-encounter peak

θ

Polar angle of ejected secondary electron

ϑ

Polar scattering angle of the incident particle

a_0

Bohr radius

d_m

Molecular diameter

d_t

Diameter of the nozzle

d_x, d_y, d_z

Separations of the Helmholtz coil pairs

e

Elementary charge

k_B

Boltzmann constant

k_I

Collection efficiency of the Faraday cup

m_e

Mass of the electron

n_v

Number of valence shell electrons

p_g

Gas pressure in the vacuum chamber

p_r

Backing pressure

v_e

Velocity of the secondary electron

v_p

Velocity of the incident particle

$\mathrm{d}\sigma_{\mathrm{el}}/\mathrm{d}W$

Differential elastic scattering cross section

$\mathrm{d}\sigma_{\mathrm{ion}}/\mathrm{d}W$

Single-differential ionization cross section

$\mathrm{d}^2\sigma_{\mathrm{ion}}/\mathrm{d}W\mathrm{d}\Omega$

Double-differential ionization cross section

$\mathrm{d}^2\sigma_{\mathrm{mod}}/\mathrm{d}W\mathrm{d}\Omega$

Parameterized double-differential ionization cross section

Abbreviations

B1

First Born (approximation)

BEA

Binary encounter approximation

CAE

Constant analyzer energy (operation mode)

CB1

Boundary-corrected first Born (model)

CDW

Continuum distorted wave (model)

CDW-EIS

Continuum distorted wave-eikonal initial state (model)

CRR

Constant retard ration (operation mode)

CTMC

Classical trajectory Monte Carlo (model)

DC

Direct current

DDCS

Double-differential cross section (for ionization)

DelCS

Differential elastic scattering cross section

DNA

Deoxyribonucleic acid

DRF

Dielectric response function

DSB

Double strand break

ECC

Electron capture to the continumm (process)

ELF

Energy loss function

FWHM

Full width at half maximum

GUI

Graphical user interface

HKS

Hansen-Kocbach-Stolterfoht (model)

I/O

Input / output

IBCT

Ion-beam cancer therapy

IP-camera

Internet-protocol camera

PIAF

The PTB ion accelerator facility

PTra

Track structure simulation code, developed at the PTB

PWBA

Plane wave Born approximation

PY

Pyrimidine

RNA

Ribonucleic acid

SCEE

Single-center electron emission

SDCS

Single-differential cross section (for ionization)

SOBP

Spread out Bragg peak

SSB

Single strand break

TCEE

Two-center electron emission

THF

Tetrahydrofuran

TICS

Total ionization cross section

TMP

Trimethyl phosphate

USB

Universal serial bus

List of Tables

List of Figures

Chapter 1

Introduction

The interaction of charged particles with atoms and molecules of target material has received considerable interest over the past few decades [1]. During an atomic collision by ion impact, the elastic and inelastic processes can take place. In the energy region considered in this work (several tens of keV to a few MeV), the most dominant processes are excitation of the target, electron capture or loss of the projectile, and the ejection of one or more electrons from the target. The last process is referred to as ionization, where the projectile transfers enough energy to a bound target electron to overcome the binding energy and releases the secondary electron from the target with a kinetic energy. This is essentially a result of the interactions of a three-body system, which comprises the target electron, the projectile ion and the ionized target atom.

The probability for a specific interaction process to occur is described by the interaction cross section [2]. The process of secondary electron emission, described by the ionization cross section, is the subject of this work. Fundamental knowledge of the ionization cross sections originates from the pioneering work of Rutherford [3] from the view of classical mechanics. The Rutherford formula [3] provides an analytic solution for a two-body problem, where the projectile ion interacts with a free electron initially at rest. In subsequent years, several theoretical approaches of varying complexity have been developed [1, 4–9]. Experimentally, Blauth [10], Moe and Petsch [11] measured the energy distribution of low-energy electrons emitted from gases by ions. Later, Kuyatt and Jorgensen Jr. [12], and Rudd and Jorgensen Jr. [13] started systematic measurements of differential electron emission, focusing on energy and angular distributions of ejected electrons [14, 15]. Furthermore, experiments of electron emission have been performed by Stolterfoht [16] and Toburen [17] using projectiles with incident energies in the order of a few MeV. In summary, various theoretical and experimental investigations of ionization cross sections on simple targets, such as rare gases, water vapor and hydrocarbon molecules, have been conducted and reviewed by Rudd et al. and Stolterfoht et al. for projectile ions as protons [18] and other heavy particles [1], respectively, covering incident energies from a few keV to several MeV.

Electron emission has been used in numerous studies to provide detailed information about the atomic structure and collision dynamics. The application of ion collisions in the medical field has been attracting more attention in recent years, where protons and other charged particles are used for radio-therapeutic treatment in ion-beam cancer therapy. Compared to conventional radiation therapy with electrons or photons, ion beams have the advantage of a deeper and sharper maximum of deposited energy in the tissue at the end of their trajectories. This sharp maximum in the so called depth-dose curve is known as the Bragg peak. Ion beams can therefore deliver high doses at well controlled depths and are thus suited for treating deep-seated tumors.

In the Bragg peak region, the ionization yields reach a maximum as the secondary electrons, which are produced in large numbers, typically have mean free paths from nanometers to several micrometers. These distances correspond in length to a fraction of the cell nucleus enclosing the deoxyribonucleic acid (DNA) molecule, which is usually regarded as a sensitive target to radiation damage. Hence, secondary electrons are responsible for highly-localized energy deposition events on the nanometric scale. Electron emission therefore plays a key role in the mechanism of ion-induced damage to biological targets.

To model the physical interactions of ion beams with the medium, track structure Monte Carlo simulations are often used [19, 20]. In these simulations, the history of the particle track, i.e. individual interactions of the projectiles and their secondaries with molecules of the medium, is modeled using corresponding interaction cross section data as input information. A critical point for the reliability of Monte Carlo simulation codes is the availability of accurate interaction cross sections [21], of which ionization cross sections are particularly relevant due to the release of secondary electrons. Generally, track structure simulations in a biological medium are performed using cross section data of water, as an approximate model for the DNA in a cellular environment. As significant differences were found for the estimated radiation damage in living tissue based on cross sections of water [22], a more realistic representation for DNA constituents is of interest. Hence, the focus of the targets studied in ion collision shifted from water to more complex, biologically relevant molecules. Theoretically, several methods based on the

first Born approximation have been developed to calculate ionization cross sections for biological targets such as nucleobases [23–27]. However, the experimental data for interaction of ions with DNA biomolecules are still incomplete. For example, previous experimental studies to date have covered only the nucleobases for proton collisions at limited energies [28–31].

The aim of this thesis is to present an experimental determination of cross sections for ionization of DNA constituents by proton impact. The motivation of this work is to provide reliable input information about the interaction cross sections which are required by the Monte Carlo track structure simulation as well as to extend the knowledge of electron emission mechanisms to complex biological targets for a wider range of primary energies. In the present work, the measurements were performed using a crossed-beam arrangement to determine double-differential cross sections, which provide a detailed description of both energy and angular distribution of emitted electrons for incident protons of specific energy. The biological targets investigated represent individual DNA constituents, such as pyrimidine, tetrahydrofuran and trimethyl phosphate, which are the respective structural analogues to the nucleobases, sugar, and phosphate of the DNA. An intensive study was made for tetrahydrofuran by carrying out measurements for proton energies ranging from 75 keV to 3000 keV. For pyrimidine and trimethyl phosphate, the measurements were performed only for protons in the Bragg-peak region (75 keV–135 keV).

This thesis begins with a short instruction, followed by a theoretical background and description of fundamental information in chapter 2. The experimental setup, including the beamline and the spectrometer, are described in chapter 3 and the procedure of the data analysis is presented in chapter 4. Several theoretical models are briefly introduced in chapter 5. The experimental results are reported in chapter 6, where they are compared to theoretical calculations. Discrepancies between the measurements and well-known cross sections of small targets (e.g. hydrogen, water, and hydrocarbon molecules) are also discussed. A scaling property of ionization cross sections is also investigated. Finally, conclusions and an outlook for further work are given in chapter 7.

Chapter 2

Background and fundamentals

2.1 Radiation effects on DNA targets

2.1.1 Ionizing radiation — Bragg peak and track structure simulation

Ion-beam cancer therapy (IBCT) has become a powerful and effective technique for the treatment of cancer, especially for deep-seated local tumors [32]. The main reason for using ion-beams in radiotherapy is their favorable depth-dose profiles, with a sharp maximum at the end of their paths referred to as Bragg peak. This characteristic peak is named after Bragg and Kleeman [33] who investigated the slowing down of particles moving through air. Many years later, the IBCT was realized in the 1950s as the application of protons in therapy after the proposition by Wilson [34] in 1946.

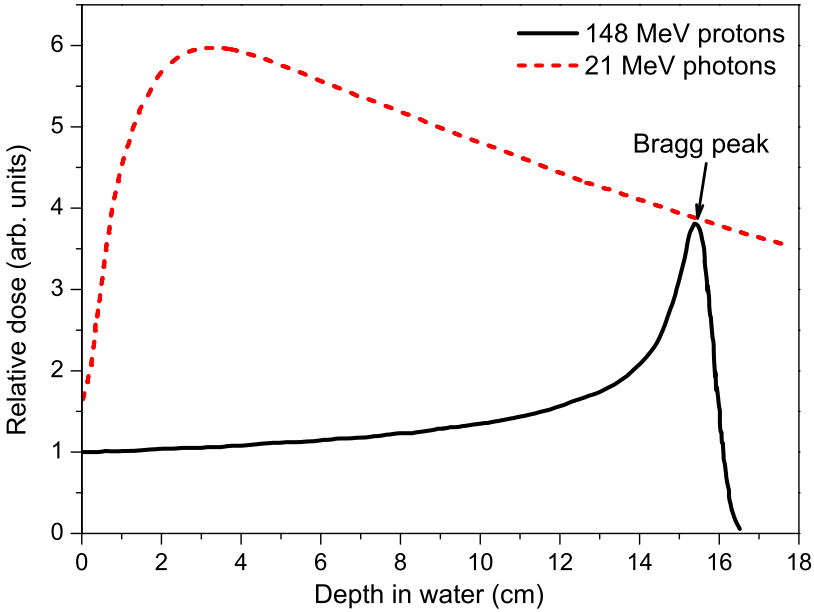

Figure 2.1 Comparison of depth-dose distributions in water for energetic protons (black solid line) and photons (red dashed line). Protons show an nearly inverse dose profile labeled as Bragg peak. The figure originates from Fokas et al. [35].

When a charged particle passes through a medium, it ionizes or excites atoms or molecules of the medium and thereby deposits energy along its trajectory. The energy deposited per unit mass is the absorbed dose. A comparison of depth-dose distributions in water for protons and photons, is displayed in figure 2.1. For photons with energy of several MeV as they are used in conventional radiotherapy, the dose builds up within the first few centimeters, and then drops exponentially with the increasing depth. This is due to the production of secondary electrons by photo-absorption or Compton scattering. These electrons, generally, have sufficient energy to travel a range of several millimeters through water. In contrast, the proton beam disposes an inverse depth-dose distribution, peaking at the end of its track (labeled as Bragg peak) and afterwards falling off to zero.

The Bragg peak occurs because the interaction cross sections of the incident ions with the medium increase as the kinetic energy of ions decreases. The interactions mainly produce secondary electrons with low energies, which have sub-millimeter ranges [36]. The location of this peak can be precisely adjusted to the desired depth in the tissue by varying the initial energy of the incident ions. However, the width of a single Bragg peak is too narrow to treat most tumors which have a typical volume of a few centimeters in size [37]. Therefore, several Bragg peaks have to be superimposed at staggered depths for a therapeutic radiation distribution, which is defined as the spread out Bragg peak (SOBP) [38]. As a result, IBCT allows a deposition of high doses into desired tumor volumes, concentrating the radiation damage to the cancer cells, and simultaneously sparing the healthy tissue around.

In the Bragg peak region, the energy of the charged particles, initially in the order of several hundred MeV, decreases very strongly, e.g. it declines to around 80 keV for protons [39]. Ions of such energies have a high linear energy transfer, consequently, the density of ionization events is enhanced, and accordingly, most of the ion-induced biodamage is expected to take place at those energies. Generally, the analytical description of the particle's propagation in a medium is very complex and therefore approximations are used. For microscopic target volumes such as the DNA, track structure simulations using Monte Carlo codes are well suited to numerically solve the particle transport problem, as the interactions of ions and secondary particles with a medium are of stochastic nature [22]. In such codes, a particle track

contains the information on positions and types of successive interactions of a single incident particle and its secondaries with a medium [22]. Hence, the detailed histories of the particle's track are followed interaction by interaction through the medium. The modeling of individual interactions is accomplished by the use of interaction cross sections, which describe the probability of a specific interaction, e.g. ionization (see section 2.2.1, page 14). The physical interactions of the ionizing particle with DNA molecules take place at times less than femto seconds (10^{-15} s) [40]. Within this time scale, simulation codes like GEANT4-DNA [41] or PTra [42] are available to provide the physical track structure.

2.1.2 The organic target — structure, damage and modeling of the DNA molecule

As an essential component in living cells, the DNA carries the genetic information. Within this function the important role is played by the specific DNA structure. In this section, a brief instruction is given to the DNA structure, including its damage induced by ionizing radiation as well as its modeling in track structure simulation.

Basically, DNA consists of two antiparallel chains of nucleotides twisted into a double-stranded helix [43]. As depicted in figure 2.2, a nucleotide molecule is a monomer unit which is composed of a phosphate group, a deoxyribose sugar, and one of four types of nucleobases. The nucleotides are joined to one another with a backbone structure which is composed of alternating phosphate and deoxyribose residues. Along the backbone, one of four nucleobases, which are classified into two types, either pyrimidine (cytosine and thymine) or purine (adenine and guanine) is attached to the deoxyribose. The nucleobases of both opposing strands are hydrogen bonded according to base pairing rules, which are, the adenine is always connected to thymine and cytosine to guanine. Within such a sequence of nucleobases along a DNA strand, the genetic information is encoded. Water molecules are also present within the cell nucleus and can be considered as an integral part of the DNA structure [22, 44].

The DNA molecule cannot be measured directly in gaseous volumes, which is necessary for a single-collision condition (see section 3.4.3, page 42). Hence, analog molecules of DNA constituents are usually used in the

experiment. Three objective biomolecules are involved in this work, namely pyrimidine (PY, $C_4H_4N_2$), tetrahydrofuran (THF, C_4H_8O) and trimethyl phosphate (TMP, $C_3H_9PO_4$), which are structural analogues to the base, the sugar and the phosphate residue of DNA, respectively. The molecular structure of a DNA segment is schematically shown in figure 2.2. PY is a precursor of the nucleobases cytosine and thymine. Both of them contain the ring structure of PY. Similarly, THF is a precursor of the deoxyribose. In combination with THF, TMP provides a representation of the trimethyl ester of the phosphoric acid. In this case, the DNA backbone can be modeled by alternating THF and TMP molecules.

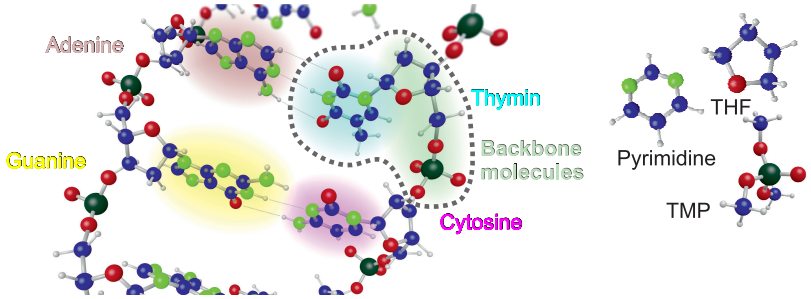

Figure 2.2 Chemical structure of a DNA segment containing the four nucleobases: adenine, guanine, thymine and cytosine. Different atoms are color coded spheres: hydrogen—small grey, carbon—blue, oxygen—red, nitrogen—green, phosphorus—large dark green. The inset illustrates the chemical structure of the investigated molecules and their similarity to the DNA constituents. The figure originates from Bug [22].

As Nikjoo [40] indicated in his work, the cell nucleus and in particular the DNA molecule is the primary target of damage for ionizing radiation. Direct ionizations or excitations of DNA molecules may lead to a rupture of chemical bonds and the generation of DNA lesions [45]. These processes are considered as direct damage to the DNA molecule, whereas the indirect damage is referred to as a chemical attack to the DNA by secondary species, for instance the water radicals or hydrated electrons, which are formed along the track of the incident particles. Generally, there are three major types of DNA damage induced by ionizing radiation [45]: single strand breaks (SSB)

are referred to as a damage of a backbone molecule on one strand; double strand breaks (DSB) are defined as two SSB on opposite strands within ten base pairs; and base damage.

To simulate the direct damage on the DNA along particle track, particularly near the Bragg peak, the experimental cross sections for the interactions between the incident particles and the molecules comprising the medium are required as input data [22]. As water may occupy more than 80% of the total volume in the cell structure [46], it is commonly used as a default medium to describe living tissue. The ionization cross sections of water have been experimentally investigated in the past [47–50]. Several estimations of DNA damage based on water cross section data have been performed, where a simplified linear DNA segment is modeled in the form of a cylinder filled with water [51] or water vapor [52].

Ion-induced DNA damage can only be evaluated from the damage to the constituents of the DNA, if the cross section data of these constituents are available. An advantage of using these data is that the strand breaks can be distinguished from base damage. While there is a significant amount of literature for water molecules, only a few experimental data have recently been published for complex biological molecules like DNA or ribonucleic acid (RNA) constituents. For example, Tabet et al. [28] presented the total ionization cross sections of nucleobases (adenine, cytosine, thymine and uracil) at proton energies below 150 keV. Iriki et al. and Itoh et al. reported the data of adenine [29, 31] and uracil [30] for proton energies of 0.5 MeV, 1 MeV and 2 MeV. To the best of our knowledge, reliable experimental cross section data for biologically relevant molecules are still largely lacking but are required due to steadily increasing applications of IBCT.

For the DNA analogues as used in this work, various cross sections have been measured at the PTB previously, containing differential elastic and total scattering cross sections [53–55] for electron impact, as well as fragmentation cross sections [56, 57]. Those data sets, together with the proton-impact ionization cross sections obtained in this work, have been integrated in the GEANT4-DNA [41] and PTra [42] track structure codes to improve the prediction of radiation damage to the DNA in a more realistic manner.

2.2 Secondary electron emission from ion-atom collision

2.2.1 Introduction to ionization cross sections

Among all interaction mechanisms along the ion trajectories, direct ionization is generally the most probable process for ion collisions at impact velocities above the orbital velocities of a target electron [18]. Various ionization mechanisms, such as binary-encounter collisions, soft collisions and Auger processes, lead to the ejection of secondary electrons. The secondary electrons emitted during such processes often carry enough energy for further ionization of nearby molecules, initiating an avalanche effect, which results in the energy transfer through ionization of sensitive biological targets, such as the DNA molecule. In fact, the ionization process and the subsequent cascade of secondary electrons account for the majority of ion-induced radiation damage to DNA [58].

Although high-energy electrons are capable of producing further ionizations, which may cause target fragmentation on the molecular level [56], it was shown that low-energy electrons can also induce single or double strand breaks in DNA via dissociative electron attachment [59, 60]. In order to reach a precise understanding of ionization processes in biological matter, not only the number of secondary electrons is relevant, but also their spatial and energetic distributions are of primary importance.

Monte Carlo track structure simulations, which calculate the spatial distribution of the ion and electron interactions, require a set of total and differential interaction cross sections. The total ionization cross section (TICS) is needed to estimate the probability of secondary electron emission due to ion collision. This quantity σ_{ion}, which has the dimension of an area, describes the ratio of the flux of secondary electrons $\dot{N}_s$ to the flux of incident particles $\dot{N}_p$ [2]:

$$\sigma_{\mathrm{ion}} = \frac{\dot{N}_s}{\dot{N}_p L_{\mathrm{int}} \rho_t}, \tag{2.1}$$

where ρ_t is the number of the target particles per volume (number density) and L_{int} is the length of beam path from which the ejected electrons are collected, e.g. the length of the interaction zone (see section 3.4.2, page 40).

Information about the angular and energy distributions of emitted electrons is contained in the double-differential cross section (DDCS) for ionization, so that the probability of further secondary electron interactions can be modeled.

The DDCS quantifies the ratio of the flux of secondary electrons $\dot{N}_s$, ejected into an element of solid angle $\Delta\Omega$ at a polar angle θ within interval ΔW around energy W, to the flux of incident particles $\dot{N}_p$ [2]

$$\frac{\mathrm{d}^2\sigma_{\mathrm{ion}}}{\mathrm{d}W\mathrm{d}\Omega} = \frac{\dot{N}_s}{\dot{N}_p L_{\mathrm{int}}\rho_t \Delta W \Delta\Omega}. \tag{2.2}$$

For some purposes, only the information of the energy spectrum is relevant. In this case, the integration of DDCS over the full solid angle leads to the single-differential cross section (SDCS) for ionization

$$\frac{\mathrm{d}\sigma_{\mathrm{ion}}}{\mathrm{d}W} = \int \frac{\mathrm{d}^2\sigma_{\mathrm{ion}}}{\mathrm{d}W\mathrm{d}\Omega}\,\mathrm{d}\Omega = 2\pi \int_0^{\pi} \frac{\mathrm{d}^2\sigma_{\mathrm{ion}}}{\mathrm{d}W\mathrm{d}\Omega}\sin\theta\,\mathrm{d}\theta, \tag{2.3}$$

where the differential solid angle is given as a function of emission angle $\mathrm{d}\Omega = 2\pi\sin\theta\mathrm{d}\theta$.

The total ionization cross section is obtained by integrating of the SDCS over all secondary electron energies from 0 to W_{max}

$$\sigma_{\mathrm{ion}} = \int_0^{W_{\mathrm{max}}} \frac{\mathrm{d}\sigma_{\mathrm{ion}}}{\mathrm{d}W}\,\mathrm{d}W, \tag{2.4}$$

where W_{max} is the maximum energy of ejected electrons.

2.2.2 Processes of secondary electron emission

2.2.2.1 Center picture

Ion-atom collisions can be categorized into two qualitatively different types: a soft (or glancing) collision (see section 2.2.2.3, page 18) and a hard (or binary) collision [18]. The description of ionizing collisions is basically a three-body problem, which can be solved by reducing this problem to a corresponding two-body problem or to a sequence of two-body interactions [1]. Rutherford [3] has given the fundamental work of the two-

body problem where only the interaction between the projectile and the target electron is considered (see section 5.2, page 83). Another approach to solve the three-body problem is using the first-order perturbation theory [1]. For example, Bethe [6] has used the first Born approximation to describe electron emission from ion impact (see section 5.3, page 86). In this section, the major mechanisms of secondary electron emission from ion-atom collisions are briefly summarized.

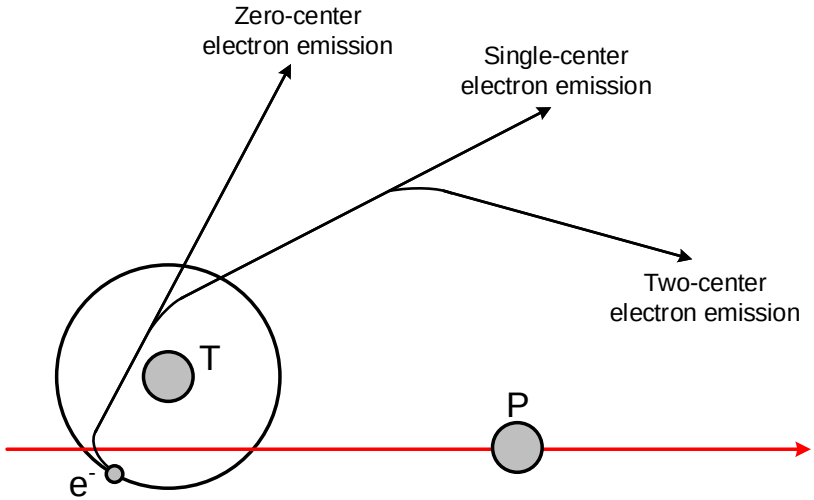

Figure 2.3 Mechanisms for electron emission associated with different trajectories. The collision partners are labeled as: e^-—target electron, T—target nuclei, P—projectile nuclei. The figure originates from Stolterfoht et al. [1].

Instead of considering the complex dynamics of a many-body system, Stolterfoht et al. [1] has introduced an intuitive picture of viewing electron emission in terms of collision centers of the outgoing electron. Formally, the formation of a center involves an strong interaction of the nucleus with the active electron, i.e. the one which is ionized during the collision. In terms of center concepts, different trajectories of the secondary electron emitted after the interaction with an incident ion are schematically displayed in figure 2.3. The target electron is initially bound to the target atom, then ionized during a

collision with the incident ion, and may be finally scattered by the Coulomb field of one or both collision partners. Generally, there are three different cases: the outgoing electron is unaffected, which corresponds to a binary collision without center (zero-center case); the outgoing electron is affected by the nuclear field of the target, which corresponds to an electron emission involving a single target center; and the outgoing electron is affected by the field of both the target and projectile, which corresponds to an electron emission involving two centers [1]. These mechanisms will be discussed separately in the following sections.

2.2.2.2 Binary-encounter electron emission

Hard collisions between projectiles and target electrons correspond to a two-body interaction in which the influence of the target nucleus to the outgoing electron can be neglected. This relatively simple ionization process is quoted as binary-encounter electron emission. The binary-encounter electron emission depicted in figure 2.3 is referred to as zero-center case. The outgoing electron follows a straight-line trajectory which is not significantly affected by the nuclear field of either the target or the projectile [18].

For projectiles whose velocities are larger than the mean velocity of the target electron before the collision, a prominent peak is observed in the angular distribution of the DDCS. This structure is known as the binary-encounter peak, which is a direct consequence of large energy and momentum transfers from the incident particles to the ejected electrons in binary collisions. The location of this peak at the emission angle θ_{BE} can be predicted according to the energy and momentum conservation rules [18]

$$\theta_{\mathrm{BE}} = \arccos \sqrt{\frac{M_p W}{4 m_e T_p}}, \tag{2.5}$$

where M_p and T_p are the mass and incident energy of the projectile, while m_e and W are the mass and kinetic energy of the secondary electron. Equation 2.5 applies for a free electron initially at rest and indicates a delta-function at the ejection angle θ_{BE}, which is not larger than 90°. In reality, the binary peak is a distribution with a specific width as the target electron has an initial velocity distribution [1], which is individual for an electron bound in a specific molecular orbital.

For relatively slow projectiles, the high-velocity components in the initial velocity distribution of bound electrons mainly cause electron emission at backward angles larger than 90°. This behavior can be considered as a binary-encounter process where the characters of the incident ion and the target electron are exchanged [1]. In this reversed binary-encounter process, the momentum direction of the bound electron may be strongly affected by the nuclear field of the slow projectile. As a result, the electrons are elastically scattered by the projectile and may leave the target atom at backward directions. Hence, the inverse binary encounter process is treated as a projectile-center case.

2.2.2.3 Single-center electron emission

In the single-center electron emission (SCEE) process, the target nucleus is generally treated as an interaction center. The influence of the target nucleus increases with decreasing velocity of the outgoing electron. In particular, electrons emitted from soft collisions are attributed to a single-center treatment [1], as for such an electron, its interaction with the nucleus, to which the electron was initially bound, may be stronger than the interaction with the projectile. This occurs for soft collisions where the energy and momentum transfers are small and the projectile velocity is high, so that the interaction time of the projectile and the target is negligible. In fact, for fast projectiles, e.g. protons with energies above 1 MeV, most collisions are of this type [18]. Thus, electrons produced in soft collisions form the pronounced structure in the DDCS spectrum at low electron energies.

In the example of figure 2.3, the outgoing electron from SCEE process, which is firstly involved in a binary-encounter event, afterwards is scattered by the Coulomb field of the target nucleus which forms a center. Besides that, another example of a SCEE process is the backscattering of fast electrons in the target center. These electrons considered are those which experience hard collisions with typical transferred energies up to a few hundred eV. In this energy range, other mechanism, for example the inverse binary-encounter process has smaller probability, so that the backscattering by the target center dominates and therefore contributes to the electron emission at backward directions.

2.2.2.4 Two-center electron emission

The ionization process associated with both centers of collision partners, i.e. the target nucleus and the projectile, is quoted as two-center electron emission (TCEE). Recalling figure 2.3, the outgoing electron from a TCEE process is affected by the superposition of the Coulomb fields of both the target and the projectile nuclei.

Since SDCS are governed by the binary-encounter and soft collisions which are zero-center or single-center phenomena, the two-center effects are mostly noticeable in the spectrum of DDCS. An outstanding example of TCEE is provided by the electron capture to the continuum (ECC) process. In this case, the outgoing electron has a velocity similar to that of the projectile after the collision. In most cases, the energy of the electron is low enough to "feel" the target center, but additionally, it is attracted by the leaving projectile. Consequently, it is essentially focused by the Coulomb field of the projectile nucleus in the forward direction, and additionally, attracted by the leaving projectile.

2.2.2.5 Auger electron emission and other process

In general, the probability for an ion projectile to interact with a target electron in outer orbital shell is higher than the probability of the interaction with an inner shell electron. The interaction of the projectile with a core electron generates a hole in the inner shell of the target atom. The inner-shell vacancy may be filled by an electron from an outermore shell with a higher energy level, resulting in a release of energy. This excess in energy can be imparted to another electron which is subsequently ejected from the same atom. This ionization process is called Auger electron emission, deriving its name from the effect discovered by Auger [61]. In large molecules, a cascade of Auger electrons can leave the molecule in a highly charged state.

The kinetic energy of an Auger electron corresponds to the difference between the transferred energy in the initial ionization leading to the inner-shell vacancy and the binding energy for the outer shell from which the Auger electron is ejected. Thus, the Auger peak appears in certain energy regions of the electron spectrum. However, despite its appearance in the experimental data (see section 6.3, page 102), Auger electron emission is not considered in the ionization cross section. The ionization cross section only describes

the probability for a direct ionization of the target atom or molecule by the projectile. Hence, Auger electron emission is also not included in theoretical calculations.

Under the experimental conditions assumed in this work, e.g. single-collision by proton impact (see section 3.4.2, page 40), the probabilities for other complex ionization processes are expected to be negligible. For instance, the contribution of multiple ionization to the ionization cross section is small in proton collisions. It amounts to a few percentage of TICS for noble gases at 3 MeV and rapidly decreases towards lower proton energies [62].

Another inelastic process is the electron capture to a bound state of the projectile. Differing from the ECC process, it leads to a reduction of the projectile's charge. In the case of hydrogen atoms, these would subsequently produce no signal to the measured ion current. Therefore, no measurements were taken to quantify the electron capture process in the setup (see section 3, page 21) and it was not accounted for in the analysis.

Chapter 3

Setup of the experiment

3.1 Introduction

The experimental cross section data reported in this work are measured for structural analogues to the nuclei bases, the sugar and the phosphate residue of the DNA backbone (see section 2.1.2, page 11), namely pyrimidine (PY, $C_4H_4N_2$), tetrahydrofuran (THF, C_4H_8O) and trimethyl phosphate (TMP, $C_3H_9PO_4$), respectively. The measurements of double-differential cross sections (DDCS) were performed using a crossed-beam arrangement built up in a high-vacuum chamber. The measuring geometry of this experiment can be seen in figure 3.1 where the primary particle beam crosses the effusive gas jet perpendicularly.

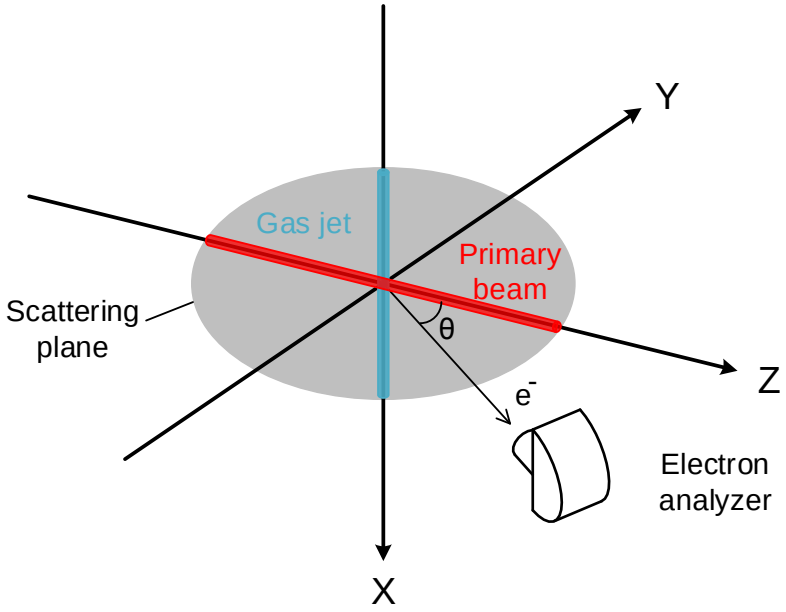

Figure 3.1 Secondary electron spectroscopy experiment using a crossed-beam arrangement.

The proton beam was generated by a 3.75 MV Van de Graaff accelerator (see section 3.3, page 34) or a 155 kV self-constructed (see section 3.2, page 24) accelerator for primary energies above or below 300 keV, respec-

tively. The overlap of the beam and the gas jet (see section 3.4.1, page 37) defines the interaction zone (see section 3.4.2, page 40), where the center is considered as the origin of the geometry. The X and Z axes are defined by the direction of the gas jet and the primary beam respectively. The Y-axis is perpendicular to both and the YZ-plane is the scattering plane. Information about the energetic and angular distributions of secondary electrons is contained in the DDCS, which is independent of the azimuthal angle and depends only on the polar angle θ due to the symmetry of the measuring geometry. The secondary electrons ejected from the interaction zone at a fixed angle θ relative to the beam direction are detected and analyzed with respect to their kinetic energy W using an electron analyzer (see section 3.5, page 43), which was mounted on a turntable such that it could be rotated around the axis of the gas jet.

3.2 Beamline — the laboratory accelerator

A new low-energy ion accelerator has been recently constructed at the PTB for collision experiments between biologically relevant molecules and protons with energies up to 155 keV. This energy range is particularly important due to the peak of the total ionization cross sections at a projectile energy of about 100 keV. The maximum energy transfer from the projectile to the target is commonly denoted as Bragg peak region (see section 2.1.1, page 9). Because perturbative theoretical approximations (see section 5.3, page 86) have limited validity in this energy range, experimental data are urgently required as benchmark. The same experimental setup was used in both the measurements of high proton energies at the Van de Graaff accelerator (see section 3.3, page 34) and the measurements with protons of energies close to the Bragg peak energy at the laboratory ion accelerator.

3.2.1 Beamline layout and components

Figure 3.2 shows the general layout of the low-energy ion accelerator beamline. The total length of the beamline was approximately 3 m. An IQE 12/38 extractor type ion source produced by SPECS GmbH was used to generate the protons from hydrogen gas. The primary energy of the ions was variable between 0.2 keV and 5 keV. With the accelerator the ion source was operated at its maximum energy of 5 keV. Protons were selected by the

mass-to-charge ratio using a Wien mass filter [63] downstream of the ionizer volume. The proton beam was then prepared by the focusing and deflection sections in the IQE 12/38 for further acceleration.

Two perpendicular deflectors operated with a voltage of up to 0.5 kV were used to align the beam with respect to the center of the accelerating stage. Each deflector was composed of two electrically deflecting plates mounted parallel to each other in vertical or horizontal direction. The 0.5 m-long accelerating stage consisted of 20 electrodes connected via a voltage divider circuit having a total resistance of 30 MΩ. The last electrode was connected to ground potential. The accelerating stage allowed tuning the primary energy over the range from 5 keV to 155 keV, where the energy resolution of 0.1% was estimated to be that of the power supply PNC150000 produced by Heinzinger GmbH. The ion source, the first deflector and the accelerating stage were contained in an electrically shielded cube at the high-voltage side of the beamline due to the applied high potential up to 155 kV and therefore inaccessible during the measurements for safety reasons.

A second deflector behind the accelerating stage steered the beam into the electrostatic quadrupole triplet which focused the beam horizontally and vertically by means of parabolic electrostatic fields. A third electrostatic deflector was located behind the quadrupole. The maximum voltages applied to the quadrupole triplet, the second and the third deflector were 5 kV, 1 kV and 1 kV respectively. The beam current could be measured with retractable Faraday cups after the first or before the third deflection stage.

The proton beam was collimated by three tantalum apertures with 5 mm, 3 mm and 5 mm in diameter, respectively. Instead of confining the beam, the purpose of the last aperture was to prevent electrons released from the middle aperture by proton impact to reach the interaction chamber. The apertures were mounted inside a differential pumping stage between the beamline and experimental chamber. The beam current on the central aperture was monitored. Another Faraday cup was positioned on the far side of the chamber to determine the proton current. For beam positioning, the proton current was maximized in this Faraday cup and minimized on the central aperture. The beam current i.e. beam intensity was regulated by adjusting both gas pressure and emission current of the filament in the ionizer

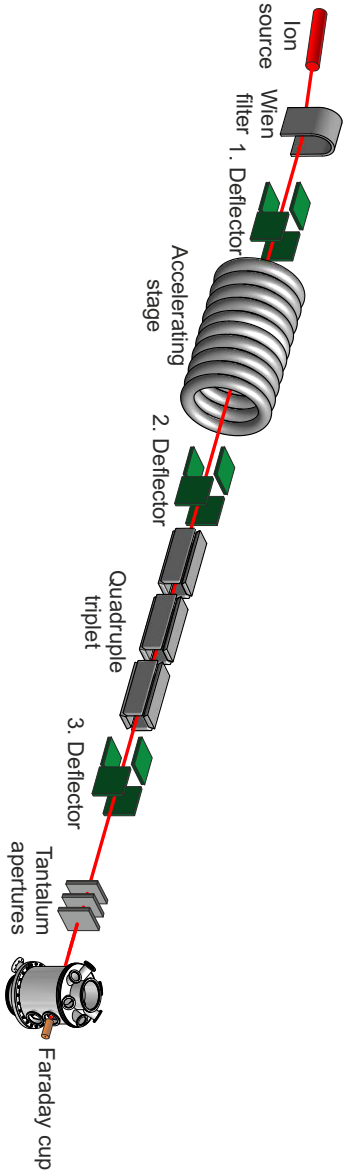

Figure 3.2 Sketch of the low-energy ion accelerator beamline.

volume at the ion source. A typical value of the proton current measured in the Faraday cup on the far side of the chamber was in the order of 20 nA during the experiments.

As the intensity of the proton beam could be reduced by the collimation, the deflecting and focusing of the beamline components were checked by means of a phosphor screen mounted between the third deflector and the collimation apertures. In this case, the proton beam was focused on this screen to check the spot size of the beam. The beam current at the Faraday cup located in front of the phosphors screen was also recorded. These results are summarized in table 3.1 for various proton energies.

Proton energy (keV)	Beam current (nA)	estimated spot size (mm × mm)
85	45	2×2
105	80	1×1
135	50	1×1
155	50	1×1

Table 3.1 Specification of the low-energy ion accelerator beamline for various proton energies.

3.2.2 Control system and instrumentation

A hardware and software system has been developed during this work to control the beamline of the low-energy ion accelerator. Figure 3.3 shows the front view of the beamline components and hardware instruments used in this control system. The three major tasks of this system are to set up the operating parameters of the ion source as well as those of the accelerator beamline and to monitor the ion beam. Comparing to commercial solutions, this control system can provide a cost-saving method to satisfy the specific requirements of the experiment. In this section, the design and the implementation of this control system are described.

3.2.2.1 Conceptual design

The control system was composed of the remote nodes and the controlling or monitoring consoles. Due to the high potential of up to 155 kV, it is not possible to access some components (e.g. the ion source at high-potential

(a) Ground side

(b) High-voltage side

Figure 3.3 Front view of the beamline components and related hardware instruments.

side) locally during the operation of the beamline. Thus, a remote control is required for this system. This was realized by connecting nodes and consoles to the PTB network, as shown in figure 3.4.

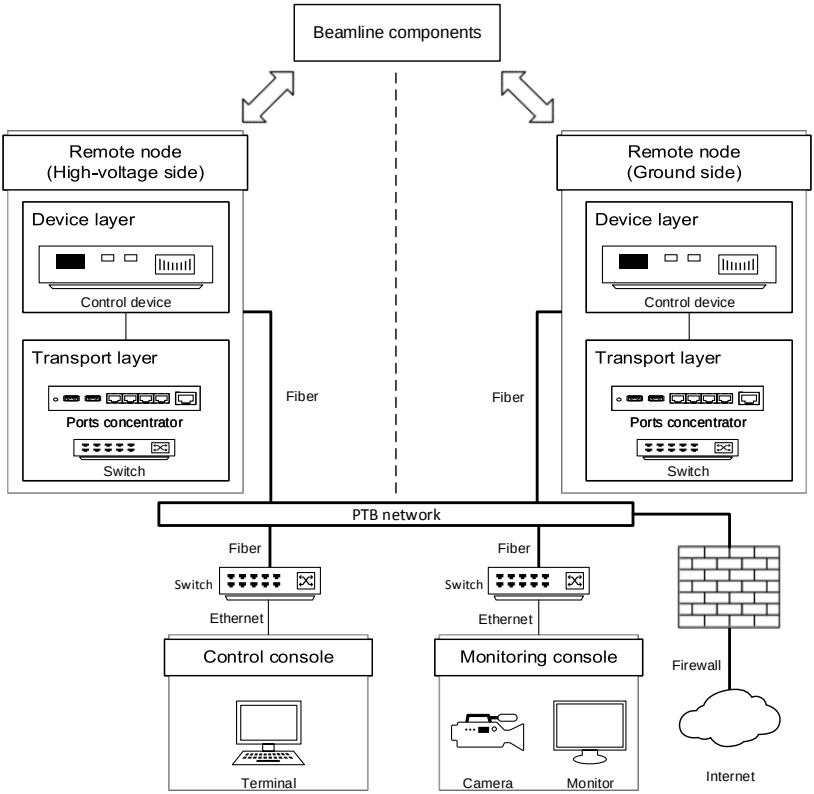

Figure 3.4 Architecture of the beamline control system.

The beamline components and their related instruments were separated into two remote nodes depending on which part of the beamline they were located, either high-voltage or ground side, as depicted in figure 3.3. Each remote node consisted of two layers: a transport layer and a device layer. In the device layer the beamline component was directly attached to its control device such as the power supplies.

There were several components installed on the beamline that need to be controlled individually. The first one was the ion source. As its control device, a power unit PU-IQE 12/38 was used to provide all voltages necessary for operation of the ion source. All operational parameters were controllable remotely via the RS-232 interface.

The other components to be controlled were the electrostatic deflectors and the quadrupole triplet. The operating voltages on the deflectors and the quadrupole triplet were provided respectively by power supply modules of the CPS and DPS series produced by iseg GmbH. These built-in modules were DC/DC converters. They were integrated in a modular crate ECH 128 manufactured by the same company. To enable the remote control for all modules plugged in, this crate was equipped with a digital interface, namely the Multichannel Interface Crate Controller.

The transport layer transmited the information between the remote node and the network. This layer was realized by the hardware composed of a ports-concentrator and a switch. The multiple peripheral devices in the upper layer were combined together by the concentrator, as shown in figure 3.4. Hereby, two models of ports-concentrator from the same manufacturer (Digi International Inc) were used, i.e. AnywhereUSB-TS and AnywhereUSB-14. The latter provided fourteen ports for USB connection. In addition, the AnywhereUSB-TS model also added four RS-232 serial ports wired in RJ-45 standard, allowing a mixing of USB and serial connections over the same network. The switch unit KGS-510F by KTI Networks Inc was used for establishing the Ethernet connections to the ports-concentrators, while its SFP-port was installed with a fiber transceiver to establish the uplink to the PTB network via a fiber connection.

The control console was implemented using a desktop computer running a Windows 7 operating system. Furthermore, a second monitor together with an IP-camera was used as monitoring console to check the beam optically by means of the phosphor screen during the beam alignment. The connection from the consoles to PTB network was carried out by the same switch KGS-510F described previously.

3.2.2.2 Software development and data communication

The software development for this control system was carried out by object-oriented programming, which was coded in C++ language using the ROOT library [64]. A brief overview of this program is shown in figure 3.5.

As figure 3.5 shows, each kind of control device is numbered for identification and abstracted as individual class. These classes inherit from their parent class "Device". Inside the class, the behaviors of control devices are managed by member functions, which can be classified into three groups: process-handler, error-handler and stream-handler. The process-handler defines the basic behavior such as connection or disconnection of the device, whereas the error-handler indicates the operating status of the device and provides diagnosis to the related error.

The stream-handler is designed to implement the communication to the control device via its remote interface (USB or RS-232 port). This is done by exchanging the input/output (I/O) data in the form of a common serial data stream between the remote node and the console across the network. In the view of console, the response from remote node (reading) is regarded as input data. The signal from the console (writing) such as user's request is defined as output data. The continuous data streaming is realized in this handler by running a thread with instructions for writing and reading.

Since the data communication to each control device is executed independently by the separate thread, the simultaneous data streaming for the connected devices can be archived by the multi-threading mechanisms. This procedure allows the program to continue data streaming in the case of partial failure. For example, if an unexpected error is detected at one of the controlled devices, the error-handler immediately requests the stream-handler to stop only this single failing I/O stream, however, the I/O streams of the other devices can keep operating.

A graphical user interface (GUI) on the control console was applied for the parameter settings and status displays. The implementation of this user interface was carried out by the class "GUI". The user interface is based on the event-driven programming [65] where the control flow of the program is indicated by a specific routine (event-handler) as a reaction to the bound signals (events) generated from the user or from the system. For instance, the refresh of the display window of the GUI is automatically triggered by

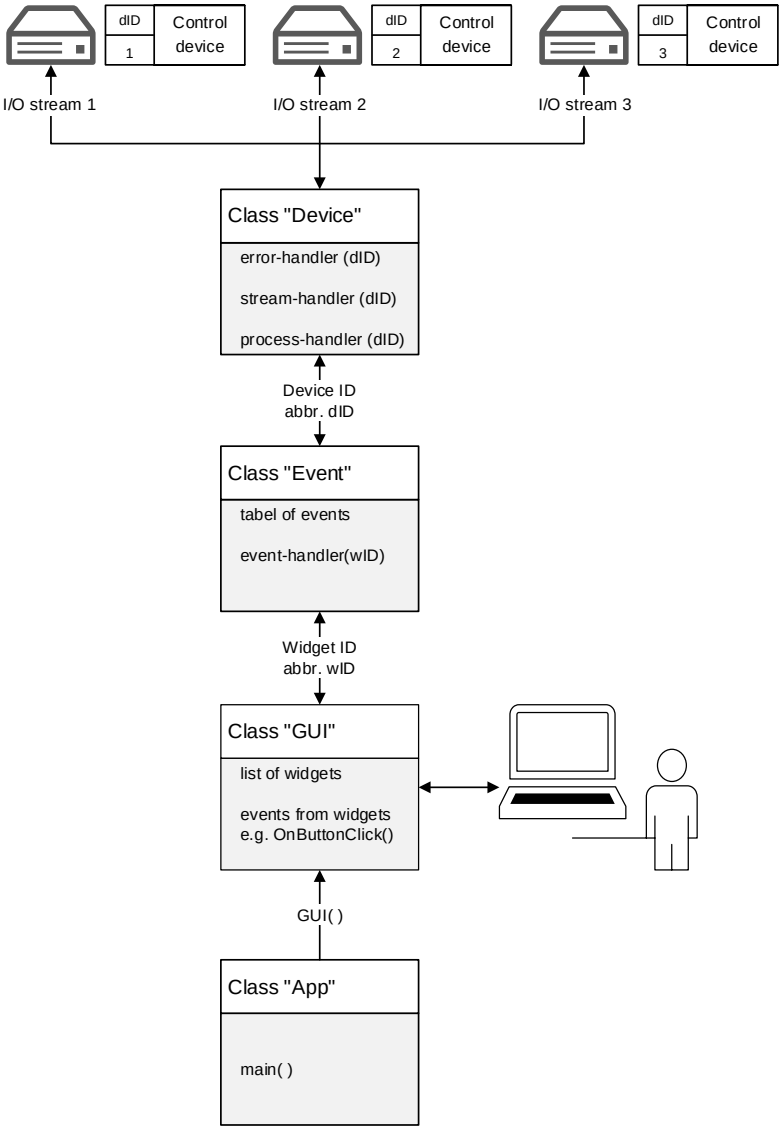

Figure 3.5 Data flow diagram of the control program.

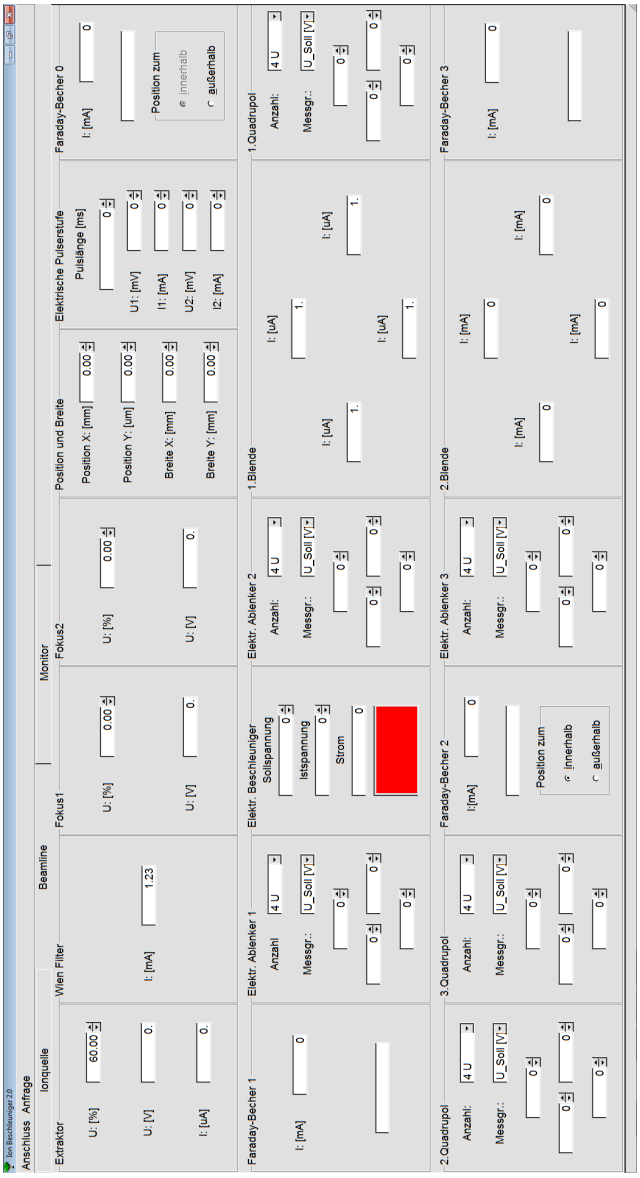

Figure 3.6 Screen shot of the second panel on the graphical user interface.

an internal timer as a system event in order to update the actual status of the operating beamline. On the other side, the events from the user such as the mouse clicks and keyboard presses are detected through the direct manipulation of the graphical control elements (widgets) such as the buttons or text boxes on the GUI. For example, a matching function is called for setting the voltage on the deflector after entering a value into the input box. The value range of the input box is limited. All of the widgets are grouped according to their relative tasks (see section 3.2.2, page 27) and placed into three corresponding panels, respectively. Figure 3.6 shows a screen shot of the panel for beam controlling on the GUI.

Another class "Event" was designed to deal with the different sorts of events produced from the user interface. To this end, the a series of methods, namely event-handlers, were implemented as member functions of this class. When one of the events takes place, according to the identification number (widgetID) of the involved widget, the matching event-handler is selected and then executed to call the related functions of the I/O stream that corresponds to the number (deviceID) of the target device. In other words, the widget event is connected to the correct function of the involved I/O stream by means of an event-handler.

The class "App" provides the entrance of the program, as the exclusive object of class "GUI" was created in the main function inside this class.

3.3 Beamline — the PTB Van de Graaff accelerator

The measurements for proton energies above 300 keV were carried out at the PTB ion accelerator facility (PIAF) using a Van de Graaff accelerator. The maximum energy of the proton beam was 3750 keV and the accuracy of the proton energy was ± 1 keV [66]. Figure 3.7 shows the electron spectrometer installed at a beamline in the experimental hall of the PIAF.

This accelerator facility was described in detail by Brede et al. [67]. In brief, the Van de Graaff accelerator was horizontally mounted and operated with pure Sulfur hexafluoride (SF_6) insulating gas. After leaving the Van de Graaff accelerator, the proton beam was focused by a quadruple doublet and enters a 90°-deflecting magnet. Afterwards via another switching magnet and quadruple doublets, the beam entered the experimental hall, where the vacuum vessel containing the electron spectrometer (see section 3.5, page 43)

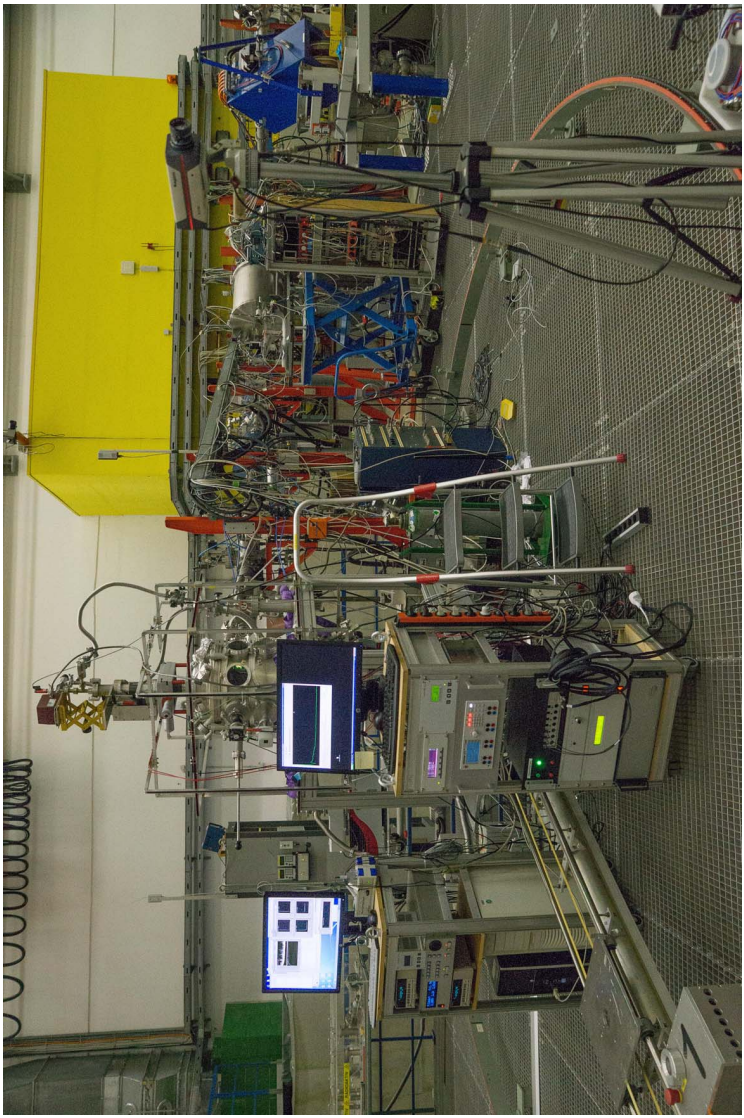

Figure 3.7 Photograph of the interaction chamber and measurement electronics installed at a beamline in the experimental hall of the PTB ion accelerator facility.

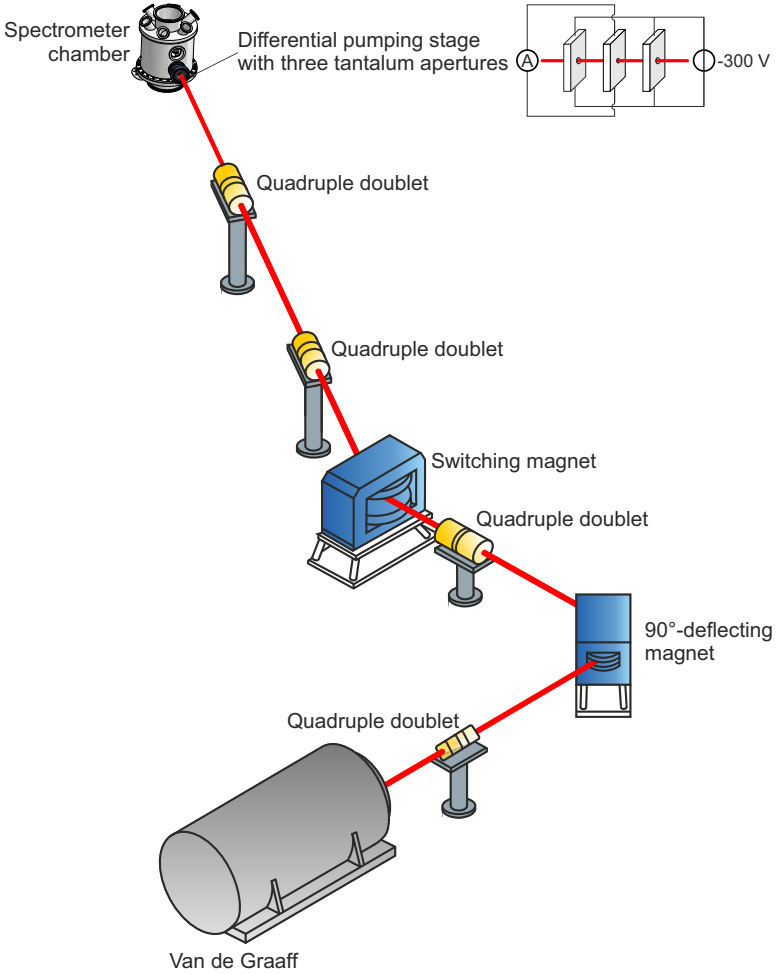

Figure 3.8 Sketch of the PTB 3.75 MV Van de Graaff accelerator beamline.

was attached to the beamline. This configuration allows to carry out a conventional crossed-beam experiment to investigate the cross sections of interested target gas. Figure 3.8 shows the general layout of the 3.75 MV Van de Graaff accelerator beamline.

As depicted in figure 3.8, a differential pumping stage was inserted as a buffer unit to prevent the flow of target gas into the high vacuum of the beamline. Inside, three tantalum apertures with diameters of 5 mm, 3 mm and 5 mm were used to collimate the beam. The current on the inner aperture was recorded by an electrometer to detect possible changes of the beam position. The outer apertures were biased to −300 V in order to suppress electron emission from the middle aperture such that only the direct current of protons hitting the middle aperture was recorded. A Faraday cup (not shown in figure 3.8) with an central aperture of 15 mm was placed on the far side of the spectrometer chamber in order to measure the beam current. Mechanical alignment of the Faraday cup, the apertures and the symmetry axis of the chamber was carried out using an optical telescope. The proton beam was aligned by maximizing the ratio of the current in the Faraday cup to the current on the central aperture. When optimally aligned, the current in the Faraday cup was in the order of 10^{-6} A, while the current onto the beam-confining aperture was in the order from 10^{-8} A to 10^{-7} A. The measured bias current on the Faraday cup in the absence of a beam was below 10^{-12} A.

3.4 Sample preparation and delivery

Collision experiments with complex biological molecules, such as those investigated in work, are difficult to accomplish in the gas phase due to the required preparation of well-characterized gas targets as well as the determination of the absolute number density of target molecules. Since the original DNA molecule may easily decompose when heated or vaporized or cannot be isolated, the three structural analogues previously mentioned (see section 2.1.2, page 11) were investigated.

3.4.1 Production and collimation of the effusive gas jet

The samples used in this work were purchased from Sigma-Aldrich company with specified purity 99%. At a room temperature of 28 °C all the samples were liquid, and their vapor pressures were high enough to achieve

a gas density in the interaction region which allowed the energy spectra of the secondary electrons to be recorded with sufficiently low uncertainty. As depicted in figure 3.9, a container filled with liquid sample was used as the vapor source. Each sample container was evacuated several times to remove any residual gas before introduction to the collision chamber. After pumping had stopped, the pressure in the container rose to the vapor pressures that were measured to be 250 mbar, 21 mbar and 3 mbar, for THF, PY and TMP, respectively.

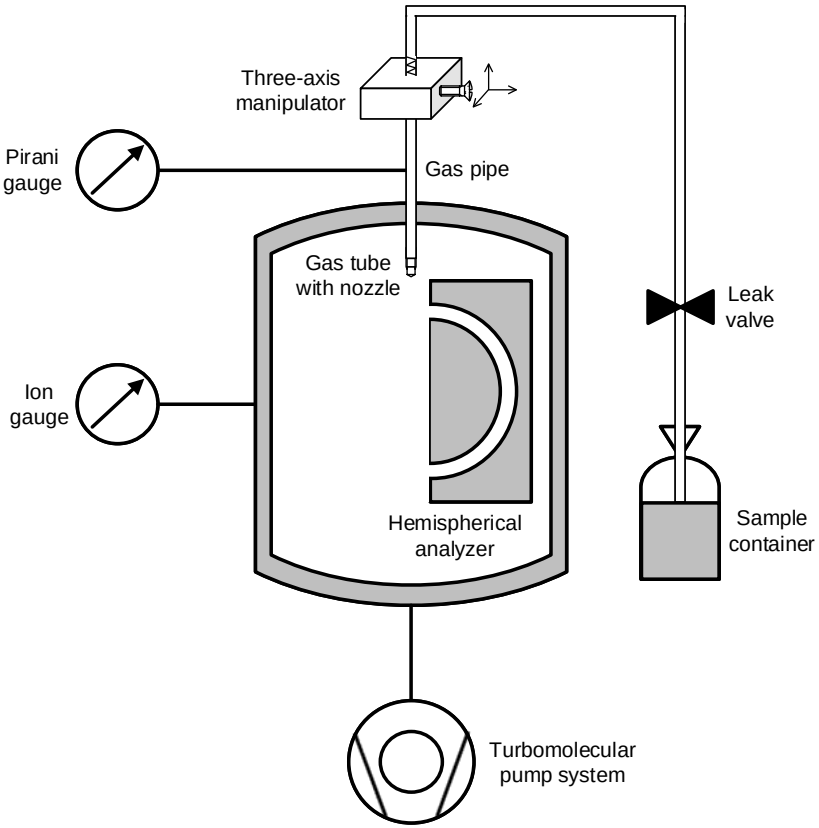

Figure 3.9 Schematic of the apparatus used for sample preparation and delivery.

The flow rate of the sample vapor was controlled by a leak valve. Along the gas pipe, a cylindrical tube with a length of 10 mm was used to generate an effusive gas jet of the target sample. This tube was aligned along the symmetry axis of the experimental chamber. At the tube's end the sample vapor was ejected into the chamber through a nozzle of 0.3 mm in diameter. The nozzle could be positioned vertically within ±10 µm (in the direction of the gas jet) and horizontally within ±2 µm (in the scattering plane) by means of a three-axis micrometer manipulator. The distance between the tip of the nozzle and the axis of the primary beam was typically set to about 2.5 mm.

A turbomolecular pump TCU 1600M purchased from Pfeiffer GmbH with a nominal pumping speed of 1380 l/s was used to create a vacuum in the order of 10^{-7} mbar inside the interaction chamber. This pressure was measured by an ion gauge PBR 260 of Pfeiffer GmbH. For the production of the gas jet, the sample vapor was introduced through the nozzle with a backing pressure of about 1 mbar measured by a pirani gauge TPR 280. As a result, the pressure in the chamber rose from 10^{-7} mbar to the order of 10^{-5} mbar.

The extent of collimation in the gas beam is dependent on the diameter of the nozzle d_t, the length of the tube ℓ_t and the pressure of vapor in the entrance reservoir, namely the backing pressure p_r [68]. The type of flow is characterized by the Knudsen number

$$K_n = \frac{\lambda_r}{d_t}, \tag{3.1}$$

where λ_r is the mean free path of the vapor molecules in the entrance reservoir. For collisions of identical particles, the quantity λ_r is given by Edelmann [69]:

$$\lambda_r = \frac{k_B \cdot T_{\text{temp}}}{\sqrt{2} \cdot \pi \cdot p_r \cdot {d_m}^2}, \tag{3.2}$$

where k_B is the Boltzmann's constant, T_{temp} is the temperature and d_m is the molecular diameter.

According to the work of Schmidt [70], the free molecular flow, where the collisions of molecules hitting the tube walls are much more significant than intermolecular collisions, prevails when $K_n > 0.3$. For the three samples

used in this work, these conditions of free molecular flow are fulfilled. Taking the THF for example, the molecular diameter d_m was estimated to be 2.86×10^{-10} m using the bond length of C=C and C=O [71]. With a pressure p_r of 1 mbar at room temperature $T_{\text{temp}} = 298$ K, the Knudsen number was $K_n = 0.376$. The tube's aspect ratio γ_t is defined as the ratio of the nozzle diameter d_t and the tube length ℓ_t, which gives

$$\gamma_t = \frac{d_t}{\ell_t}. \tag{3.3}$$

Here, the aspect ratio for the tube used in this experiment was 0.3 mm/10 mm = 0.03. As referred to the research of Seccombe et al. [68], the maximum collimation occurs when $\gamma_t \to 0$, and when $K_n > 0.3$, to hold the free molecular flow condition.

3.4.2 Geometry of the interaction zone

A relatively small and well-defined interaction zone of appropriate number density of target gas is required in the electron spectroscopy measurements. Figure 3.10 shows a geometric drawing for the perpendicular arrangement of the gas jet and proton beam in the interaction zone.

As can be seen from figure 3.10, the distance from the tip of the nozzle to the particle beam was estimated to be 2 mm. It was chosen to be large enough to avoid proton scattering on the nozzle. The gas jet ejected from the tip was estimated to be symmetric about the axis of the nozzle and to have a diameter of 1 mm in the interaction zone. The circular primary beam was estimated to be of 1 mm diameter. Thus, the length of the interaction zone was estimated to be 1 mm.

The number density in the interaction zone was determined using the calculation of Seccombe et al. [68] for the gas density arising from a single tube. For the simplicity of calculation, it was assumed that the interaction zone had a cylindrical geometry. The radius of the cylinder r_c was equal to the half length of the interaction zone and the length of the cylinder h_c was equal to the diameter of the incoming primary beam. Since the idealized interaction zone preserved the cylindrical symmetry around the nozzle axis, the variation of the number density around the nozzle axis could be neglected. Using the polar coordinate defined in figure 3.10, in which the origin is located

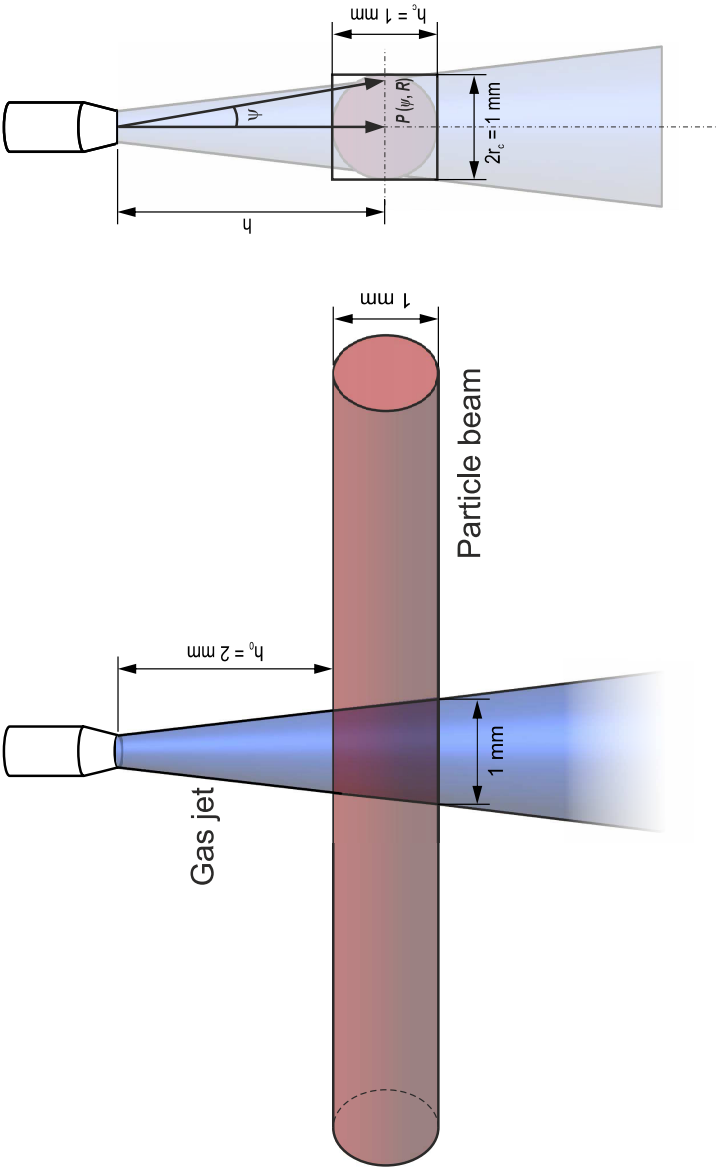

Figure 3.10 A geometry of the interaction zone with the primary particle beam and the gas jet.

at nozzle exit, the target number N_{int} in the interaction zone is given by [68]

$$N_{\text{int}} = 2\pi \int_{h_0}^{h_0+h_c} \int_0^{\chi} \frac{J(\psi)\tan(\psi)h}{\bar{c}R^2}\,\mathrm{d}\psi\mathrm{d}h, \tag{3.4}$$

where

$$R = \frac{h}{\cos(\psi)}, \tag{3.5}$$

and

$$\chi = \tan^{-1}\left(\frac{r_c}{h}\right). \tag{3.6}$$

Hereby, the quantity $J(\psi)$ is the angular distribution of the molecular flux beyond the exit plane of the nozzle. The symbol h describes the projection of R along the nozzle axis and h_0 represents the distance from the nozzle exit to the interaction zone. The quantity $\bar{c}$ of the mean thermal velocity is given by [72]

$$\bar{c} = \sqrt{\frac{8 \cdot k_B \cdot T_{\text{temp}}}{\pi \cdot M_{\text{gas}}}}, \tag{3.7}$$

where M_{gas} is the molecular mass of the target gas.

Finally, the number density of target gas in the interaction zone ρ_t can be obtain in following form

$$\rho_t = N_{\text{int}}/V_{\text{int}}, \tag{3.8}$$

where V_{int} is the volume of the interaction zone given by

$$V_{\text{int}} = \pi \cdot {r_c}^2 \cdot h_c. \tag{3.9}$$

3.4.3 Condition of single collision

The number density of target vapor was adjusted by means of the backing pressure. This backing pressure was chosen such that it was sufficiently high to record the data at a high rate, however, at the same time low enough to fulfill the single collision condition. The latter is an important restriction,

which ensures that the possibility of one projectile passing through gas target and undergoing more than one collisions is negligibly small. An approximate expression to be fulfilled for the requirement for single collision condition is given as [73] :

$$\rho_t \cdot \sigma \cdot L_{\text{int}} \ll 1, \tag{3.10}$$

where L_{int} is the beam length in the target gas, i.e. the length of the interaction zone and ρ_t is the number density of the target gas. The quantity σ is total interaction cross sections. In many cases, σ primarily describes a single process that is dominant [73].

Using the mean free path λ_t for the interaction of a projectile with the gas jet in the interaction zone, which yields the inverse of the product of ρ_t and σ, the approximation 3.10 can be written as:

$$\lambda_t \gg L_{\text{int}}. \tag{3.11}$$

A typical range of total interaction cross section is on the order of $10^{-16}\,\text{cm}^2$ to $10^{-15}\,\text{cm}^2$. Taking the THF sample as an example, the total scattering cross section of THF by electron impact at its maximum around 100 eV amounted to $29.13 \times 10^{-16}\,\text{cm}^2$ according to the work of Baek et al. [53]. The number density ρ_t of THF vapor in the interaction zone at a backing pressure of 1 mbar was derived to be $1.3 \times 10^{14}\,\text{cm}^{-3}$ using the equation 3.8. This is certainly an upper limit given the questionable assumption of a cylindrical expansion of the gas. Then the mean free path length becomes $\lambda_t = 26\,\text{mm}$, which is 26 times larger than the interaction zone length $L_{\text{int}} = 1\,\text{mm}$, so that the experiments were performed in single collision regime.

3.5 Electron spectrometer — detection of the secondary electrons

Figure 3.11 shows an exterior view of the interaction chamber surrounded with three pairs of Helmholtz coils. Inside this chamber, an AR 65 electron spectrometer manufactured by Omicron GmbH was used to detect the secondary electrons produced in the collision between the primary beam and the gas jet. A detailed description of the spectrometer is given in this section.

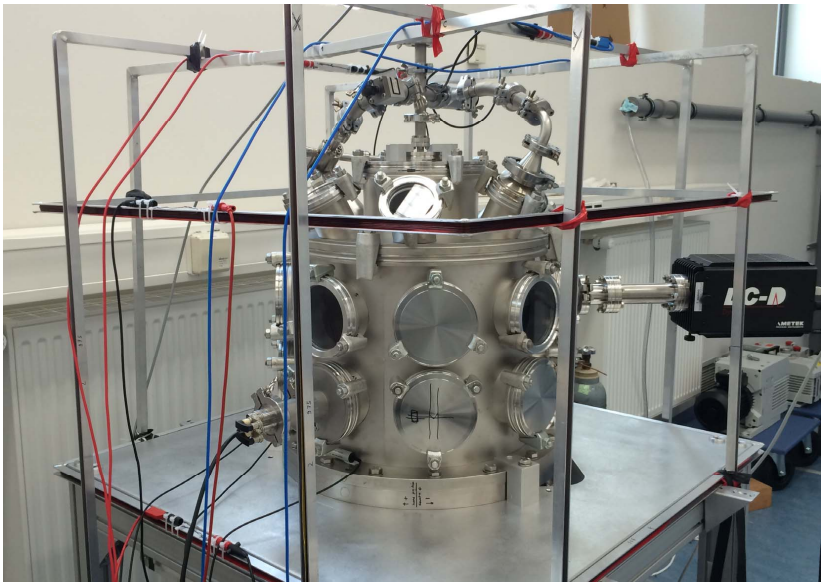

Figure 3.11 Photograph of the interaction chamber.

3.5.1 Compensation of the external magnetic field

The motion of secondary electrons, especially at low kinetic energies, is strongly influenced by the magnetic fields, including the homogeneous earth's magnetic field and the magnetic fields due to residual magnetization of components of the setup. Assuming that the magnetic field inside the analyzer is homogeneous, the secondary electrons move on a circular path and experience the central force as a combination of the electric field between the analyzer hemispheres and the Lorentz force generated by the magnetic field. For 10 eV electrons traveling through the magnetic fields of 10 µT, 30 µT and 50 µT, the maximal expected uncertainties, compared to the case without magnetic field, were found to be 6%, 22% and 36% respectively, which were estimated on the basis of the cross sections of PY by electron-impact with an incident energy of 100 eV [54].

Three orthogonal pairs of square-shaped Helmholtz coils were used to compensate the external magnetic fields. Comparing to circular Helmholtz coils, several advantages of square Helmholtz coils are given in [74], e.g. ease

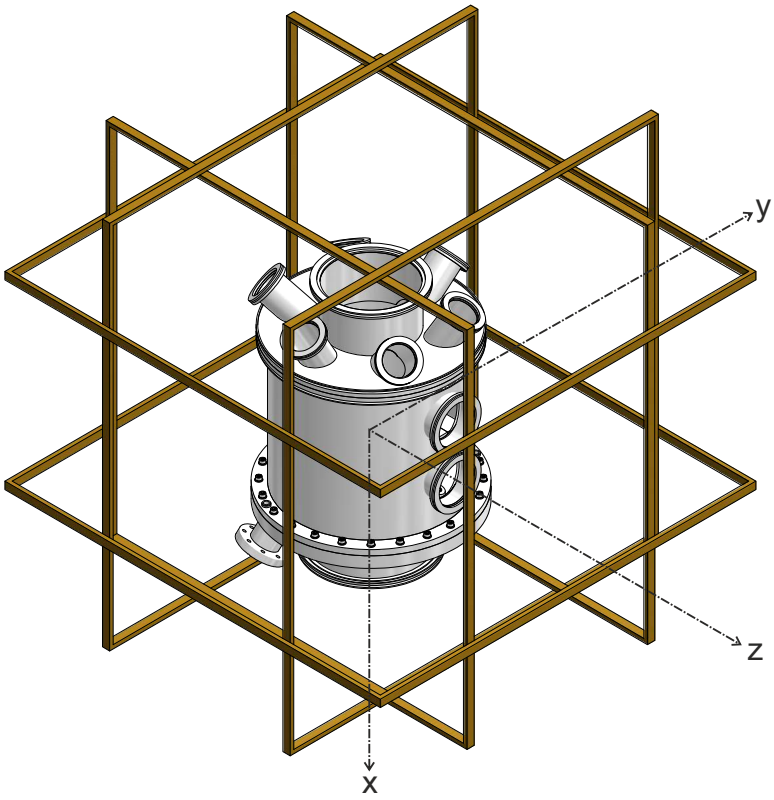

Figure 3.12 Sketch of the square-shaped Helmholtz coils system surrounding the scattering chamber.

of construction of the coils, and, relatively simple field computations. As illustrated in figure 3.12, these three pairs of coils were set up symmetrically around the scattering chamber with the axis coinciding with the primary beam direction (Z-axis), with the effusive gas jet direction (X-axis) and with the direction (Y-axis) perpendicular to beam and gas jet.

The calculation of the magnetic field produced by this system of square Helmholtz coils was carried out by a MATLAB program. In this calculation the field generated by each coil was considered separately. Taking the vertical

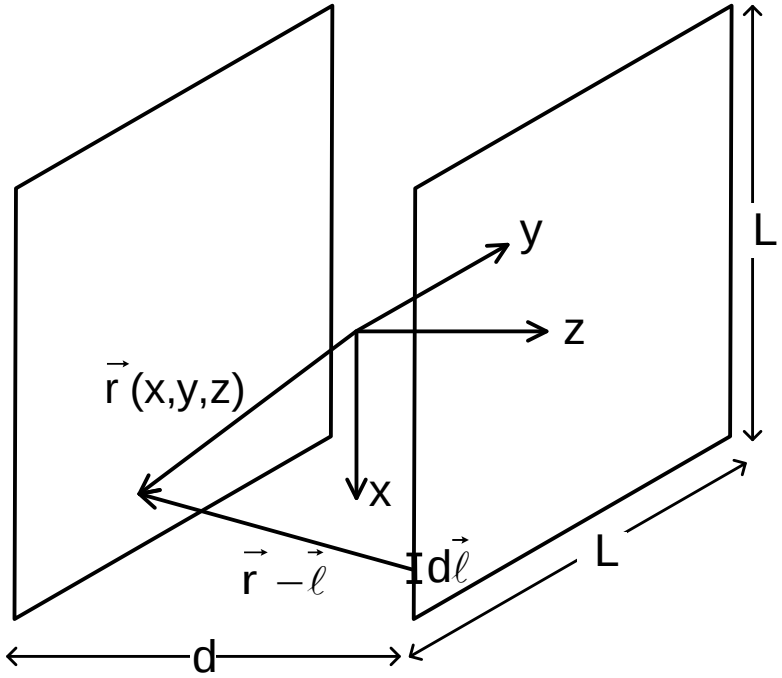

Figure 3.13 Illustration of the contribution of a line element $\mathrm{d}\vec{\ell}$ at one of four segments of the square-shaped Helmholtz coils to the magnetic field at point $\vec{r}$ according to equation 3.12.

coil located at positive Z-axis as an example, as shown in figure 3.13, the contribution to the field $\mathrm{d}\vec{B}$ at point (x, y, z) due to a current element $\mathrm{d}\vec{\ell}$ at one of the four line segments can be derived from the Biot-Savart law:

$$\mathrm{d}\vec{B} = \frac{\mu_0 N I}{4\pi} \frac{\mathrm{d}\vec{\ell} \times \left(\vec{r} - \vec{\ell}\right)}{\left|\vec{r} - \vec{\ell}\right|^3}, \tag{3.12}$$

where μ_0 is the magnetic constant, N is the number of turns on the coil and I is the current through the wire. The vector $(\vec{r} - \vec{\ell})$ represents the displacement vector from the current element $\vec{\ell} = (x_\ell, y_\ell, z_\ell)$ to the point $\vec{r} = (x, y, z)$ where the magnetic field is being calculated.

In this manner the orthogonal component B_z of the magnetic field in the primary beam direction is given by:

$$B_z = \frac{\mu_0 NI}{4\pi} \int_{-\frac{L}{2}}^{\frac{L}{2}} \left\{ \begin{aligned} &\frac{\left(y+\frac{L}{2}\right) \mathrm{d}x_\ell}{\left[\left(z-\frac{d}{2}\right)^2 + (x-x_\ell)^2 + \left(y+\frac{L}{2}\right)^2\right]^{\frac{3}{2}}} \\ &+ \frac{\left(\frac{L}{2}-y\right) \mathrm{d}x_\ell}{\left[\left(z-\frac{d}{2}\right)^2 + (x-x_\ell)^2 + \left(y-\frac{L}{2}\right)^2\right]^{\frac{3}{2}}} \\ &+ \frac{\left(x+\frac{L}{2}\right) \mathrm{d}y_\ell}{\left[\left(z-\frac{d}{2}\right)^2 + \left(x+\frac{L}{2}\right)^2 + (y-y_\ell)^2\right]^{\frac{3}{2}}} \\ &+ \frac{\left(\frac{L}{2}-x\right) \mathrm{d}y_\ell}{\left[\left(z-\frac{d}{2}\right)^2 + \left(x-\frac{L}{2}\right)^2 + (y-y_\ell)^2\right]^{\frac{3}{2}}} \end{aligned} \right\}, \tag{3.13}$$

the component B_x in the molecular gas jet direction yields:

$$B_x = \frac{\mu_0 NI}{4\pi} \int_{-\frac{L}{2}}^{\frac{L}{2}} \left\{ \begin{aligned} &\frac{\left(z-\frac{d}{2}\right) \mathrm{d}y_\ell}{\left[\left(z-\frac{d}{2}\right)^2 + \left(x-\frac{L}{2}\right)^2 + (y-y_\ell)^2\right]^{\frac{3}{2}}} \\ &+ \frac{\left(\frac{d}{2}-z\right) \mathrm{d}y_\ell}{\left[\left(z-\frac{d}{2}\right)^2 + \left(x+\frac{L}{2}\right)^2 + (y-y_\ell)^2\right]^{\frac{3}{2}}} \end{aligned} \right\}, \tag{3.14}$$

and the component B_y in the direction perpendicular to primary beam and gas jet is obtained by:

$$B_y = \frac{\mu_0 NI}{4\pi} \int_{-\frac{L}{2}}^{\frac{L}{2}} \left\{ \begin{aligned} &\frac{\left(z-\frac{d}{2}\right) \mathrm{d}x_\ell}{\left[\left(z-\frac{d}{2}\right)^2 + (x-x_\ell)^2 + \left(y-\frac{L}{2}\right)^2\right]^{\frac{3}{2}}} \\ &+ \frac{\left(\frac{d}{2}-z\right) \mathrm{d}x_\ell}{\left[\left(z-\frac{d}{2}\right)^2 + (x-x_\ell)^2 + \left(y+\frac{L}{2}\right)^2\right]^{\frac{3}{2}}} \end{aligned} \right\}, \tag{3.15}$$

where L is the length of the coil and d is the separation of the coils pair. The quantity N is the number of windings at the coil and I is the current flowing through the coil. These integrations over the four line segments were numerically evaluated by means of the rectangle rule. Then the total fields were obtained by superposition of all the contributions of six coils.

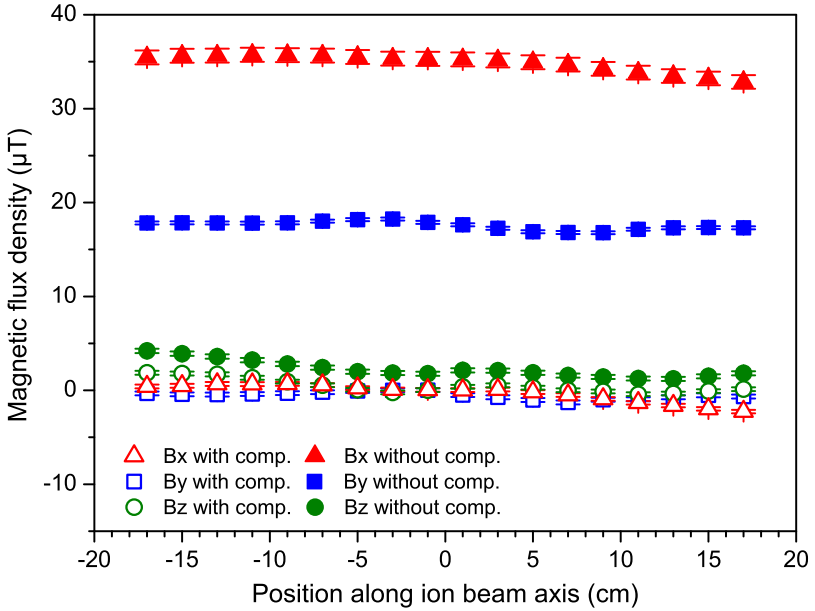

Figure 3.14 Variation of the magnetic field along the beam axis with (open symbols) and without (solid symbols) compensation of the external magnetic field. B_x (red triangles), B_z (green dots), and B_y (blue squares), represent the orthogonal components of the magnetic field in the effusive gas jet direction, in the ion beam direction and in the direction perpendicular to beam and gas jet, respectively.

To minimize the non-uniformity of produced field, the coil pairs were separated at a certain distance d such that the second derivative of the field vanished. This distance d is defined as the Helmholtz spacing and given in [74]:

$$d_i = 0.5445 \cdot L_i. \tag{3.16}$$

where the coil pairs are indicated by their central axis in the direction of $i = x, y, z$. The dimensions of the three pairs were $L_x = 90.5\,\text{cm}$, $L_z = 94.0\,\text{cm}$ and $L_y = 97.5\,\text{cm}$. Each coil consisted of 50 turns of copper wire with a diameter of 0.8 mm. The currents flowing through each coil pair were generated by the power source HAMEG HMP-4040 and set to about

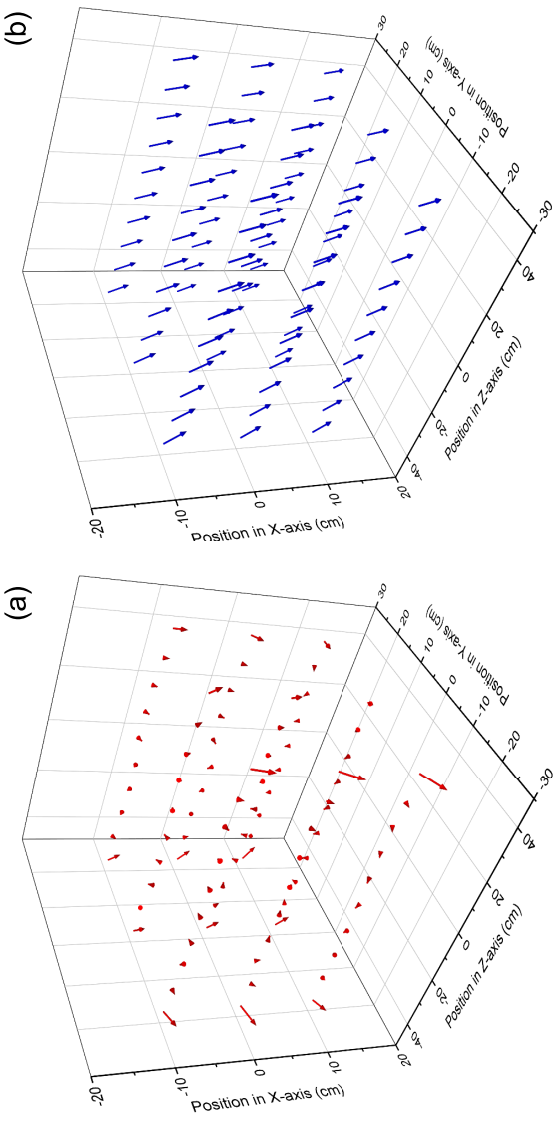

Figure 3.15 Variation of the magnetic field inside the chamber (**a**) with and (**b**) without compensation of the external magnetic field. X-, Z- and Y-axis are the effusive gas jet direction, the ion beam direction and the direction perpendicular to beam and gas jet, respectively. Vectors with arrows represent the magnitude and the direction of local magnetic field at each position.

$I_x = 450\,\text{mA}$, $I_z = 200\,\text{mA}$ and $I_y = 30\,\text{mA}$, respectively. In this case, the magnetic field intensity in the interaction zone, i.e. in the vicinity of the origin of the coordinate, could be reduced to almost zero.

The quantitative measurements of magnetic field inside the scattering chamber were carried out by three flux gate magnetometers GEO-X produced by Projekt Elektronik GmbH. These three probes were operated simultaneously with the interface IAS-4 such that the measurements could be performed in three dimensions. The analog output signals of all connected probes were available at the same time and fed into data acquisition device USB-6009 manufactured by National Instruments, which prepared the digital signals for the further processing on the computer.

Figures 3.14 and 3.15 show the variation of the magnetic field along the beam axis and inside the scattering chamber, respectively, both with and without compensation of the external magnetic field. As a result, the residual magnetic field was below $2.0\,\mu\text{T}$ over a spherical region of $0.3\,\text{m}$ in diameter. The uncertainty of the measurements was dominated by the linearity error of the probe (about $\pm 0.2\,\mu\text{T}$ when $\leq 2\,\mu\text{T}$ and 1.5% otherwise).

3.5.2 Electron spectrometer system

The AR 65 electron spectrometer was mounted on a turntable such that it could be positioned at any angle around the symmetry axis of the experimental chamber i.e. the axis of the gas jet. A mu-metal foil sheet was placed between the top of the turntable and the electron spectrometer to shield against the local magnetic field arising due to the iron-containing bearing of the rotation stage.

Figure 3.16 shows a schematic of the complete electron spectrometer system. The spectrometer comprises three main components: an electrostatic input lens system, a hemispherical energy analyzer and three channel electron multipliers. The input lens system is composed of four element electrostatic lens. It is placed at a working distance of 29 mm from the rotation axis. Its entrance aperture with a diameter of 1 mm accepts secondary electrons within a field of view of $\pm 1°$. The electrons are focused by the lens system into the hemispherical energy analyzer. The circular entrance aperture of the analyzer is 1 mm in diameter. The mean radius R_0 of the analyzer is 65 mm and the gap between two hemispheres is 28 mm.

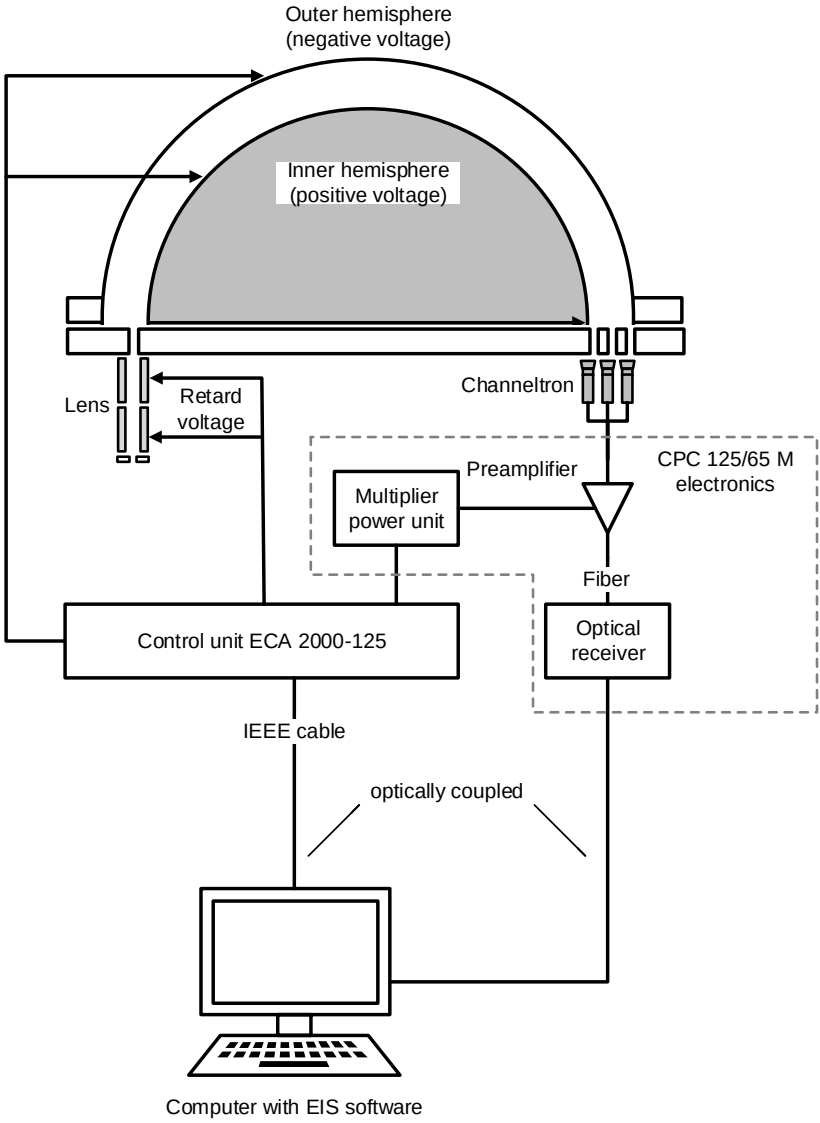

Figure 3.16 Schematic of the AR 65 electron spectrometer system.

The paths of electrons passing through a portion of an ideal spherical condenser were worked out by Purcell [75]. For an electron traveling in an orbit of the mean radius $R_0 = (R_1 + R_2)/2$, the focusing potential V_0 is obtained by:

$$eV_0 = W_p \left(\frac{R_2}{R_1} - \frac{R_1}{R_2} \right), \tag{3.17}$$

where e is the elementary charge and W_p is the kinetic energy of the passing electron, namely, the pass energy in terms of eV. The quantities R_1 and R_2 are the radius for the inner and outer hemispheres, respectively.

With respect to the pass energy W_p of the analyzer the inner and outer hemispheres were biased with voltages of positive V_1 and negative V_2, which are given by

$$eV_1 = W_p \left(2\frac{R_0}{R_1} - 1 \right) \quad \text{and} \quad eV_2 = W_p \left(2\frac{R_0}{R_2} - 1 \right). \tag{3.18}$$

The analyzer can be operated either in constant analyzer energy (CAE) mode or constant retard ratio (CRR) mode. In CAE mode, the pass energy is kept constant during a spectrum. In this case, the incoming electrons are retarded or accelerated by the lens voltages such that their kinetic energy matches the desired pass energy of the analyzer. On the other side, when the analyzer is operated in CRR mode, the ratio of kinetic energy W of the electrons relative to the pass energy W_p of the analyzer is kept constant throughout the scan range. This retard ratio known as the CRR value K_{CRR} is given as:

$$K_{\mathrm{CRR}} = \frac{W}{W_p} \tag{3.19}$$

After leaving the analyzer, electrons are detected by three channel electron multipliers (channeltrons) which amplified the charge by a factor of about 10^8. The channeltrons are placed across the exit plane of the analyzer. The size of the exit slits is $1\,\mathrm{mm} \times 5\,\mathrm{mm}$. The energy offset for each channel electron multiplier due to their different positions are corrected individually by configuration of the data acquisition software with the calibration values ($(1-0.0522) \times W_p$, $1 \times W_p$, $(1+0.0524) \times W_p$ for the respective channeltron) given by the manufacturer.

The CPC 125/65M electronics by Omicron GmbH is used for operating the channeltrons in pulse counting mode. It consists of three discrete units: a power supply for biasing the channeltrons, a pulse preamplifier and an optical

receiver. The power supply unit is used to provide an operating voltage for 0–3.5 kV for the channeltrons. The preamplifier receives the output pulses of the channeltrons and additionally filters the noise. The electrical signals are converted to optical signals within the preamplifier unit and afterwards transmits to the receiver via an optical fiber. The receiver converts the optical signal to digital output pulses which are passed on to pulse-counter board installed in the computer. The optical link isolates the computer from the spectrometer and maintains the signal on a low noise level. The cables are shield with aluminum foil to decouple the signals from high frequency noise.

The voltages for the two lenses, the analyzer hemispheres and the multiplier power unit are supplied by an ECA 2000-125 spectrometer control unit which can be configured via an IEEE-488 interface from the computer. Finally, the EIS software suit (Omicron GmbH) running on the computer is used for pulse processing and recording of an electron spectrum.

3.5.3 Characterization of the electron spectrometer

The characterization of the spectrometer was done by means of measurements using argon as the target gas, since the reference data of argon have been available in literature for both electrons and protons as primary particles. A pressurized cylinder filled with argon of high purity ($\geq 99.999\%$) was used as the gas source. When the gas jet was operated with argon, the pressure inside the scattering chamber was kept in the same range (10^{-5} mbar) as in the case of the gas jet operated with biologically relevant molecules.

3.5.3.1 Energy resolution

The energy resolution of the spectrometer was checked by measuring the argon Auger spectrum (see section 2.2.2.5, page 19) by 1550 keV protons. The electrons emitted at 90° were recorded in the energy range between 200 eV and 210 eV in steps of 0.1 eV. These measurements were made with a CRR value of 2, resulting in a pass energy of the argon Auger electrons of about 100 eV.

The measured $L_{2,3}M_{2,3}M_{2,3}$ Auger spectrum of argon is shown in figure 3.17. The measured peak No. 1 was chosen to determine the energy resolution of the spectrometer since this peak was known as singlet without

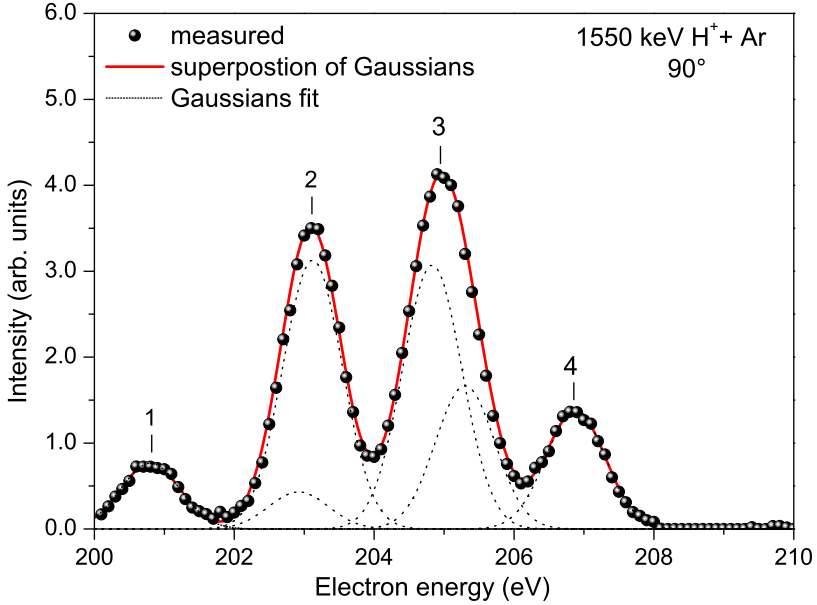

Figure 3.17 Measured $L_{2,3}M_{2,3}M_{2,3}$ Auger spectrum (dots) of argon produced at 90° by 1550 keV protons. The peaks are numbered arbitrarily for identification. The measured spectrum is fitted by the superposition (solid line) of Gaussians (dashed lines) with a FWHM of an estimated energy resolution of 1 eV.

interfering satellite transitions. A value of 1 eV for the full width at half maximum (FWHM) was obtained. According to Dahl et al. [76], this observed peak width may result from several contributions, i.e. the natural line width, the instrumental resolution and the width due to thermal Doppler broadening. The natural widths of argon $L_{2,3}M_{2,3}M_{2,3}$ Auger lines reported by Krause and Oliver [77] were found to be about 0.1 eV. The width due to the thermal Doppler broadening ΔE_T could be estimated using the equation given by Dahl et al. [76]:

$$\Delta E_T = 4\sqrt{W_0 \frac{m_e}{M_{Ar}} k_B T_{\text{temp}} \ln 2}, \tag{3.20}$$

where k_B is the Boltzmann's constant and T_{temp} is the temperature. The quantities m_e and M_{Ar} are the mass of electron and argon atom, respectively. For electrons of $W_0 = 200\,\text{eV}$ at room temperature $T_{\text{temp}} = 298\,\text{K}$, a value of $\Delta E_T = 0.028\,\text{eV}$ was obtained.

In a rough approximation, this measured 1 eV FWHM may be considered as a quadratic combination of the contributing line widths mentioned above. In this case the contribution from the natural width (about 0.1 eV) of the argon $L_{2,3}M_{2,3}M_{2,3}$ Auger lines and the estimated width of thermal Doppler broadening (<0.1 eV) were small compared with the observed 1 eV FWHM and were therefore negligible. Hence, the instrumental energy resolution of the spectrometer was estimated to be 1 eV at a pass energy about of 100 eV. Due to this limited energy resolution, the measured peaks Nos. 2 and 3 were each composed by two overlapping Auger lines, which were resolved separately in the measurements reported by Mehlhorn and Stalherm [78]. In order to represent individual Auger lines, the measured spectrum was fitted by a superposition of six Gaussians with FWHM of 1 eV.

Initial state	Final state	Involved peak	Gaussian fit (eV)	Mehlhorn [78] (eV ± 0.25 eV)
$L_2(^2P_{1/2})$	$M^2_{2,3}(^1S)$	No.2	202.92	203.01
	$M^2_{2,3}(^1D)$	No.3	205.30	205.40
	$M^2_{2,3}(^3P)$	No.3	206.88	207.03
$L_3(^2P_{3/2})$	$M^2_{2,3}(^1S)$	No.1	200.80	200.87
	$M^2_{2,3}(^1D)$	No.2	203.12	203.26
	$M^2_{2,3}(^3P)$	No.4	204.83	204.96

Table 3.2 Energy positions of argon $L_{2,3}M_{2,3}M_{2,3}$ Auger transitions.

The energy positions of those Gaussians are listed in table 3.2 and compared to the literature data reported by Mehlhorn and Stalherm [78]. This also means that the energy calibration of the electron spectrometer was accurate within the uncertainty of 1 eV. The maximal difference was found at the $L_2M^2_{2,3}(^3P)$ transition and amounted to 0.15 eV, which was within

the uncertainty of ±0.25 eV in Mehlhorn and Stalherm's measurements. To check the accuracy of the energy scale, our average value of L_2–L_3 spacing was determined as 2.12 ± 0.05 eV, which also compared fairly with the value 2.15 ± 0.01 eV of Mehlhorn and Stalherm [78]. In summary, an energy resolution of 1 eV FWHM was estimated, which is sufficient for the present measurements of DDCS.

3.5.3.2 Angular resolution

The accuracy of the angular positioning of the spectrometer was determined by measuring the elastic scattering of electrons on an argon gas jet. Based on the research of Jablonski et al. [79], the differential elastic scattering cross sections (DelCS) of argon have been parametrized in the NIST database for a wide range of primary electron energies. Here, the theoretical DelCS of argon for 100 eV electrons were considered as reference data.

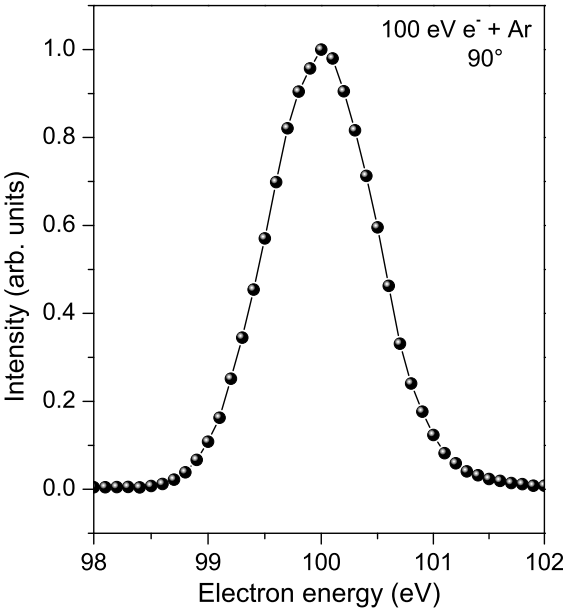

Figure 3.18 Experimental count rate of 100 eV electrons scattered elastically by argon at the scattering angle of 90° as a function of the kinetic energy.

In order to deliver the 100 eV electron beam, an electron gun EQ 22/35 (SPECS GmbH) with an energy width of ∼0.6 eV was mounted at the entrance of the spectrometer chamber. The electron beam was aligned by maximizing the current on the Faraday cup located at the opposite side of the spectrometer chamber. The measurements of the primary electron beam were carried out by an electrometer Keithley 617.

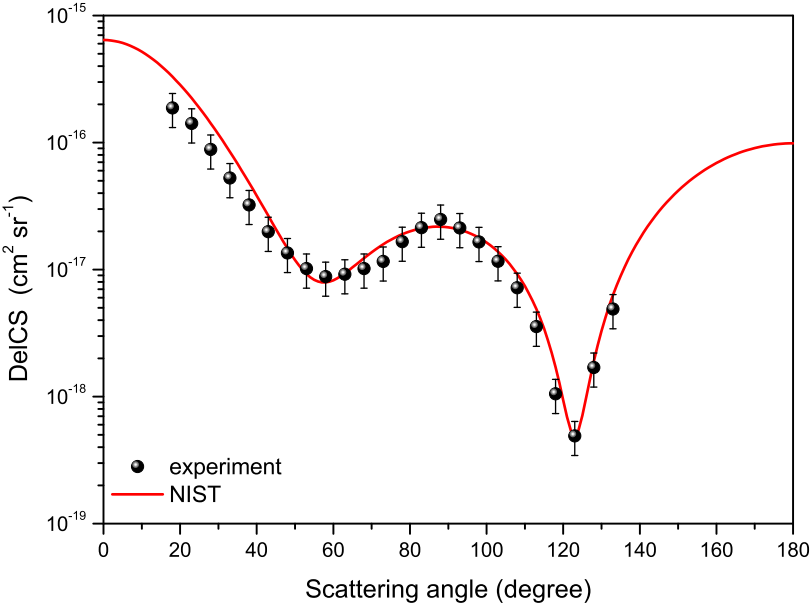

Figure 3.19 Experimental (dots) and theoretical (solid line) differential elastic scattering cross sections (DelCS) of argon by 100 eV electrons. The theoretical values are obtained from the NIST data [79] convolved with a Gaussian of a width equal to the acceptance angle of 2°.

For each scattering angle, the count rate of the secondary electrons in the elastic peak was recorded as a function of the kinetic energy. Figure 3.18 shows a measured spectrum of 100 eV electrons scattered elastically by argon at the scattering angle of 90° in the case of CRR model with a value of 1, i.e. no retardation. The elastic peak was dominated by the secondary electrons with energies around 100 eV. These measured spectra were converted into

absolute cross sections by applying a correction factor for the relative energy dependence of the detection efficiency (see equation 4.12, page 67). A further explanation of the data analysis procedure is given in section 4.2, page 64.

Our experimental DelCS of argon for 100 eV electrons are illustrated in Figure 3.19 as a function of scattering angle from 18° to 138° in steps of 5°. The angle of acceptance amounted to 2°, as the energy analyzer was equipped with an entrance aperture of 1 mm in diameter at a working distance of 29 mm. The theoretical values were obtained from the NIST data [79] convolved with a Gaussian of a width equal to the acceptance angle of 2°. As Figure 3.19 shows, a sharp minimum was predicted at the scattering angle around 123° in the theoretical calculations [79] from NIST and the position of the minimum exhibited in our measurements agrees with that of literature data [79] within the angular resolution mentioned above.

Chapter 4

Measurements principle and data analysis

4.1 Overview of the experimental data

The measurements were carried out using a crossed-beam arrangement (see section 3.1, page 23) where the primary proton beam was perpendicular to an effusive gas jet target in a high-vacuum chamber. Inside the scattering chamber an hemispherical electron analyzer was mounted on a turntable such that the spectrometer could be rotated around the axis of the gas jet.

The absolute double-differential cross sections (DDCS) for ionization were derived from the energy spectra of the secondary electrons measured as a function of their kinetic energy W at a given emission angle θ. The energy spectra were recorded by turning the electron analyzer to the desired emission angle and repeatedly scanning the electron energy and counting the electrons registered by the channeltrons. The number of registered electrons was divided by the dwell time for each electron energy to obtain the count rate. Typically, three energy scans were performed and finally the average was taken.

While the energy spectra of the secondary electrons were measured, the current in the Faraday cup and the pressure reading of the ion gauge were recorded to monitor fluctuations in the beam current and the target density. Exceptions to this procedure were measurements for emission angles below 45° at which the spectrometer housing was blocking the beam path to the Faraday cup. In this case, the beam current was obtained by the interpolation from the values measured before and after the scans at small angles.

For each emission angle, two secondary electron spectra were measured, namely with and without a gas flow. The latter measurement was done to determine the background in the electron energy spectra. The background spectra were measured without target gas and subtracted from the spectra measured with target gas. The background signal can be attributed to electrons emitted from the residual gas as well as from the metal surface and electronic noise in the detection system. However, the number density of the residual gas was four orders of magnitude lower than that of the gas jet so that the contribution from the residual gas could be neglected. For emission angles above 45° the background signal was dominated by the electronic noise. In the measurements at emission angles below 45°, the background spectra showed an increase in counts due to secondary electrons produced by protons hitting the surface of the spectrometer housing.

Sample	Proton energy	Maximum electron energies (eV) versus emission angles									
	(keV)	15°	30°	45°	60°	75°	90°	105°	120°	135°	150°
PY	75	200	200	200	200	200	200	200	200	200	n/a
	105	200	200	200	200	200	200	200	200	200	n/a
	135	200	200	200	200	200	200	200	200	200	n/a
TMP	75	200	200	200	200	200	200	200	200	200	n/a
	105	200	200	200	200	200	200	200	200	200	n/a
	135	200	200	200	200	200	200	200	200	200	n/a
THF	75	200	200	200	200	200	200	200	200	200	n/a
	105	200	200	200	200	200	200	200	200	200	n/a
	135	200	200	200	200	200	200	200	200	200	n/a
	300	200	200	200	200	200	200	200	200	200	200
	420	800	800	600	600	200	200	200	200	200	200
	840	800	800	800	800	200	200	200	200	200	200
	1200	800	800	800	800	800	800	200	200	200	200
	1550	800	800	800	800	800	600	200	200	200	200
	2000	800	800	800	800	800	600	400	400	400	400
	3000	400	400	400	800	800	400	400	400	400	400

Table 4.1 Proton energies and ranges of secondary electron emission angles and energies covered in the experiments.

Generally, the measurements were divided into two parts depending on the range of the proton energies. In the lower energy range the measurements of DDCS were accomplished at the beamline of the laboratory accelerator (see section 3.2, page 24) [80]. Primary energies of the protons were 75 keV, 105 keV and 135 keV. The spectrometer was operated in the constant retard ratio (CRR) mode, where the ratio of electron kinetic energy to analyzer pass energy is kept constant. The energy spectra were taken for electron energies from from 10 eV to 200 eV in steps of 0.5 eV with a CRR value of 1 and at emission angles 15° to 135° in 15° steps. The vapor-phase of DNA structural analogues, namely, pyrimidine (PY), tetrahydrofuran (THF) and trimethyl phosphate (TMP) were used as target samples.

For the energies between 300 keV and 3000 keV, the measurements of DDCS were carried out during several beamtimes of totally three weeks (September 15–27, 2014 and March 23–27, 2015) at the beamline of the Van de Graaff accelerator [67] located at the PTB (see section 3.3, page 34). The primary proton energies were 300 keV, 420 keV, 840 keV, 1200 keV, 1550 keV, 2000 keV and 3000 keV. The detection angles ranged from 15° to 150° in steps of 15°. The electron energy was measured from 10 eV to 200 eV in steps of 2.5 eV, from 200 eV to 400 eV in steps of 10 eV and for energies above 400 eV in steps of 20 eV. The chosen value of CRR was 1 for the electrons with energy range from 10 to 200 eV. Electrons of higher kinetic energies were analyzed with larger CRR values. The transmission of the analyzer decreases with increasing CRR value. Therefore, the count rates in the energy spectra between 200 and 400 eV (CRR 2), 400 and 600 eV (CRR 3) and 600 and 800 eV (CRR 4) were scaled up according to the CRR values used in order to compensate the decrease of the transmission.

The ranges of secondary electron emission angles and energies covered in the DDCS measurements for different target samples are listed in Table 4.1. The same evaluation procedure was applied for PY, THF and TMP and will be described in section 4.2. The information provided in this chapter has been in part published in [80] and [81].

4.2 Evaluation procedure of the experimental DDCS

Generally, the absolute value of DDCS can be determined in two ways: by directly measuring the electron detection efficiency, gas density, and other experimental parameters; and, by indirectly obtaining these parameters via normalization using other collision systems and/or impact energies where absolute cross sections are available [1]. In this work, the experimental DDCS were placed on the absolute scale using normalization procedures, which are formulated in detail within this section.

4.2.1 Derivation of the measurement equation

The number of secondary electrons $\dot{N}_s$ emitted per unit time from a length L_{int} of an ionizing particle beam trajectory into the solid angle $\Delta\Omega$ located at angle θ with respect to the beam direction in the energy range W to $W + \Delta W$, is given by [2]:

$$\dot{N}_s\left(W,\theta\right) = \dot{N}_p \rho_t L_{\text{int}} \frac{\mathrm{d}^2\sigma_{\text{ion}}}{\mathrm{d}W\mathrm{d}\Omega} \Delta W \Delta\Omega, \tag{4.1}$$

where $\dot{N}_p$ is the rate of primary particles passing a cross-sectional area of the molecular beam and ρ_t is the number of the target particles per volume (number density). The quantity $\mathrm{d}^2\sigma_{\text{ion}}/\mathrm{d}W\mathrm{d}\Omega$ is the DDCS of target molecules by the primary particles, which has dimensions of area per energy and per solid angle.

In the experiments, the number density of target molecules within the gas jet is non-uniform so that the rate of production of secondary electrons is varying over the interaction zone where the primary particle beam and the target gas jet overlap. Electrons emitted from the interaction zone, covered by the entrance aperture of the spectrometer located at angle θ with respect to the primary beam direction, are detected with a detection efficiency $\eta(W)$. The count rate of detected electrons originating from collisions of primary particles with gas jet molecules is given by:

$$\dot{N}_{\text{det},s}\left(W,\theta\right) = \dot{N}_p \dot{N}_g n_{g,p}(\theta) \eta(W) \times \frac{\mathrm{d}^2\sigma_{\text{ion}}}{\mathrm{d}W\mathrm{d}\Omega} \Delta W \Delta\Omega, \tag{4.2}$$

where $\dot{N}_g$ is the rate of gas molecules emitted from the nozzle, $n_{g,p}(\theta)$ is the effective number of target molecules per area in the projectile beam direction divided by the rate of target molecules ejected from the nozzle, and $\eta(W)$ is the detection efficiency of the spectrometer for electrons of energy W.

The rate of passing primary particles $\dot{N}_p$ can be obtained from the beam current I_{FC} measured with the Faraday cup as follows:

$$\dot{N}_p = \frac{I_{\mathrm{FC}}}{qek_I}, \tag{4.3}$$

where q and e are the charge number of the primary particles and the elementary charge, respectively. The quantity k_I is the collection efficiency of the Faraday cup.

The rate of gas molecules emitted from the nozzle can be related to the pressure p_g, measured by the ion gauge in the spectrometer vacuum chamber in the presence of the gas jet, via the ideal gas law

$$\dot{N}_g = \frac{p_g \dot{S}_{\mathrm{pump}}}{k_B T_g} k_p^{(g)} k_V^{(g)}, \tag{4.4}$$

where $\dot{S}_{\mathrm{pump}}$ is the nominal pumping speed of the turbomolecular pump for the target gas, k_B is the Boltzmann constant and T_g is the gas temperature, which is assumed to be equal to the room temperature. As both gas pressure measurement and pumping speed depend on the gas type, gas dependent correction factors $k_p^{(g)}$ and $k_V^{(g)}$ have to be applied to the ion gauge reading and the pumping speed.

Inserting equations 4.3 and 4.4 into equation 4.2 and taking into account that the spectrometer also detects a background of electrons produced from processes other than interactions between the gas jet and the primary particle beam with a current $I_p^{(g)}$, gives for the count rate $\dot{N}_{\mathrm{det}}^{(g)}(W,\theta)$ of electrons for a measurement at scattering angle θ

$$\begin{aligned}\dot{N}_{\mathrm{det}}^{(g)}(W,\theta)) = &\left(\frac{\dot{S}_{\mathrm{pump}}}{qek_I k_B} I_p^{(g)} \frac{p_g}{T_g} k_p^{(g)} k_V^{(g)} n_{g,p}(\theta)\eta(W) \times \frac{\mathrm{d}^2\sigma_{\mathrm{ion}}}{\mathrm{d}W\mathrm{d}\Omega} \Delta W \Delta\Omega\right) \\ &+ \frac{I_p^{(g)}}{qek_I}\beta(W)\eta(W),\end{aligned} \tag{4.5}$$

where $\beta(W)$ is the number of background electrons per incident primary particle that enters the spectrometer aperture within the angular range of acceptance.

When the gas jet is turned off, the corresponding measurement equation for the count rate is

$$\dot{N}_{\mathrm{det}}^{(b)}(W,\theta) = \frac{I_p^{(b)}}{qek_I}\beta(W)\eta(W), \tag{4.6}$$

where $\dot{N}_{\mathrm{det}}^{(b)}(W,\theta)$ is the background count rate and $I_p^{(b)}$ is the beam current in the background measurements.

Inserting equation 4.6, it is convenient to rewrite equation 4.5 in the following form:

$$\begin{aligned}\dot{N}_{\mathrm{det}}^{(g)}(W,\theta) = &\left(C\times I_p^{(g)}\frac{p_g}{T_g}k_p^{(g)}k_V^{(g)}n_{g,p}(\theta)\eta(W)\times\frac{\mathrm{d}^2\sigma_{\mathrm{ion}}}{\mathrm{d}W\mathrm{d}\Omega}\Delta W\Delta\Omega\right)\\ &+I_p^{(g)}\frac{\dot{N}_{\mathrm{det}}^{(b)}(W,\theta)}{I_p^{(b)}},\end{aligned} \tag{4.7}$$

where C is a constant during our measurements and is independent of the charge of the primary particle (protons or electrons) and gas types:

$$C = \frac{\dot{S}_{\mathrm{pump}}}{qek_Ik_B}. \tag{4.8}$$

Two secondary electron spectra were recorded as a function of electron energy W for each emission angle θ with and without the gas jet in operation. For the data analysis, it was assumed that the yield of background events per incident primary particle remains the same in both spectra.

According to equation 4.7, the ratio of the detected count rate with the gas jet $\dot{N}_{\mathrm{det}}^{(g)}(W,\theta)$ to the respective beam current $I_p^{(g)}$ less that of the background count rate $\dot{N}_{\mathrm{det}}^{(b)}(W,\theta)$ to $I_p^{(b)}$ is proportional to the double-differential cross section $\mathrm{d}^2\sigma_{\mathrm{ion}}^{(p)}\Big/\mathrm{d}W\mathrm{d}\Omega$ for ionization of target gas by protons:

$$\begin{aligned}\frac{\dot{N}_{\mathrm{det}}^{(g)}(W,\theta)}{I_p^{(g)}} - \frac{\dot{N}_{\mathrm{det}}^{(b)}(W,\theta)}{I_p^{(b)}} &= C\frac{p_{g,p}}{T_{g,p}}k_p^{(g)}k_V^{(g)}n_{g,p}(\theta)\eta(W)\\ &\quad\times\frac{\mathrm{d}^2\sigma_{\mathrm{ion}}^{(p)}}{\mathrm{d}W\mathrm{d}\Omega}\Delta W\Delta\Omega.\end{aligned} \tag{4.9}$$

Essentially, this equation 4.9 describes the measurements in experiments of proton collision with target gas.

4.2.2 Correction for the energy dependence of the detection efficiency

The relative energy dependence of the detection efficiency $\eta(W)$ of the spectrometer was determined by comparing secondary electron spectra measured for THF with our spectrometer to previously reported cross section data for ionization of 400 eV electrons on THF [22, 53].

These measurements were performed as an electron collision experiment on THF. The electron beam was delivered by the same electron gun used for the characterization of the electron spectrometer (see section 3.5.3.2, page 56). The target number density was chosen similar to the proton collision experiments by adjusting the gas supply for the THF gas jet such that the pressure inside the scattering chamber was kept at 10^{-5} mbar. The measurement sequence was the same as in the case of proton collision experiments (see section 4.2.1, page 64).

The relation between the DDCS for electron impact and the measured quantities is given by:

$$\begin{aligned}\frac{\dot{N}_{\mathrm{det}}^{(g,e)}(W,\theta)}{I_e^{(g)}} - \frac{\dot{N}_{\mathrm{det}}^{(b,e)}(W,\theta)}{I_e^{(b)}} &= C\frac{p_{g,e}}{T_{g,e}}k_p^{(g)}k_V^{(g)}n_{g,e}(\theta)\eta(W) \\ &\quad\times\frac{\mathrm{d}^2\sigma_{\mathrm{ion}}^{(e)}}{\mathrm{d}W\mathrm{d}\Omega}\Delta W\Delta\Omega, \end{aligned} \tag{4.10}$$

where the meaning of the symbols is analogous to those in equation 4.9. The measured energy spectra at each angle were corrected for variation of detection efficiency with electron energy and subsequently normalized to the absolute differential cross sections reported by Bug [22] at each angle. In this way, a correction factor $k_\eta(W,\theta)$ is obtained by

$$k_\eta\,(W,\theta) = \frac{p_{g,e}}{T_{g,e}}\times\frac{\mathrm{d}^2\sigma_{\mathrm{ion}}^{(e)}}{\mathrm{d}W\mathrm{d}\Omega}\times\left(\frac{\dot{N}_{\mathrm{det}}^{(g,e)}\,(W,\theta)}{I_e^{(g)}} - \frac{\dot{N}_{\mathrm{det}}^{(b,e)}\,(W,\theta)}{I_e^{(b)}}\right)^{-1}. \tag{4.11}$$

Using equation 4.10 this correction factor for the relative energy dependence of the detection efficiency $\eta(W)$ can be rewritten in

$$k_\eta(W,\theta) = \frac{1}{Ck_p^{(g)}k_V^{(g)}\Delta W\Delta\Omega n_{g,e}(\theta)\eta(W)}. \tag{4.12}$$

4.2.3 Correction for the beam profile and alignment

Solving equation 4.9 for the DDCS of the respective target gas for ionization by protons and using equation 4.12 gives:

$$\frac{\mathrm{d}^2\sigma_{\mathrm{ion}}^{(p)}}{\mathrm{d}W\mathrm{d}\Omega} = \left(\frac{\dot{N}_{\mathrm{det}}^{(g)}(W,\theta)}{I_p^{(g)}} - \frac{\dot{N}_{\mathrm{det}}^{(b)}(W,\theta)}{I_p^{(b)}} \right) \frac{T_{g,p}}{p_{g,p}} k_\eta(W,\theta) \times \frac{n_{g,e}(\theta)}{n_{g,p}(\theta)}. \quad (4.13)$$

The ratio $n_{g,e}(\theta)/n_{g,p}(\theta)$ is defined as a correction factor $k_n(\theta)$ taking into account that the beam profile and alignment in the electron measurements may be different from the case of the measurements with protons:

$$k_n(\theta) = \frac{n_{g,e}(\theta)}{n_{g,p}(\theta)}. \quad (4.14)$$

The correction factor $k_n(\theta)$ defined in equation 4.14 was derived using the measured secondary electron spectra after proton impact on argon for a subset of proton beam energies and emission angles covered in the literature data published by Rudd et al. [82]. The measurements were done in the same way as described in section 4.2.1. In these experiments of argon, the measurement equation is given by:

$$\begin{aligned} \frac{\dot{N}_{\mathrm{det},Ar}^{(g)}(W,\theta)}{I_{p,Ar}^{(g)}} - \frac{\dot{N}_{\mathrm{det},Ar}^{(b)}(W,\theta)}{I_{p,Ar}^{(b)}} &= C \frac{p_{g,Ar}}{T_{g,Ar}} k_p^{(Ar)} k_V^{(Ar)} n_{Ar,p}(\theta) \eta(W) \\ &\quad \times \frac{\mathrm{d}^2\sigma_{\mathrm{ion},Ar}^{(p)}}{\mathrm{d}W\mathrm{d}\Omega} \Delta W \Delta\Omega, \end{aligned} \quad (4.15)$$

where the meaning of the symbols is analogous to those in equation 4.9. For those emission angles, proton and secondary electron energies where literature data were available [82], a normalization factor could be defined by:

$$\begin{aligned} f_N(\theta) &= (k_\eta(W,\theta))^{-1} \frac{p_{g,Ar}}{T_{g,Ar}} \frac{\mathrm{d}^2\sigma_{\mathrm{ion},Ar}{}^{(p)}}{\mathrm{d}W\mathrm{d}\Omega} \\ &\quad \times \left(\frac{\dot{N}_{det,Ar}^{(g)}(W,\theta)}{I_{p,Ar}^{(g)}} - \frac{\dot{N}_{det,Ar}^{(b)}(W,\theta)}{I_{p,Ar}^{(b)}} \right)^{-1}. \end{aligned} \quad (4.16)$$

Using equations 4.14 and 4.15, this normalization factor is equivalent to

$$f_N(\theta) = \frac{k_p^{(g)}}{k_p^{(Ar)}} \frac{k_V^{(g)}}{k_V^{(Ar)}} \frac{n_{g,p}(\theta)}{n_{Ar,p}(\theta)} k_n(\theta). \tag{4.17}$$

Variations of the overlap integral between proton beam and gas jet as described by $n_{g,p}(\theta)$ and $n_{Ar,p}(\theta)$ are expected to be negligible in comparison of other sources of uncertainty. Therefore, the correction factor $k_n(\theta)$ defined in equation 4.14 can be obtained as:

$$k_n(\theta) = f_N(\theta) \frac{k_p^{(Ar)}}{k_p^{(g)}} \frac{k_V^{(Ar)}}{k_V^{(g)}}. \tag{4.18}$$

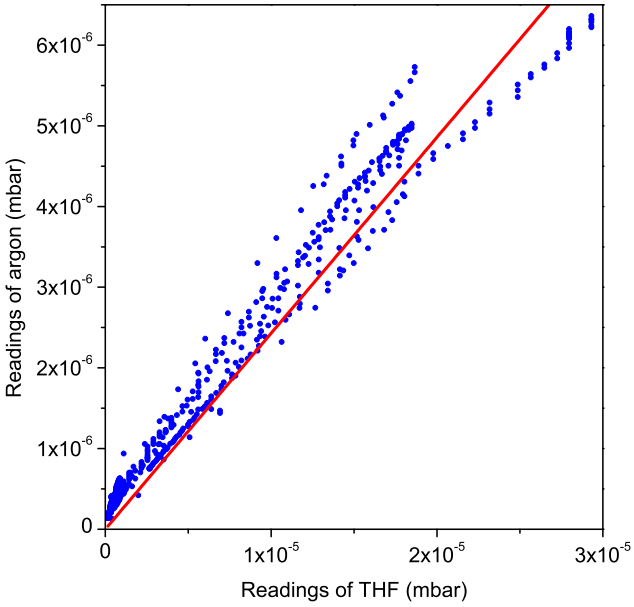

Figure 4.1 The pressure readings of the ion gauge for THF versus those for argon using the same reading of the Baratron as reference value. A linear regression (solid line) of the data was performed where the slope amounted to be 0.24 ± 0.02.

To determine the influence of the different pumping speeds, flow characteristics and ion gauge (calibrated for nitrogen) sensitivities of argon and target gas, an additional pressure measurement in the gas reservoir was performed by using a capacitance manometer (Baratron) whose reading is known to be independent of the gas type. As shown in figure 4.1, the readings of the ion gauge for THF were plotted against those for argon which corresponded to the same reading of the Baratron as obtained for THF. In this case, the ratio $k_p^{(Ar)}k_V^{(Ar)} \Big/ k_p^{(THF)}k_V^{(THF)} = 0.24 \pm 0.02$ was determined by linear regression. Then the DDCS of target gas can be calculated from equation 4.13 using the correction factors $k_\eta(W, \theta)$ for the detection efficiency as well as $k_n(\theta)$ for the different beam profile and alignment.

The same normalization procedure was used for PY and TMP. Further experimental data sets of DDCS for different targets will be detailed in chapter 6 according to the incident proton energies.

4.2.4 Correction for the low-energy secondary electron detection

For protons of energies between 300 keV and 3000 keV and secondary electron energies below 50 eV, the procedure described previously showed a contribution of electrons created by protons hitting the metal surface of the spectrometer, especially at small incident angles. Unfortunately, the contribution of such electrons was apparent only after the data analysis and the beamtime could not be repeated due to limited availability of the accelerator facility. To solve this problem, the measured DDCS for the energies below 50 eV were extrapolated from the values at higher energies by using the same relative energy dependence as for argon data from the literature [82].

Figure 4.2 shows the experimental cross sections of THF for 2000 keV protons derived from equation 4.13 as a function of the secondary electron energy for a sequence of emission angles from 15° to 135° in steps of 15°. The relative energy dependence of argon was determined by means of polynomial regression up to the fifth degree. However, it was not possible to apply this correction procedure for the data at the emission angle of 150° because the argon literature data [82] did not cover such large emission angles.

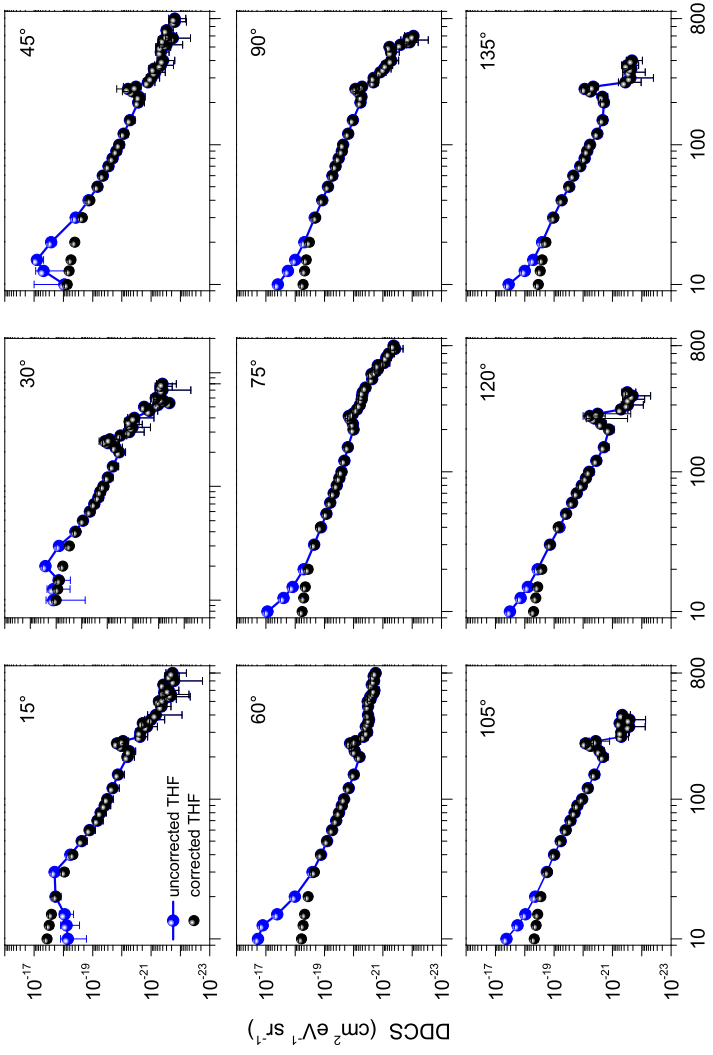

Figure 4.2 Uncorrected (blue dots) and corrected (black dots) experimental double-differential cross sections (DDCS) for ionization of THF by 2000 keV protons. The method used for the correction is explained in the text. The data are shown as a function of secondary electron energy for a sequence of emission angles from 15° to 135° in steps of 15°.

4.2.5 Parameterization of the experimental DDCS

The parameterization of the experimental DDCS is based on the previous work of Bug [22]. Since measurements at angles below 15° and above 150° are not feasible, an analytical description for the DDCS is required for an extrapolation of the experimental DDCS to 0° and 180°. This was achieved by fitting the measured data as a function of the polar emission angle θ for each secondary electron energy W. A formula for this model function was developed based on the motivation given by Rudd [83]. In his work, it was noted that the angular distribution of DDCS is usually dominated by the binary-encounter peak, which could be represented by a Lorentzian in the cosine of the angle θ. The equation of our model function is given as a superposition of three Lorentzian functions

$$\frac{\mathrm{d}^2\sigma_{\mathrm{mod}}}{\mathrm{d}W\mathrm{d}\Omega} = a_1 \left[\frac{1}{1+\left(\frac{\cos\theta+a_2}{a_3}\right)^2} + \frac{a_4}{1+b_1\left(\frac{\cos\theta+b_2}{b_3}\right)^2} + \frac{a_5}{1+\left(\frac{\cos\theta+b_5}{b_4}\right)^2} \right], \quad (4.19)$$

where the first Lorentzian term was used to reproduce the binary peak occurring at emission angles between 45° and 90°, while the second and third terms were used to fit the rise or the plateau in the cross section noted at forward and backward directions, respectively. Here, least-squares fitting was applied to retrieve the optimum parameters a_p with index p = 1–5 for the model function to the experimental data. The parameters b_q with index q = 1–5 given in table 4.2 were used to adjust the function manually. It is worth to note that the experimental data for secondary electron energies between 200 eV and 400 eV were omitted due to the Auger peaks appearing in this region.

Figure 4.3 shows the DDCS model functions of several data sets as a function of the emission angle θ. The first Lorentzian term in equation 4.19, describing the angular region of the binary-encounter peak (see section 2.2.2.2, page 17), is shown as dashed line. Generally, the region of the binary-encounter peak for emission angles θ between 45° and 90° is well reproduced by the model functions among all data sets. The increase of the experimental data at small emission angles θ of 15° and 30° are also

Proton energy (keV)	$W \leq 200\,\text{eV}$ b_1	b_2	b_3	b_4	b_5
75, 105, 135	1	-1	0.2	0.2	1.3
300	1	-0.45	0.6	0.1	1.3
420	1	-0.45	0.6	0.1	1.3
840, 1200	1	-1	0.7	0.4	1.3
1550	1	-1	0.7	0.4	1.3
2000, 3000	1	-1	0.7	0.4	1.3
Proton energy (keV)	$W > 200\,\text{eV}$ b_1	b_2	b_3	b_4	b_5
75, 105, 135	n/a	n/a	n/a	n/a	n/a
300	1	-0.45	0.6	0.1	1.3
420	1	-0.45	0.8	0.1	1.3
840, 1200	1	-1	0.3	0.1	1.3
1550	1	-1	0.1	0.1	1.3
2000, 3000	0	n/a	n/a	0.3	1.3

Table 4.2 Fitting parameters b_q used in the DDCS model function.

well described by the second Lorentzian term in equation 4.19. For large emission angles $\theta \geq 105°$, the model function provides an interpolation of the measured data, which are subject to low count rates particularly for high proton and electron energies (see figure 4.3 for $T_p = 2000\,\text{keV}, W = 400\,\text{eV}$).

4.3 Determination of the SDCS and TICS

The determination of the single-differential cross sections (SDCS) for ionization were based on experimental DDCS evaluated in section 4.2. Two different procedures were applied depending on the energy range of the secondary electrons. Due to the limited energy range of secondary electrons covered in the measurements, the experimental SDCS were obtained from 10 eV to 200 eV and from 10 eV to 400 eV for protons with energies below

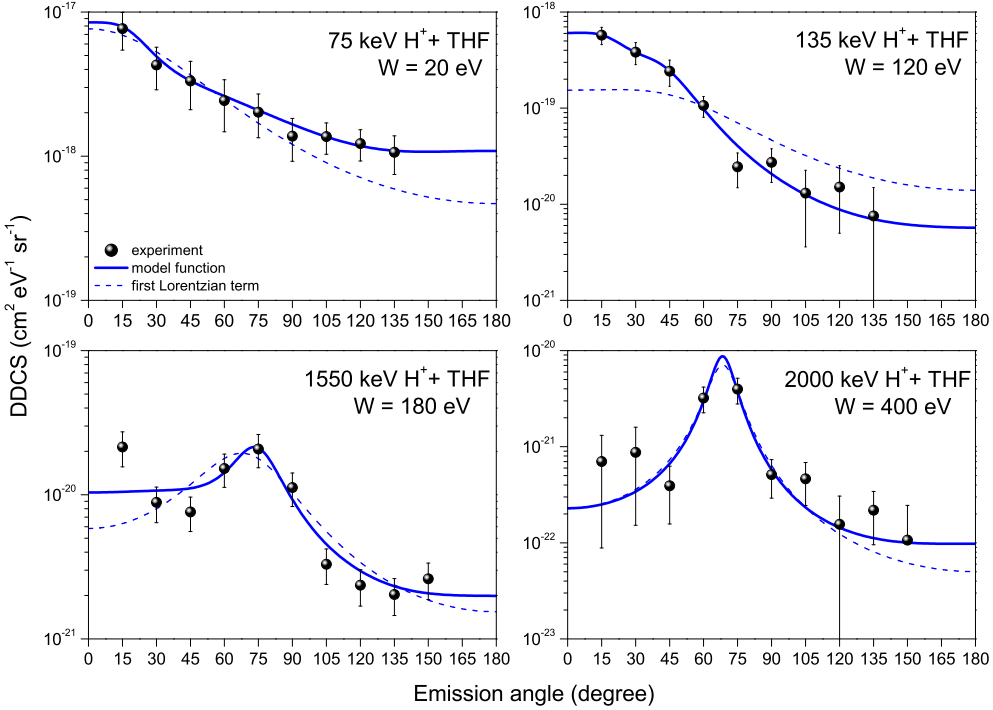

Figure 4.3 Model functions (solid line) of the double-differential cross sections (DDCS) for ionization of THF at different proton energy and secondary electron energy. Experimental data (symbols) are shown as a function of the emission angles from 15° to 135° or to 150° in steps of 15°. The dashed line corresponds to the first Lorentzian term in equation 4.19 describing the angular region of the binary-encounter peak.

1550 keV and above 2000 keV, respectively. For electron energies below 200 eV, the SDCS were obtained from the determined DDCS according to equation 4.19. The integration of DDCS model functions over the emission angles yielding the SDCS $\mathrm{d}\sigma_{\mathrm{ion}}/\mathrm{d}W$ [2]

$$\frac{\mathrm{d}\sigma_{\mathrm{ion}}}{\mathrm{d}W} = \int \frac{\mathrm{d}^2\sigma_{\mathrm{mod}}}{\mathrm{d}W\mathrm{d}\Omega}\,\mathrm{d}\Omega = 2\pi \int_0^{\pi} \frac{\mathrm{d}^2\sigma_{\mathrm{mod}}}{\mathrm{d}W\mathrm{d}\Omega}\sin\theta\,\mathrm{d}\theta. \tag{4.20}$$

However, as previously mentioned, the DDCS between 200 eV and 400 eV were omitted in the parametrization due to the contribution from Auger electrons. For the sake of the completeness of the data, the SDCS in this energy range were also determined directly from the experimental DDCS using the trapezoidal rule:

$$\frac{\mathrm{d}\sigma_{\mathrm{ion}}}{\mathrm{d}W} = 2\pi \sum_{k=1}^{12} \left[(\theta_{k+1} - \theta_k) \cdot \frac{1}{2} \left(\sin\theta_k \left.\frac{\mathrm{d}^2\sigma_{\mathrm{exp}}}{\mathrm{d}W\mathrm{d}\Omega}\right|_k + \sin\theta_{k+1} \left.\frac{\mathrm{d}^2\sigma_{\mathrm{exp}}}{\mathrm{d}W\mathrm{d}\Omega}\right|_{k+1} \right) \right], \tag{4.21}$$

where θ_k with $k = 1$–12 are a sequence of emission angles θ from 0° to 165° in steps of 15°, which indicates that $\theta_{k+1} - \theta_k = 15°$. Then equation 4.21 can be rewritten as:

$$\frac{\mathrm{d}\sigma_{\mathrm{ion}}}{\mathrm{d}W} = \frac{\pi^2}{12} \sum_{k=1}^{12} \left(\sin\theta_k \left.\frac{\mathrm{d}^2\sigma_{\mathrm{exp}}}{\mathrm{d}W\mathrm{d}\Omega}\right|_k + \sin\theta_{k+1} \left.\frac{\mathrm{d}^2\sigma_{\mathrm{exp}}}{\mathrm{d}W\mathrm{d}\Omega}\right|_{k+1} \right), \tag{4.22}$$

where, as an approximation, the experimental DDCS were assumed to be flat at forward (below 15°) as well as backward directions (above 150°).

The total cross sections for ionization (TICS) were calculated by integrating the SDCS over the range of secondary electron energies using the following expression [2]:

$$\sigma_{\mathrm{ion}} = \int_0^{W_{\mathrm{max}}} \frac{\mathrm{d}\sigma_{\mathrm{ion}}}{\mathrm{d}W}\,\mathrm{d}W. \tag{4.23}$$

Particularly the energy $W_{\mathrm{max}} = 200\,\mathrm{eV}$ was used as the upper limit owing to the rapid decrease of the SDCS at higher electron energies. The SDCS at these energies give only a negligible contribution to the TICS. The integral was calculated with the trapezoidal rule in a step size of 1 eV. In this

calculation, the SDCS below 10 eV were assumed to have the same value as at 10 eV, which is justified by the expected plateau at low electron energies, that was predicted by the theory and experimentally observed for argon in this proton energy range [82]. The results of SDCS and TICS will be presented in chapter 6.

4.4 Discussion of the experimental uncertainty

The uncertainties in the measurements come from several sources. One source could be attributed to the residual magnetic field inside the chamber, which may affect the path of secondary electrons with very low kinetic energies. Assuming a homogeneous magnetic field of 10 µT inside the analyzer, an uncertainty of 6% was found for electrons with a kinetic energy of 10 eV [54]. However, for localized inhomogeneous fields such as those observed around the rotation stage, it is difficult to estimate their effect. Therefore, the measured data below 10 eV were excluded.

An additional source could arise from the inaccuracy of charge collection of the Faraday cup. This inaccuracy arose due to escaping electrons and was estimated using the measurement results reported by Grusell et al. [84] and it amounts to about 4%. The standard deviations for current and pressure fluctuations were mostly below 1%. Uncertainties arising from reading inaccuracies of the electrometer and pressure sensor, and from the uncertainty in the detector efficiency and transmission are included in the uncertainty of the angle and energy dependent normalization factor, that amounts to about 25% [53]. Similarly, the dominant contribution to the uncertainty of the gas-dependent sensitivity factor for the ion gauges is given by the uncertainty of the absolute elastic cross sections, which is 13% [53]. Another source is due to the statistical uncertainty in count rate measurements. For protons of energies between 75 keV and 135 keV the statistical uncertainty ranges from 0.9% to 17.7% depending on the electron energy and emission angle. For protons of energies between 300 keV and 3000 keV, it amounts to be <10% and 10%–50% for electron energies below and above 600 eV, respectively. The larger uncertainties at higher electron energies are due to the poor statistics stemming from a lower ionization cross section and smaller spectrometer transmissions caused by the use of higher CRR values of up to 4.

Uncertainties may also arise from the non-uniformity of the ionizing particle beam in the interaction zone. A variation of the beam profile might affect the count numbers of electrons. At the beamline of the laboratory accelerator (see section 3.2, page 24), the proton beam was optimized on maximum current and centered by apertures that were optically aligned to the beamline axis. The proton beam size was also monitored by phosphor screen. The diameter was about 1.5 mm at reduced beam current as required to produce a structured profile on the screens. At full current, however, the proton beam spot appeared up to three times larger. Electron spectra were taken with the proton beam deflected to several positions to estimate the sensitivity of the count rate to the beam position. Indeed, the count rate dropped at small deflections already and vanished when the beam was more than 1 mm down or off the spectrometer compared to its optimal position. Thus, the sub-millimeter shift of the 105 keV compared to the 75 keV beam position may have led to a 50% lower count rate; this uncertainty is not included in above uncertainties, because the available equipment did not allow a proper quantification at the time of measurement. At the beamline of PIAF (see section 3.3, page 34), the Van de Graaff accelerator can provide an comparable stability of the beam profile due to its higher incident energies and a longer focusing distance.

The measurement quantities were not correlated, so that the standard uncertainty of the DDCS was determined according to the law of propagation of all contributing uncertainties. The combined relative uncertainty of the DDCS is about 30% for electron energies below 600 eV, but then increases up to 60% due to the low statistic for electron energies above 600 eV. Integration of cross sections over angle or energy involves additional uncertainties but also some averaging. It is unlikely that there is more than about 5% uncertainty introduced by the integration.

Chapter 5

Theoretical treatments

5.1 Introduction

Experimental cross section data obtained in this work are compared with several theoretical methods, which are briefly introduced in this chapter. The development of these theoretical models have been reported in detail previously [1, 18, 23–25, 27]. Part of these theoretical data for the sample targets (PY, THF and TMP) investigated in this work and published in [80] and [81] have been calculated by C. Champion and P. de Vera within the framework of *ad hoc* international cooperations. The argumentation given in the articles [1, 18, 23–25, 80, 81] are followed in this chapter. The original symbols are also mostly kept to provide a straightforward relation to the aforementioned articles.

For several decades, various theoretical methods have been developed to investigate the fundamental process of electron emission from atoms or molecules induced by charged particle impact. Generally, these methods fall into two different categories, the classical and the quantum-mechanical treatment. The first attempt to formulate the electron production generated from ion-atom collision was made by Rutherford [3] at the beginning of last century. In his fundamental work, an analytical i.e. the original Rutherford equation (see section 5.2, page 83), was given for a two-body problem under the assumption that the target electron is free and at rest. Based on this formalism, Gryziński [4, 85, 86, 87] introduced a classical theory called the binary-encounter approximation (BEA) to describe the two-body process as a binary collision where the projectile interacts with a moving electron. Later, this BEA model was extended by Abrines and Percival [5, 88] for considering more realistic three-body interactions. This treatment, known as classical trajectory Monte Carlo (CTMC) method, has included the interactions of an electron with both the projectile and target nucleus.

On the other side, quantum mechanics has been proven as a powerful tool to investigate electron emission mechanisms from the ion-atom collision. As Rudd et al. [18] summarized in a review article, two types of the quantum mechanical treatments, depending on the intensity of the interaction between the target electron and the incoming and outgoing projectiles, are quite important for describing atomic or molecular ionization:

(i) the electron-target interaction is strong whereas the electron-projectile interaction is weak,

(ii) and both, electron-target and electron-projectile, are strong interactions.

In view of the center concept (see section 2.2.2.1, page 15) introduced by Stolterfoht et al. [1], treatments of type (i) are usually applied in the zero or single-center case where the ejected electron and the projectile differ significantly in their velocities or outgoing directions. Treatments of type (ii) is necessary for a consideration of specific two-center phenomena, such as the ECC process (see section 2.2.2.4, page 19), where the outgoing electron and projectile are leaving at similar velocities and directions after the collision.

One of the popular treatment of type (i) is called the first Born (B1) approximation (see section 5.3, page 86), which considers only a weak perturbation of the target potential by the incoming projectile. A more appropriate method of type (ii) is the continuum distorted wave (CDW) method [7, 8], which has been successful in its treatment of two-center effects. For calculation of TICS, a limitation of CDW approximation is still found in the energy range, where the incident velocity of the projectile matches the classical Bohr velocity of the electron in the target orbit. To solve this problem, a modified version of CDW was proposed by Crothers and McCann [9], using an eikonal approximation to represent the initial state. This improved calculation is called continuum distorted wave-eikonal initial state (CDW-EIS) approximation.

Electron emission processes as well as total, single-differential, and double-differential ionization cross sections of diverse atomic or simple molecular targets for ion impact have been summarized in several reviews [1, 2, 18, 89]. Recently, the focus shifted to more complex, biologically relevant molecules. Since water is commonly used as a default medium to describe living tissue, several review articles of the experimental and theoretical works of ion-induced ionization have recently been given by Bernal-Rodriguez et al. [90] and Champion et al. [27] for liquid and vapor water, respectively. Several existing theoretical models have also been used to calculate ionization cross sections of complex biological molecules like DNA or RNA constituents. For example, the simple BEA model [91] yields reasonable accuracy for atoms or small molecules, but differs for large molecules. Regarding other more sophisticated models, such as the CDW-EIS or CTMC method, Champion et al. [92] have studied TICS of nucleobases and found a very good agreement

between the both models at high enough impact velocities. However, their applications to large biological molecules require complex and expensive computational efforts.

Generally, the perturbative B1 approximation is an effective quantum mechanic method for a wide range of radiological applications [27], benefiting from its simplicity and traceability. Several variants based on the B1 approximation have been successfully employed for treating ionization processes in many atomic and molecular target systems including nucleobases, which are the subject of section 5.3. For comparison, simple calculations of SDCS using the classical model, here limited to the Rutherford formula, are also included in section 5.2.

5.2 Classical treatment — the Rutherford formula

The simplest approach to determine the ionization cross section for the collision of a charged particle is provided by the Rutherford formula. Assuming that all the energy transfer is given to the kinetic energy of the ejected electron, as would be the case of a free electron initially at rest, the cross section, differential in electron energy, is given by Rutherford [18] as a simple expression:

$$\frac{\mathrm{d}\sigma_R}{\mathrm{d}W} = \frac{4\pi a_0^2 Z_p^2}{T}\left(\frac{E_R}{W}\right)^2, \tag{5.1}$$

where a_0 is the Bohr radius, Z_p is the nuclear charge of the projectile, E_R is the Rydberg energy, W is the kinetic energy of the target electron after the collision, $T = (T_p m_e)/M_p$ is the kinetic energy of an electron of mass m_e moving with the velocity same as the incident particle with kinetic energy T_p and mass M_p.

Considering the case of a bound atomic electron, which is initially not at rest, a part of the energy transfer Q is required to overcome the binding energy B and the remainder is given to the kinetic energy W of the ejected electron. Consequently, according to [18], equation 5.1 can be rewritten as:

$$\frac{\mathrm{d}\sigma_R}{\mathrm{d}W} = \frac{4\pi a_0^2 Z_p^2}{T}\left(\frac{E_R}{Q}\right)^2 = \frac{4\pi a_0^2 Z_p^2}{T}\left(\frac{E_R}{B+W}\right)^2, \tag{5.2}$$

which indicates that for $W \gg B$ the cross section approaches the result of equation 5.1 and follows approximately an W^{-2} law.

As the Rutherford formula is obtained from classical mechanics, it generally underestimates the cross section for the production of low-energy electrons from soft-collisions (see section 2.2.2.3, page 18), for which a quantum-mechanical description is essential. To achieve agreement with the Born approximation [6], Stolterfoht et al. [1] modified equation 5.2 by introducing a semi-empirical term c_S:

$$\frac{\mathrm{d}\sigma_S}{\mathrm{d}W} = \frac{4\pi a_0^2 Z_p^2}{T}\left(\frac{E_R}{c_S B + W}\right)^2, \tag{5.3}$$

with

$$c_S = \left[\ln\left(\frac{2T}{B}\right)\right]^{-\frac{1}{2}}. \tag{5.4}$$

Finally, the TICS is obtained from equation 5.3 integrated over W, as given by Stolterfoht et al. [1], yielding

$$\sigma_S = \frac{4\pi a_0^2 Z_p^2 E_R^2}{TB}\left(\ln\frac{2T}{B}\right)^{\frac{1}{2}}. \tag{5.5}$$

For a target molecule with shell structure, equations 5.2 through 5.5 have to be expanded by summing the cross sections for each target electron with binding energy B_i for i-th subshell. In this work, the binding energies for PY, THF and TMP (table 5.1) were calculated by means of the restricted Hartree-Fock (RHF) method in GAMESS [93] with the 6-311G basis set [22]. The number of molecular orbitals used in the target description were 21, 20 and 37 for PY, THF and TMP, respectively. Because orbital energies calculated by the RHF method are often higher than the ground state energies [94], the binding energies of the highest occupied molecular orbital were substituted by the experimental values of the ionization threshold determined by Kishimoto and Ohno [95], by Mayer et al. [71], by Tasaki et al. [96], for PY, THF and TMP respectively.

SDCS and TICS were calculated using Rutherford formula for the proton energy range below 300 keV (see table 5.2, page 87). For higher proton energies, the Rutherford formula is expected to fail in describing the measured data, as the energy range of secondary electrons covered in the experiment was only limited to relatively low energy transfers.

Subshell	Binding energies B_i (eV)		
i	PY	THF	TMP
1	423.44	557.94	2178.05
2	423.44	306.17	559.41
3	307.52	306.17	559.40
4	307.09	305.08	559.40
5	307.09	305.07	557.34
6	305.92	36.97	306.92
7	36.57	28.97	306.92
8	33.02	27.21	306.92
9	29.75	22.25	209.59
10	24.64	22.14	152.44
11	24.55	18.69	152.42
12	20.52	18.19	152.42
13	19.37	16.28	39.64
14	17.98	15.97	37.67
15	16.53	15.11	37.67
16	16.27	13.60	35.23
17	15.96	13.57	27.43
18	12.58	12.99	26.20
19	11.54	12.31	26.20
20	10.96	9.74	21.40
21	9.73		19.37
22			19.37
23			18.44
24			17.85
25			17.85
26			17.13
27			17.09
28			17.09
29			15.90
30			14.33
31			14.33
32			13.59
33			13.32
34			13.32
35			12.90
36			10.81
37			10.81

Table 5.1 Binding energies B_i of i-th subshell electrons in PY, THF and TMP. These data are taken from the work of Bug [22] and used for the Rutherford formula and the HKS model.

5.3 Quantum-mechanical treatment — the first Born approximation

A weak electron-projectile interaction can be treated perturbatively [18]. Based on this approach, Bethe [6] performed a pioneering work to describe the electron emission from ion-atom collisions using the first Born (B1) approximation, which is a first order perturbation theory. Within this perturbative approach, the initial and final states of the incident particle are expressed as plane waves [1], while the target electrons can be described using an appropriate wave function [2]. However, the strong interaction of the electron with the target nucleus is fully taken into account [1]. Therefore, the B1 approximation describes essentially the electron emission from the single center formed by the target nucleus and, hence, is associated with target-center case [1] (see section 2.2.2.1, page 15).

The B1 approximation is applicable for prediction of soft-collision electrons, which are mainly deflected by the target nucleus [1]. It should be noted that for bare projectiles the B1 approximation is sufficient for describing the binary-encounter process, despite the strong electron-projectile interaction in the initial state. This is due to the fact that the calculation considering the perturbation yields the same result as obtained for the two-body Coulomb problem [1]. Accordingly, the B1 approximation is excepted to yield accurate results for SDCS, which are primarily determined by the electron emission mechanism of the binary-encounter process and soft collision.

The simplest version of the B1 approximation can be obtained if a plane wave is used for describing the outgoing electron, whose interaction with the target nucleus is completely ignored in this case. It is denoted as the fully plane wave Born approximation (PWBA). Note that the PWBA, which contains neither a projectile nor a target center, is commonly referred as zero-center case [1] (see section 2.2.2.1, page 15). Due to its computationally simplicity, the PWBA is most frequently used through the literature [12, 97, 98].

The theoretical methods discussed in this section have been performed within the B1 approximation. As comparison, cross sections were calculated for the entire proton energy range by means of the well-known Hansen-

Kocbach-Stolterfoht (HKS) model [23], which is a variant of the PWBA. The calculations using the HKS model and Rutherford formula were accomplished with own developed C++ code. For proton energies above 300 keV, the ionization cross sections of THF [81] have been derived by de Vera et al. [24, 25] using a recently reported semi-empirical model, in which the target is described by the dielectric response function (DRF). However, this method (denoted hereafter by DRF) is not suited for lower proton energies. Thus, Champion et al. have applied a boundary-corrected first Born approximation (CB1) for the investigation of ionization cross sections of PY, THF and TMP by proton impact of 75 keV, 105 keV and 135 keV [80]. In table 5.2, the calculations performed by the above mentioned methods are specified according to the range of proton energies.

Data set	$T_p < 300\,\mathrm{keV}$	$T_p \geq 300\,\mathrm{keV}$
DDCS	CB1 and HKS	HKS and DRF
SDCS	CB1, HKS and Rutherford	HKS and DRF
TICS	CB1, HKS and Rutherford	CB1, HKS and DRF

Table 5.2 Theoretical methods utilized in this work for different proton energy ranges. The terms labeled in this table are given in the text.

5.3.1 Hansen-Kocbach-Stolterfoht model

The semi-empirical model reported by Stolterfoht et al. [1], Hansen and Kocbach [99] has been developed to determine ionization by non-relativistic ions. Bernal and Liendo [23] carried out consistency tests of the HKS model and recommended a DDCS formula that was determined analytically from the original expression of Hansen and Kocbach [99]:

$$\frac{\mathrm{d}^2\sigma_{\mathrm{HKS}}}{\mathrm{d}W\mathrm{d}\Omega} = \frac{16a_0^2Z_p^2}{3\pi E_R v_p^2 \alpha k_c^3}\left[\frac{1}{1+(\hat{K}_m - \hat{k}_t\cos\theta)^2}\right]^3, \tag{5.6}$$

where

$$k_c = \left(k^2 + \frac{2\alpha^2}{\ln(2v_p^2/\alpha^2)}\right)^{\frac{1}{2}}, \tag{5.7}$$

$$k_t = \left(k^2 + 0.2\alpha^2\sqrt{v_p/\alpha}\right)^{\frac{1}{2}}. \tag{5.8}$$

Here, a_0 is the Bohr radius and E_R the Rydberg energy. The quantities Z_p and $v_p = (T/E_R)^{\frac{1}{2}}$ are the charge and the velocity of the projectile, respectively, with T the kinetic energy of an electron moving with the same velocity as the projectile. The quantities $\alpha = (B/E_R)^{\frac{1}{2}}$ and $k = (W/E_R)^{\frac{1}{2}}$ represent the mean initial and final electron momenta, where B and W are the initial binding energy and final kinetic energy of emitted electron, respectively.

The function in the square brackets of equation 5.6 describes the binary-encounter interaction (see section 2.2.2.2, page 17). According to the work of Bernal and Liendo [23], the quantities $\hat{K}_m = K_m/\alpha_c$ and $\hat{k}_t = k_t/\alpha_c$ are the normalized momenta with

$$\alpha_c = \alpha \left(1 + 0.7 \frac{v_p^2}{v_p^2 + k^2} \right), \tag{5.9}$$

where $K_m = (\alpha^2 + k^2)/2v_p$ is the minimum momentum transfer. This function resembles a Lorentzian whose width is governed by α_c and involves the electron emission angle θ.

In the work of Hansen and Kocbach [99], the descriptions of the initial and final electron states are approximated by a hydrogenic and a plane wave function, respectively. Moreover, the amplitude of the outgoing wave is determined by means of the peaking approximation which neglects the initial momentum of the bound electron. This treatment causes a singularity in the low energy regime. Thus, equations 5.7 to 5.9 are employed as semi-empirical modifications [1, 2] which originated from fitting of HKS model results to those of the B1 formula published by Landau et al. [100].

Integration of equation 5.6 leads to the following SDCS formula, which was recommended by Bernal and Liendo in their work [23]:

$$\begin{aligned} \frac{\mathrm{d}\sigma_{\mathrm{HKS}}}{\mathrm{d}W} = \frac{4a_0^2 Z_p^2}{E_R v_p^2 \alpha k_c^3 \hat{k}_t} \Bigg\{ & \tan^{-1}(\hat{K}_m + \hat{k}_t) - \tan^{-1}(\hat{K}_m - \hat{k}_t) \\ & + \frac{5(\hat{K}_m + \hat{k}_t) + 3(\hat{K}_m + \hat{k}_t)^3}{3[1 + (\hat{K}_m + \hat{k}_t)^2]^2} - \frac{5(\hat{K}_m - \hat{k}_t) + 3(\hat{K}_m - \hat{k}_t)^3}{3[1 + (\hat{K}_m - \hat{k}_t)^2]^2} \Bigg\}. \end{aligned} \tag{5.10}$$

It should be noted that equations 5.6 and 5.10 are for a single target electron and must be summed over all electrons corresponding to each i-th subshell for multi-electronic targets. These binding energies B_i employed here are the same as used for the Rutherford formula.

In summary, the advantage of the HKS model is that it provides an analytical expression with empirical fitting to the B1 calculations [100] and requires only the binding energies of electrons in the respective atom or molecule. Hence, the HKS model enables a fast calculation of ionization cross sections.

5.3.2 Analytical model based on the dielectric formalism

As reported by de Vera et al. [25], a semi-empirical model using the dielectric formalism [97, 101] has been recently proposed for calculating the DDCS of condensed organic materials impacted by fast ions. The dielectric formalism is based on the PWBA and provides the differential inelastic scattering cross section by exploiting the dependence of the electronic excitation spectrum of the target on the transferred energy $\hbar\omega$ and momentum $\hbar k$ (i.e. the dielectric response function $\epsilon(\hbar k, \hbar\omega)$ of the target).

According to the work of de Vera et al. [25], the energy transfer $\hbar\omega$ in an ionizing collision can be expressed as:

$$\hbar\omega = B_i + W, \tag{5.11}$$

where B_i is the binding energy of a given electronic inner shell, or the mean binding energy of the outer shell electrons [24, 25]. In the work of de Vera et al. [25], the DDCS for ionizing an electronic shell i as a function of the secondary electron energy W and the momentum transfer to the target $\hbar k$ is written as:

$$\left.\frac{\mathrm{d}^2\sigma_{\mathrm{DRF}}}{\mathrm{d}W\,\mathrm{d}k}\right|_i = \frac{e^2}{\pi\hbar^2\mathcal{N}}\frac{M_p\left[Z_p-\rho(k)\right]^2}{T_p}\frac{1}{k}\,\mathrm{Im}\left[\frac{-1}{\epsilon(\hbar k, B_i+W)}\right]_i, \tag{5.12}$$

where T_p, M_p, and Z_p are, respectively, the kinetic energy, mass, and atomic number of the projectile, and $\rho(k)$ is the Fourier transform of its electronic density. The target is characterized by its number density $\mathcal{N}$ and the energy loss function (ELF) $\mathrm{Im}\left[-1/\epsilon(\hbar k, B_i+W)\right]_i$, which represents its electronic excitation spectrum.

The momentum transfer $\hbar k$ is related to the scattering angle ϑ of the projectile and is given by de Vera et al. [25]:

$$\hbar k = \sqrt{2M_p \left[2T_p - (B_i + W) - 2\sqrt{T_p \left(T_p - (B_i + W)\right)} \cos(\vartheta)\right]}. \quad (5.13)$$

In order to obtain the DDCS as a function of the ejected angle θ of the secondary electron, it is assumed that θ is related to ϑ via $\theta = \vartheta/\gamma$ [25]. The proportionality constant γ is derived from the binary-encounter approximation, $\gamma = \vartheta_{\max}/\theta_{\mathrm{BE}}$, where θ_{BE} is the ejection angle of the binary-encounter peak (see equation equation 2.5, page 17) and $\vartheta_{\max}$ is the scattering angle of the projectile at which the ionization cross section is maximum [25].

Using the definition of the solid angle, $\mathrm{d}\Omega = 2\pi \sin(\theta)\mathrm{d}\theta$, and equation 5.13, the DDCS from equation 5.12 can be rewritten to following expression, as given by de Vera et al. [25]:

$$\begin{aligned} \left.\frac{\mathrm{d}^2\sigma_{\mathrm{DRF}}}{\mathrm{d}W\mathrm{d}\Omega}\right|_i = {} & \frac{\gamma e^2}{2\pi^2\hbar^2\mathcal{N}\sin\theta} \frac{M_p \left[Z_p - \rho(k)\right]^2}{T_p} \mathrm{Im}\left[\frac{-1}{\epsilon(\hbar k, B_i + W)}\right]_i \\ & \times \frac{\sqrt{T_p \left[T_p - (B_i + W)\right]} \sin(\gamma\theta)}{2T_p - (B_i + W) - 2\sqrt{T_p \left[T_p - (B_i + W)\right]} \cos(\gamma\theta)} \\ & \times F_{\mathrm{Salin}}(T_p, M_p, W, B_i, \theta). \end{aligned} \quad (5.14)$$

where the last term is called the Salin's factor $F_{\mathrm{Salin}}(T_p, M_p, W, B_i, \theta)$, which semi-empirically accounts for the enhanced electron ejection at forward direction due to the electron capture to the continuum (ECC) process [18, 102, 103].

As stated in the work of de Vera et al. [25], the advantage of this method is that the knowledge of the ELF and the mean binding energy of the outer-shell electrons of the target material is enough for obtaining the DDCS. If the ELF for the material of interest is not experimentally known, it can be approximately predicted through an empirical parameterization for organic materials that only needs as input of the atomic composition and density [104]. Therefore, the method provides a good approximation of the DDCS for any organic material.

According to the work of de Vera et al. [24], the SDCS for ionization of the electronic i-shell yields:

$$\left.\frac{\mathrm{d}\sigma_{\mathrm{DRF}}}{\mathrm{d}W}\right|_i = \frac{e^2}{\pi\hbar^2\mathcal{N}}\frac{M_p Z_p^2}{T_p}\int_{k_-}^{k_+}\frac{\mathrm{d}k}{k}\,\mathrm{Im}\left[\frac{-1}{\epsilon(\hbar k,\hbar\omega)}\right]_i, \tag{5.15}$$

where the meaning of the symbols is identical to those in equation 5.12. The integration limits, $k_\pm = \sqrt{2M}\left[\sqrt{T_p} \pm \sqrt{T_p - (B_i + W)}\right]$, are imposed by conservation laws. Once the SDCS is known, the TICS can be obtained from integrating the SDCS and is given by de Vera et al. [24]:

$$\sigma_{\mathrm{DRF}} = \int_0^\infty \frac{\mathrm{d}\sigma_{\mathrm{DRF}}}{\mathrm{d}W}\mathrm{d}W. \tag{5.16}$$

Within the framework of this thesis, the ionization cross section data of THF have been calculated by de Vera [81] for proton energies between 300 keV and 3000 keV. Since there is no experimental information available for the ELF of THF, it has been obtained using the semiempirical parametric model [25]. It has to be noted that, apart from using an approximate ELF, another source of uncertainty is that this method is developed for condensed phase materials, while the experiments are performed in the gas phase.

5.3.3 Boundary-corrected first Born approximation

The ionization cross section data for proton energies below 300 keV have been calculated by Champion [80] within the B1 approximation with corrected boundary conditions for the initial and final wave functions. In this calculations the ejected electron is described by a Coulomb wave whereas the incident and the scattered projectiles are both described by plane waves. This approach will be hereafter referred to as the boundary-corrected first Born (CB1) approximation [27]. Champion et al. have successfully used this approach for investigating the ionization process induced by light bare ions on water molecule [27] as well as on different nucleobases [26].

Generally, in the PWBA framework, the outgoing electron is described by means of a plane wave function, so that the interaction between the outgoing electron and the target nucleus is neglected. Furthermore, the target electron is assumed to be a free electron which interacts with the incoming particle independent of the target. Accordingly, the ionization

process can be regarded as a binary-encounter electron emission, which may be described as a classic billiard-ball-like collision. However, this treatment would not be expected to be valid for collisions where the outgoing electron will feel the potential of the target nucleus. In the CB1 model, this is taken into account by the use of a Coulomb wave function for representing the ejected electron traveling in a continuum state of the target. In addition, a screened target potential is considered, which significantly improves the estimation of the cross sections for backscattering electrons. For this purpose, the electrons in the initial state are represented by individual atomic wave functions corresponding to the electrons in each target molecular subshell.

Chapter 6

Results and discussions

6.1 Introduction

This chapter presents the interaction cross section data sets obtained within this work, which are the cross section data for ionization of low-energy (75 keV–135 keV, see section 6.2, page 95) as well as high-energy (300 keV–3000 keV, see section 6.3, page 102) protons on the DNA constituents pyrimidine (PY), tetrahydrofuran (THF) and trimethyl phosphate (TMP). The experimental determination was performed using a double-differential measurement setup, which allows a detailed detection of both energy and angular distributions of emitted electrons. The range of emission angles and energies of secondary electrons covered in this work are detailed in table 4.1.

The measured energy spectra of secondary electrons were converted into absolute double-differential cross sections (DDCS), single-differential cross sections (SDCS) and total ionization cross sections (TICS) using different evaluation procedures (see section 4.2, page 64 and section 4.3, page 73). In this chapter, each type of ionization cross section is discussed in detail. The consistency and accuracy of the experimental data are examined through several theoretical calculations using the methods described in chapter 5. Results for the aforementioned samples are compared to scaled literature data of other molecules in order to test the concept of scalability for differential and total ionization cross sections (see section 6.5, page 110).

6.2 Differential cross sections for ionization by low-energy proton impact

6.2.1 Experimental DDCS spectra of secondary electrons

The complete data sets of experimental DDCS for electron emission from PY, THF and TMP by 75 keV, 105 keV and 135 keV protons are shown in figure 6.1 for various emission angles from 15° to 135°. Generally, the spectra exhibit a broadly decreasing electron yield from 10 eV to 200 eV. With increasing electron energy, the decrease becomes steeper. The binary-encounter peaks, where the collision between the proton and the subsequently emitted target electron can be approximately described as a two-body process (see section 2.2.2.2, page 17), are excepted to occur at electron energies $W_{\mathrm{BE}} = 4T_p\cos^2\theta \cdot (m_e/M_p)$. For protons of $T_p = 75\,\mathrm{keV}$, they are indicated with vertical arrows at electron energies 152 eV, 123 eV and 82 eV for emission angles of 15°, 30° and 45°, respectively. At a small emission angle $\theta = 15°$,

the region of electron capture to the continuum (ECC, see section 2.2.2.4, page 19) is still recognizable. In this process, electrons are released with velocities similar to those of the projectile ions and are essentially focused in the forward direction. Thus, the excepted range of ECC process is around the electron energy of $W \approx T_p \cdot (m_e/M_p)$, as indicated in figure 6.1 with the horizontal pair of arrows for PY by protons with $T_p = 75\,\text{keV}$.

In figure 6.1, it is also apparent that there is little variation in the measured cross sections for emission angles above 90°. This enhancement of electron production at backward angles may be attributed to the mechanism considered as inverse binary-encounter process (see section 2.2.2.2, page 17), where the roles of the projectile ion and the target electron are exchanged [1]. In this case, the momentum direction of the emitted electron may significantly be influenced by the Coulomb field of a relatively slow projectile. Consequently, the electron may leave the target atom with its initial velocity as it is elastically scattered by the quasi static field of a slow projectile [1].

Compared to protons in the MeV range (see section 6.3, page 102), the spectral for electron emission show less energy dependence below 60 eV. Such flattening of the DDCS for smaller electron energies was previously observed for proton impact between 50 keV and 150 keV on argon [82]. It is noted that all three samples show almost the same relative energy dependence of the DDCS for the proton energies investigated. This characteristic of the DDCS data will be discussed in detail in the subsequent sections.

6.2.2 Comparison of experimental and theoretical DDCS

Figure 6.2a compares the experimental DDCS of the gas targets PY, THF and TMP for 75 keV protons at emission angles of 15°, 60°, 90° and 135°. Generally, the relative energy dependence of three samples is almost identical. In absolute numbers, TMP with the largest number of valence electrons has a larger cross section compared to PY and THF. All electrons outside the core molecular orbital, whose typical bindings energies are several electron hundred eV, are counted as valence electrons. Their ionization energy lies between about 10 eV and 50 eV (see table 5.1, page 85). The number of valence electrons is 30 for PY and THF and 50 for TMP. The ratios of DDCS for PY/THF and TMP/PY (averaged over both electron

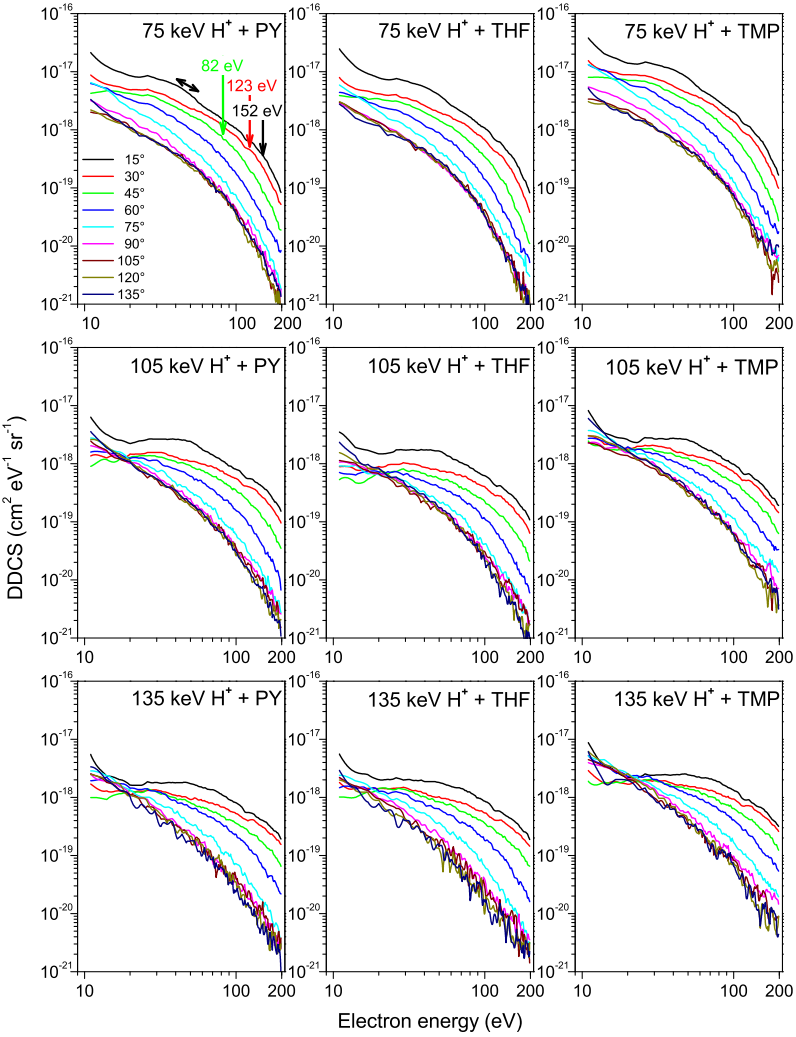

Figure 6.1 Measured (solid lines) double-differential cross sections (DDCS) for ionization of PY, THF and TMP by protons with incident energies of 75 keV, 105 keV and 135 keV. The energy spectra are shown as a function of secondary electron energy for the emission angles from 15° to 135° in steps of 15°. Vertical arrows indicate the energy of the binary-encounter peak, the horizontal arrow at 15° shows the expected range of electron capture to the continuum.

energy and emission angle, and weighted by the standard deviation of each data point) are 1.11 ± 0.03 and 1.69 ± 0.04, respectively. The ratios for the number of valence electrons are similar, namely 1.00 and 1.67. This indicates that the total ionization cross sections are well scalable with the number of valence electrons within the experimental uncertainties. In other words, the molecular structure has no significant influence on the total ionization cross section. It is therefore expected that the electronic structure of the target molecule is stronger reflected in differential cross sections.

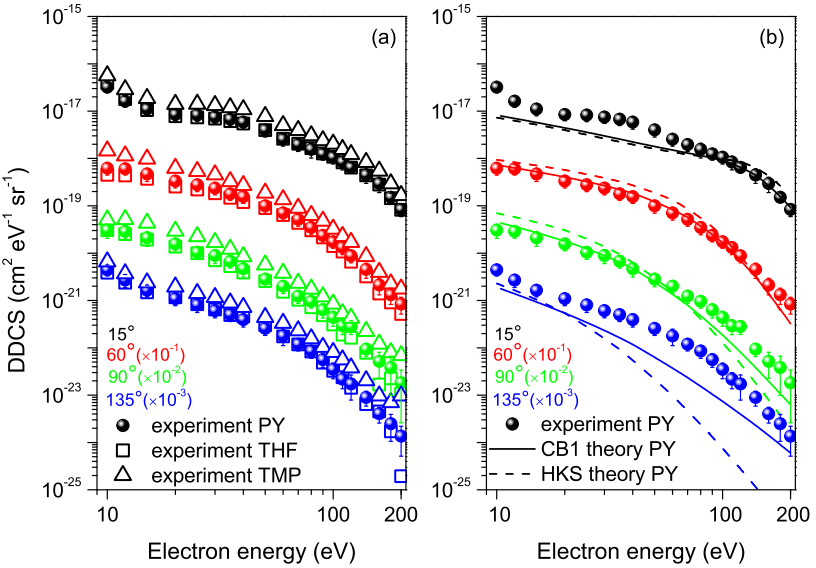

Figure 6.2 Experimental double-differential cross sections (DDCS) for ionization of PY (dots) by 75 keV protons in comparison to: (**a**) the experimental DDCS of THF (open squares) and TMP (open triangles); (**b**) the theoretical DDCS obtained using the CB1 model [27] (solid line) and the HKS model [23] (dashed line). The results are shown as a function of secondary electron energy for the emission angles of 15°, 60°, 90° and 135°. For improved readability, the data of different emission angles are multiplied by the indicated factor.

In figure 6.2b, the experimental results are compared with the semi-empirical HKS model modified by Bernal and Liendo [23] and the quantum mechanical CB1 calculations by Champion et al. [27], which are both described in chapter 5. The CB1 calculations show an overall better

agreement with the experimental results. In the forward direction of 15°, both models are in good agreement with the experimental data around the binary-encounter peak. At low electron energies, however, they underestimate the cross section by as much as a factor of 2, where the electron emission from two-center effects plays a role. It should be noted that at 15° the enhanced DDCS is attributed to the ECC process, which is not accounted for in the theory. At emission angles of 60° and 90°, the CB1 model agrees quite well with the measured results within the experimental uncertainties over the entire energy range, whilst the HKS calculations are only in good agreement in the energy region around the binary-encounter peak.

At a large angle of 135°, the CB1 model reproduces the relative energy dependence but underestimates the cross section between 50 eV and 150 eV. The HKS model, on the other hand, exhibits more deviations with increasing electron energy. At a relative large energy transfer ($W > 150\,\text{eV}$), the discrepancy between the HKS calculation and experimental data is larger than a factor of 10. This disparity originates from the backscattering of high-energy electrons in the target center (see section 2.2.2.3, page 18). Electron emission in backward directions is due to a scattering at the full nucleus charge rather than at the smaller effective charge [1]. The strong electron-target backscattering is therefore underestimated by the HKS model using a simplified description based on the hydrogenic wave functions.

6.2.3 Comparison of experimental and theoretical SDCS

In figure 6.3a, the experimental SDCS of the target molecules PY, THF and TMP are compared for proton energies of 75 keV, 105 keV and 135 keV. For all three molecules, the relative energy dependence of the SDCS shows a similar trend, that is the cross sections are highest at 10 eV and continuously decrease for higher emission energies of secondary electrons. In view of the absolute values, the experimental data are higher at lower proton energies, but decrease more rapidly. The SDCS of TMP, which has the largest number of valence electrons, are consistently higher by a factor of about 1.5 than the other two target molecules. For THF and PY, which have the same number of valence electrons, the SDCS at proton impact energies of 75 keV and 135 keV are about the same. For protons of 105 keV, the SDCS of THF are mostly within the experimental uncertainties of the PY data.

Figure 6.3b shows the experimental SDCS of PY at proton energies of 75 keV, 105 keV and 135 keV for electron energies up to 200 eV, along with the theoretical calculations using the HKS and CB1 models. The agreement of experimental data and theoretical calculations is very good for 75 keV proton impact. At larger proton energies, especially at 105 keV, the experimental SDCS are lower than the theoretical values for electron energies below 60 eV, whilst a good agreement can be seen for electron energies between 60 eV and 200 eV. This reduced detection of slow electrons at 105 keV proton energy may result from a sub-millimeter shift in the ion beam position with respect to the spectrometer.

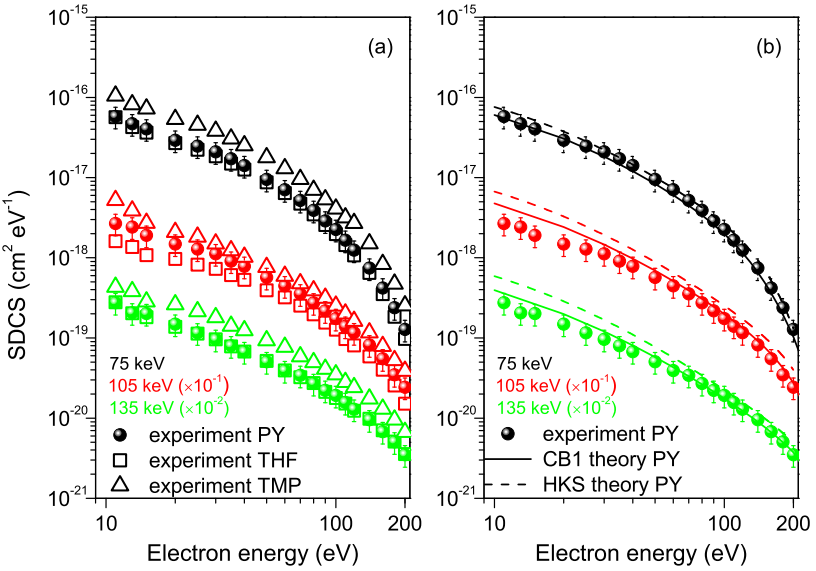

Figure 6.3 Experimental single-differential cross sections (SDCS) for ionization of PY (dots) by protons with incident energies of 75 keV, 105 keV and 135 keV in comparison to: (**a**) the experimental SDCS of THF (open squares) and TMP (open triangles); (**b**) the theoretical SDCS obtained using the CB1 model [27] (solid line) and the HKS model [23] (dashed line). The results are shown as a function of secondary electron energy. For improved readability, the data for the different proton energies are multiplied by the indicated factor.

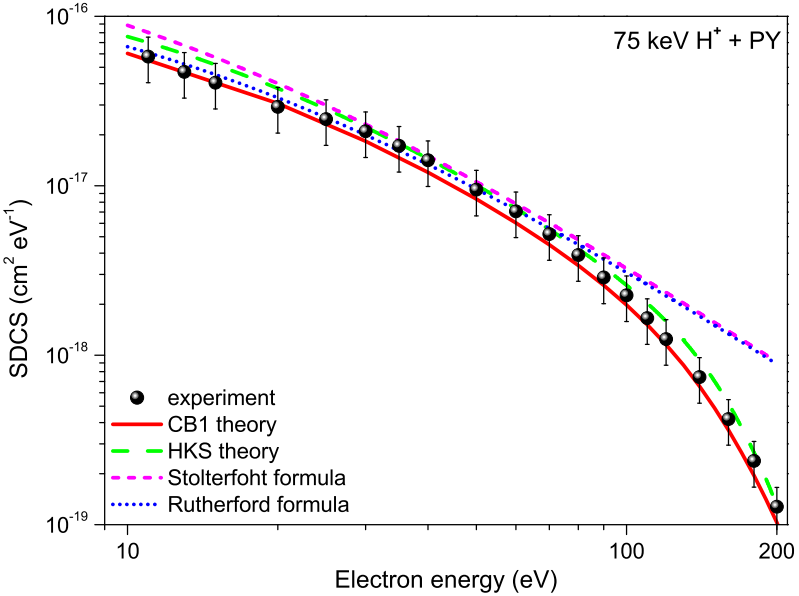

Figure 6.4 Experimental (dots) single-differential cross sections (SDCS) for ionization of PY by 75 keV protons in comparison to several theoretical calculations: Rutherford formula (blue dotted line), Stolterfoht modification (pink short dashed line), the HKS model [23] (green dashed line) and the CB1 model [27] (red solid line). The results are shown as a function of secondary electron energy.

In figure 6.4, the experimental SDCS of PY at 75 keV proton energy are also compared to the theoretical SDCS using the Rutherford analytical formula (see equation 5.2, page 83) and the Stolterfoht's modification (see equation 5.3, page 84). The simple analytical formula of the Rutherford model appears to overestimate the SDCS at electron energies above 100 eV. Since electrons produced in soft collision are included in Stolterfoht's modification, larger Rutherford cross sections occur below 50 eV, resulting in a poorer agreement with the experimental results. Hence, it is questionable to employ these two classical methods to predict the SDCS for electron energies larger than 100 eV. The HKS model, on the other hand, reproduces the energy dependence of the SDCS despite slightly overestimating it at small electron energies below 30 eV. In comparison, the CB1 calculation provides the best modeling of the experimental data.

6.3 Differential cross sections for ionization by high-energy proton impact

6.3.1 Experimental DDCS spectra of secondary electrons

In section 6.2, the experimental DDCS and SDCS of the molecules THF, PY and TMP are compared for lower proton energies and a similar energy dependence of the cross section data was found. This finding led to further cross section measurements at higher proton energies with only THF for two reasons: firstly, differences in angular and energy dependencies are expected to be rather less pronounced at higher proton energies as the structural dimensions of the target molecule are much larger than the projectile's wave length; and secondly, due to limited beam time, so measurements of a larger range of proton and secondary electron energies could be achieved.

The complete data sets of experimental DDCS for electron emission from THF by proton impact with energies between 300 keV and 3000 keV are shown in figure 6.5 for various emission angles between 15° and 150° in steps of 15°. These DDCS spectra of secondary electrons generally decrease with increasing secondary electron energy, becoming noisy at higher electron energies. The noise is due to the poor statistics caused by a lower ionization cross section and smaller spectrometer transmissions from using higher CRR values of up to 4. Auger peaks of carbon and oxygen are pronounced features in the DDCS of THF at electron energies between 200 eV and 300 eV and between 400 eV and 500 eV, respectively. As the primary proton energy increases, the velocity of the incident proton is much larger than the mean orbital velocity of the target electron. In this case the reversed binary-encounter process is negligible for collisions with fast projectiles. The DDCS spectra for backscatter angles ($\theta > 90°$) can thus be distinguished from each other.

6.3.2 Comparison of experimental and theoretical DDCS

In figure 6.6, the experimental DDCS of THF are compared to those obtained theoretically by the HKS model [23] and the DRF model [25] for protons with incident energies of 1200 keV. Both theoretical models reproduce the general trends of the experimental data. Auger electrons

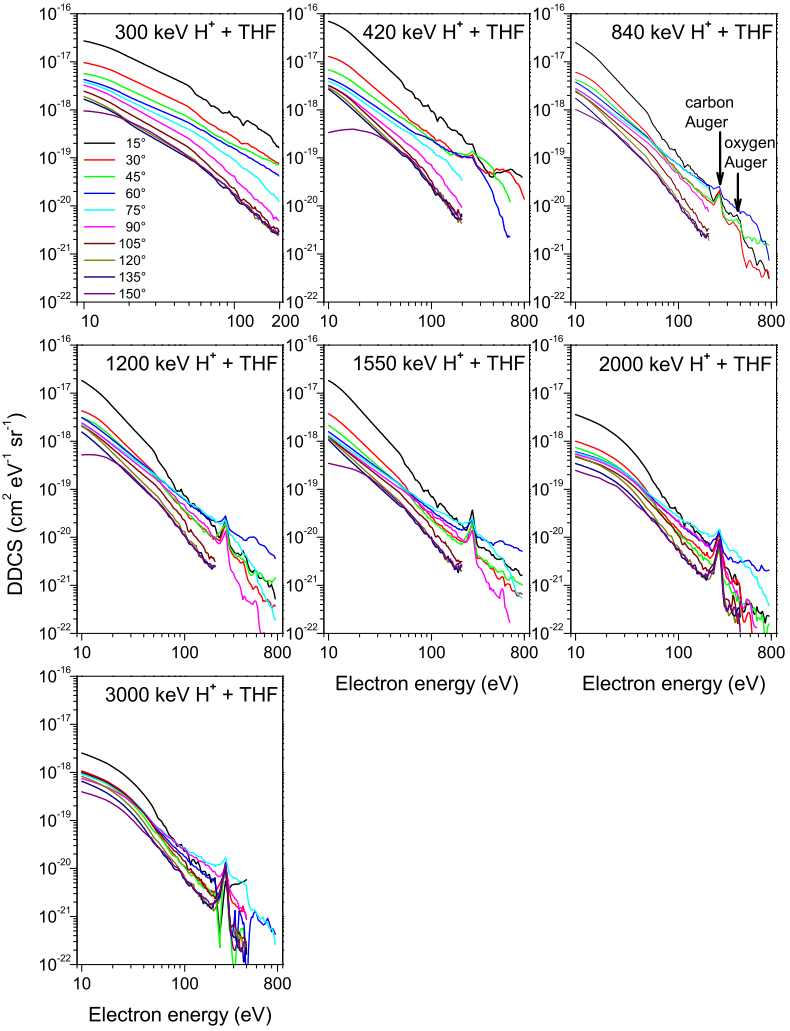

Figure 6.5 Measured (solid lines) double-differential cross sections (DDCS) for ionization of THF by protons with incident energies of 300 keV, 420 keV, 840 keV, 1200 keV, 1550 keV, 2000 keV and 3000 keV. The energy spectra are shown as a function of secondary electron energy for the emission angles from 15° to 150° in steps of 15°. Labels indicate the location of the Auger peaks of carbon and oxygen at electron energies between 200 eV and 300 eV and between 400 eV and 500 eV, respectively.

ejected from carbon and oxygen atoms occur between 200 eV and 300 eV and between 400 eV and 500 eV, respectively. These Auger processes are not accounted for in the theoretical calculations.

At an emission angle of 15°, both theoretical models predict lower absolute values, especially at electron energies below 100 eV. The experimental data are larger than the DRF data and HKS data by up to a factor of 3 and 15, respectively. The DRF data, on the other hand, are in better agreement with the experimental results at small angle of 30°. This better agreement may result from the consideration of a more realistic electronic excitation spectrum of THF, which is accounted for in the DRF calculation with the use of the energy loss function. In the HKS model, the target electron is described by a hydrogenic wave function, and hence, its electronic excitation spectrum is described in a less accurate way. The agreement between the HKS and DRF models improves at emission angles between 45° and 105°. As can be seen from figure 6.6, both models reproduce the energy dependency of the experimental data for secondary electron energies up to 800 eV.

At large emission angles between 120° and 150°, the agreement between both theoretical calculations and measurements is acceptable at low electron energies ($W < 50\,\text{eV}$), but reduces remarkably with increasing electron energy (up to a factor of 50 at $W = 200\,\text{eV}$ and $\theta = 150°$). Furthermore, both models fail to predict cross sections of collisions involving larger emission angles and high energy transfer ($W > 100\,\text{eV}$). This discrepancy, which is caused by the target center effects, has also been discussed for a low proton energy of 75 keV. Since the binary-encounter peak position is used in the DRF model to determine the position of the maximum DDCS, the theorectical values have greater uncertainties in the angular region far from the binary peak [25]. The hydrogenic wave function used in the HKS model also leads to a screening of the nucleus charge [23].

In figure 6.7a, the angular dependence of DDCS for THF for proton impact with energy of 1200 keV is depicted for selected electron energies. In the region of emission angles between 45° and 90°, the binary-encounter peak is a dominant feature. This is a direct consequence of hard collisions (see section 2.2.2.2, page 17) for which there is a large energy transfer from the projectiles to target electrons [18]. Both models are based on

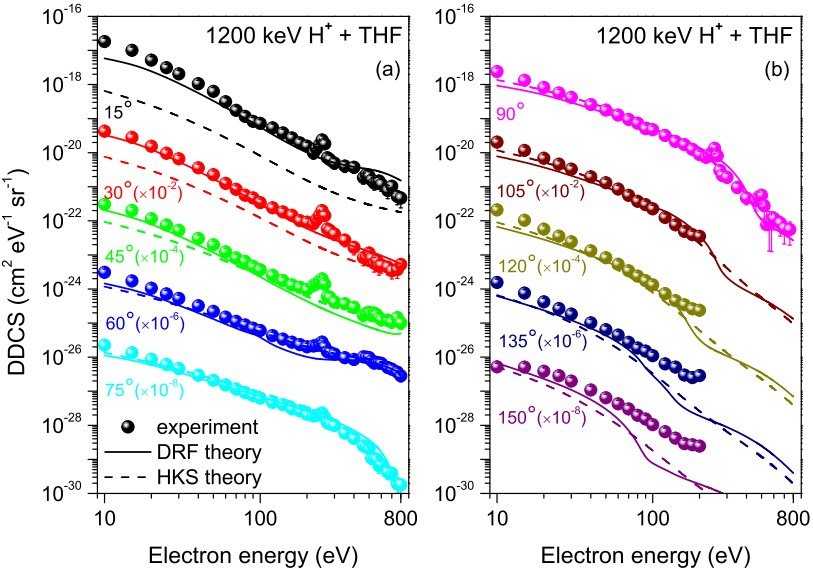

Figure 6.6 Experimental (dots) double-differential cross sections (DDCS) for ionization of THF by 1200 keV protons in comparison to the theoretical DDCS obtained using the DRF model [25] (solid line) and the HKS model [23] (dashed line) for different emission angles: (**a**) in forward directions from 15° to 75°; and (**b**) in backward directions from 90° to 150°, in steps of 15°. The results are shown as a function of secondary electron energy. For improved readability, the data of different emission angles are multiplied by the indicated factor.

the B1 approximation (see section 5.3, page 86) and they are expected to agree well with the experimental DDCS over this angular range. The DRF model predicts a fairly good description of the experimental data over this angular range, except for some data points at 45°, which are underestimated, particularly for electron energies above 200 eV. The HKS model, on the other hand, is able to reproduce the peak position but generally overestimates the maximum by up to a factor of 2.

Since the B1 approximation does not take two-center effects into account, it is unable to reproduce the process of ECC. In this process, electrons ejected from the target with velocities similar to those of the projectile ions are attracted by the leaving ions. Thus, they are essentially focused

in forward direction. In the DRF calculation using equation 5.14, the two-center effect was considered by the introduction of Salin's factor [102]. This is a multiplicative factor, which is essentially proportional to $|\vec{v}_p - \vec{v}_e|^{-1}$, where $\vec{v}_p$ and $\vec{v}_e$ are the velocities of the projectile ion and the secondary electron, respectively. Thus, this factor enhances the DDCS when $\vec{v}_e$ approaches $\vec{v}_p$. For example, as seen in Fig. 6.7b, for 1200 keV protons, the introduction of Salin's factor improves the predicted DDCS in the forward direction. This is particularly evident for electron energies with velocities comparable to that of the incoming proton (e.g. $W = 500$ eV) and also for electrons with lower energies (e.g. $W = 50$ eV), which experience the potentials of both target and outgoing proton simultaneously.

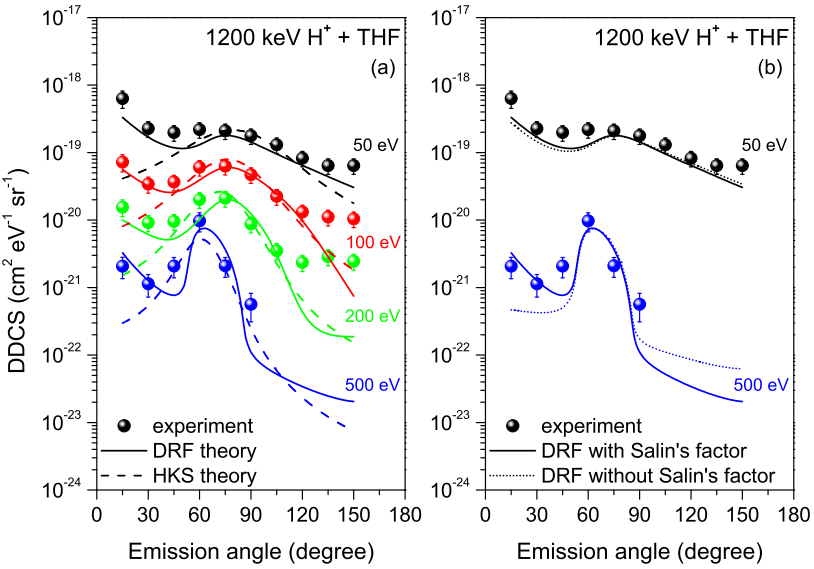

Figure 6.7 Experimental (dots) double-differential cross sections (DDCS) for ionization of THF by 1200 keV protons in comparison to: (**a**) the theoretical DDCS obtained using the DRF model [25] (solid line) and the HKS model [23] (dashed line); (**b**) the theoretical DDCS obtained using the DRF model [25] with and without Salin's factor [102] in solid and dotted line, respectively. The results are shown as a function of emission angle for secondary electron energies 50 eV (black), 100 eV (red), 200 eV (green) and 500 eV (blue).

6.3.3 Comparison of experimental and theoretical SDCS

Figure 6.8 shows a comparison of the experimental results of THF with the corresponding theoretical calculations based on the HKS model [23] and the DRF model [24]. As the SDCS was governed by electrons from the binary-encounter and soft collisions, differences in the backward scattering that were observed in DDCS have little influence here. The experimental results are in good agreement with the DRF calculations over a wide range of incident proton and secondary electron energies. The HKS model, on the other hand, underestimates the SDCS by up to a factor of 2 for electron energies $W \leq 50\,\text{eV}$. Auger electron peaks from carbon were observed in the experimental spectra at about $W = 250\,\text{eV}$ for proton energies of 2000 keV and 3000 keV. The discrepancy observed in the region around $W = 200\,\text{eV}$ for 420 keV protons may be due to the contribution from electrons involved in the ECC process, as for 420 keV protons the left wing of the ECC peak (around 230 eV) is within the measured energy range. However, if this is the case, then one would expect this effect of ECC to also occur around 160 eV for 300 keV protons.

6.4 Total cross sections for ionization by proton impact

The experimental TICS of PY, THF and TMP, together with several theoretical calculations, are shown in figure 6.9a, 6.9b and 6.9c, respectively. The experimental data are depicted as black dots, whilst the theoretical values are show as a function of incident proton energy. For all samples, TICS at 105 keV and 135 keV proton energy are lower than the 75 keV data. The 50% reduction at 105 keV may arise from a slight shift in the proton beam position. In general, the normalization factor (see section 4.2, page 64) derived from the absolute cross sections of electron beam impact may offset the absolute scale of proton beam data as it assumes the beam dimensions to be equal.

The experimental TICS of all three samples in figure 6.9 were also compared to Stolterfoht's analytical formula for TICS (equation 5.5). These calculated TICS using this formula agree well with experimental data as well as other theoretical values above 500 keV. This supports the previous suggestion of using such a calculation to estimate the TICS of polyatomic molecules, such as adenine [31]. The TICS were also compared to those

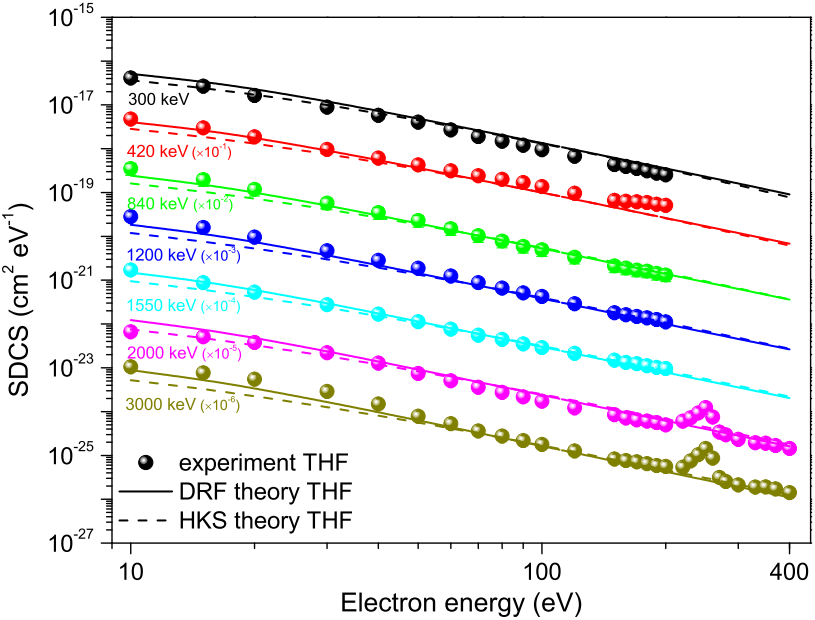

Figure 6.8 Experimental (dots) single-differential cross sections (SDCS) for ionization of THF by protons with incident energies between 300 keV and 3000 keV. The data were obtained from the DDCS by numerical integration over the solid angle. The theoretical SDCS calculated using the DRF model [25] (solid line) and the HKS model [23] (dashed line) are also shown for different proton energies. For improved readability, the data for the different proton energies are multiplied by the indicated factor.

from electron-impact experiments [22], which used primary electrons with the same velocity as the protons. The TICS data of equal-velocity electron impact decrease with decreasing incident energies below about 100 eV, which corresponds to proton energies between 150 keV and 200 keV. As pointed out by Rudd et al. [89], this decrease in electron impact for lower energies is caused by several effects, such as the exchange effect between the incident and bound electrons which generally reduces the production of ejected electrons. Such effects lead to a larger TICS for proton impact than that for equal-velocity electron impact. In comparison, the HKS approach has a maximum TICS at around 50 keV, whilst for Stolterfoht's formula and the CB1 model

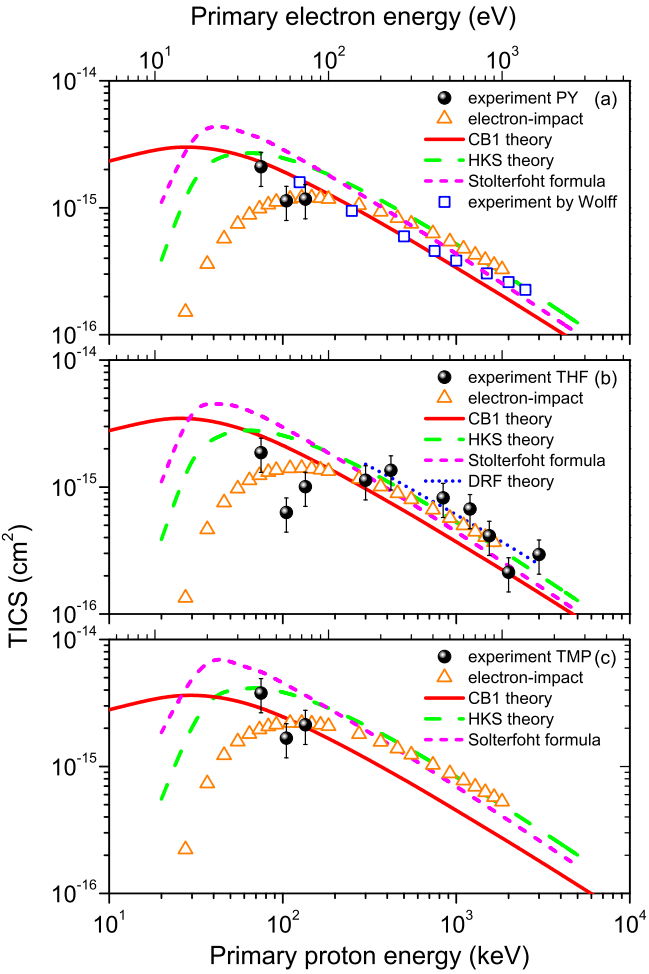

Figure 6.9 Experimental (black dots) total ionization cross sections (TICS) of (**a**) PY, (**b**) THF and (**c**) TMP in comparison to several theoretical calculations: Stolterfoht formula (pink short dashed line), the HKS model [23] (green dashed line) and the CB1 model [27] (red solid line). For PY, the TICS derived by Wolff et al. [105] from ion-induced fragmentation are plotted in blue squares. For THF, the TICS obtained using the DRF model [24] are depicted as a blue dotted line for proton energies between 300 keV and 3000 keV. Experimental TICS for electron-impact [22] are displayed in orange and the corresponding energy axis is on top of the graph.

a maximum can be seen at around 40 keV. At higher incident energies, the cross sections of electron-impact are expected to approach those of protons traveling at the same speed [89]. In figure 6.9, for all of three samples, the electron-impact TICS coincide with those obtained using the HKS approach for proton energies between 400 keV and 2000 keV.

For THF, the experimental TICS at 75 keV agree well with the electron-impact data as well as those obtained using the CB1 and HKS calculations. The TICS of THF at 105 keV and 135 keV, however, seem to be underestimated. For higher energies between 300 keV and 3000 keV, TICS values calculated using the DRF model [24] are also shown. At MeV energies, the experimental proton-impact results are in good agreement with the DRF theory and electron-impact data, whilst the CB1 calculation is generally lower than experimental data (except for the data point at 2000 keV) by up to factor of 2.

In the case of PY, TICS derived from the fragmentation cross sections measured by Wolff et al. [105] show a good agreement with the present results, especially at proton energies around 130 keV. Compared to theory, the TICS obtained with the CB1 approach agree well with the experimental values for 75 keV as well as the data of Wolff et al. [105] between 125 keV and 1000 keV. The experimental TICS of proton impact with energy of 125 keV are similar to the electron-beam data, but up to a factor of 2 lower than those values obtained with the CB1 calculations.

TMP has the largest TICS of all three samples due to its greater number of valence electrons. The values obtained using CB1 theory agree well with the experimental data around 100 keV, but underestimate the electron-impact data at higher proton energies. The TICS values obtained using Stolterfoht's formula converge to the electron-impact data for energies between 100 keV and 500 keV.

6.5 Scaling property of differential and total ionization cross sections

The scalability of cross sections in terms of the number of valence electrons n_v is well-known as a semi-empirical rule used to estimate the cross sections for complicated molecules based on the literature data for simple target systems. From the previous study of several molecules such as water

molecule [47], numerous hydrocarbons [106] and amines [107], it was found that the cross sections for the molecules studied can be scaled by a common cross section, which was derived from the molecular cross sections divided by the number of weakly bound electrons n_v (i.e. all electrons except K-shell electrons). Only molecules containing elements with low atomic number ($Z_p < 10$) have been investigated. Molecular hydrogen [108] was found to be the one exception for successfully applying the scaling technique among the molecules studied. The cross sections of hydrogen exhibited a much sharper angular distribution near the binary-encounter peak than that of other more complex molecules. A comparison of the cross sections obtained for DNA constituents to these obtained for hydrogen is therefore also shown in this section.

Recently, the scaling property of ionization cross sections has been extended to complex biological molecules such as uracil [30] and adenine [29, 31], belonging to the nucleobases of RNA or DNA. The uracil and adenine comprise 42 and 50 bound electrons, respectively. Since the number of bound electrons for hydrocarbons and amines is usually less than 30, one must include the experimental data of uracil and adenine to cover large n_v values.

It should be noted that all experimental investigations to date [29–31, 47, 106–108] have been performed at least for proton energies above 0.25 MeV. Using these data, the aforementioned scaling method (with the number of valence electrons in molecules) was verified to be a good approximation of these ionization cross sections. This approximation seems valid for proton impact at MeV energies where a fast charged proton predominantly interacts with the weakly bound valence electrons [47]. To check the reliability of the scaling procedure at low proton energies, a comparison was made between the cross sections for THF and the literature data for other molecules at incident energies of a few hundred keV.

6.5.1 Angular distribution of cross section data

From figure 6.2, the experimental data of PY, THF and TMP were shown to exhibit a similar energy distribution of secondary electrons at 75 keV proton energy. It is important to note that all three targets have a similar molecular composition, particularly for THF and PY which have

a similar ring structure. Thus, a comparison of the angular distribution for PY and other simple targets is presented in figure 6.10, where the DDCS for molecular hydrogen [12] and argon [82] are plotted for 75 keV and 70 keV proton energy, respectively. Unfortunately, the experimental data for other complex molecules at this energy are not available.

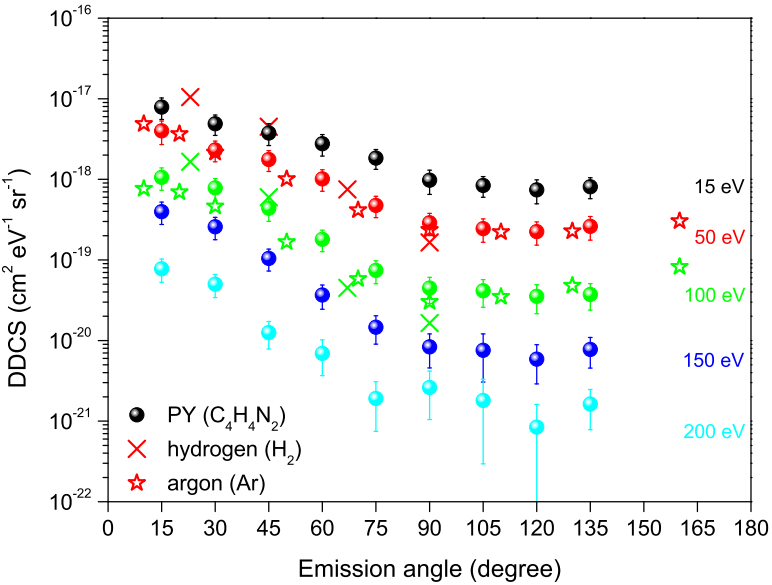

Figure 6.10 Experimental double-differential cross sections (DDCS) for ionization of PY (dots) by 75 keV protons. The results are shown as a function of emission angle for a sequence of secondary electron energies from 15 eV to 200 eV. For 50 eV and 100 eV, the DDCS of PY are compared to those of hydrogen [12] (cross) by 75 keV protons and argon [82] (open star) by 70 keV protons. The data sets of hydrogen and argon were scaled with a factor of 30/2 and 30/8 representing the ratio of the number of valence electrons.

For all secondary electron energies, the DDCS is largest for emission angles in forward directions, where it then decreases steadily towards 90° before either flattening out or slightly increasing. The same behavior can be seen for rare gases [109], water [50], methane and ammonia [107] around 100 keV. Resolving equation 2.5, the angular distribution with a dependency in form of $\cos^2\theta$ is expected to be symmetric around 90° [1]. The observed asymmetry at low incident energies is mainly due to the

influence of two-center effects (see section 2.2.2.4, page 19). These effects are expected to increase with decreasing projectile energy, since two-center effects are governed by the Bohr parameter Z_p/v_p which is a measure for the perturbation strength of the projectile [1]. Therefore, for a low projectile energy, these effects give a clear enhancement at forward angles where the outgoing electrons are attracted by the receding projectile. In summary, electrons with energies below 200 eV ejected by impact of slow protons are mostly in the forward direction.

The scaling property of DDCS for larger molecules has so far only been investigated at higher proton energies. For example, the scaling of adenine for 1 MeV protons has been reported by Iriki et al. [29]. According to this investigation, the angular distributions of secondary electrons for adenine deviate significantly from those for simple targets, i.e. molecular hydrogen at emission angles smaller and larger than the binary-encounter peak. These discrepancies are due to the differences in the momentum distribution of the respective target electrons. Iriki et al. found a better agreement when comparing the adenine distributions to those of different hydrocarbon molecules where their momentum distributions were more alike. Nevertheless, for 1 MeV protons, the angular distribution of secondary electrons are still slightly broader for adenine compared to those of hydrocarbons, and large discrepancies are expected for protons of lower velocities due to a large contribution of two-center effects. Disagreements between adenine data for 1 MeV protons [29] and the calculation of de Vera et al. [25] can also be seen at emission angles outside the range of the binary-encounter peak. An extended comparison to other complex targets as well as lower proton energies is therefore needed.

Figure 6.11 shows the angular distribution of experimental data for THF (C_4H_8O, $n_v = 30$) at electron energies 15 eV, 50 eV, 200 eV and 500 eV by protons of 105 keV, 300 keV, 1550 keV and 2000 keV. These THF data are compared to the data of hydrogen (H_2, $n_v = 2$) [12, 108], water vapor (H_2O, $n_v = 8$) [47, 50], ethane (C_2H_6, $n_v = 14$) [106], benzene (C_6H_6, $n_v = 30$) [106], uracil ($C_4H_4N_2O_2$, $n_v = 42$) [30] and adenine ($C_5H_5N_5$, $n_v = 50$) [31]. The DDCS of the respective molecules were multiplied by the ratio of the number of the valence electrons of THF to that of their valence electrons.

Generally, the data for molecular hydrogen differ from those for other polyatomic molecules at small and large emission angles. The emitted secondary electrons from hydrogen are more anisotropic than those from other molecules, which is due to the broader momentum distribution of the target electrons in polyatomic molecules compared to hydrogen [106].

Benzene has the same number of valence electrons and a ring structure similar to that of THF, whilst ethane does not. Ethane, nonetheless, shows a similar scaled DDCS. As Wilson and Toburen [106] pointed out, neither angular nor energy distributions within the hydrocarbon groups at high proton energies are influenced very much by the variations in molecular bondings, namely, C−H bonds, single, double and triple C−C bonds, and the chemical structure. Compared to THF at proton energies $T_p \geq 300\,\text{keV}$, most of these polyatomic molecules have different numbers of valence electrons and individual chemical structures. Despite this, the angular distribution of scaled data for these molecules shows a reasonable agreement for a wide range of emission angles except for $\theta = 15°$, where the DDCS of THF is significantly higher than that of other molecules particularly at low electron energies. As can be seen from figure 6.7a, this increase in the angular distribution for THF at forward angles is also predicted in the DRF calculation rather than in the HKS calculation as the former model considers the two-center effects by introducing the Salin's factor. However, such a large increase of up to a factor of 10 between the DRF data and experimental results at 15° was not expected and requires further investigation.

An asymmetric angular distribution of THF, which is similar to that of PY in figure 6.10, is observed at a proton energy of 100 keV. This asymmetry, which is unlike to the behavior at larger proton energies, suggests that two-center effects are most important for the redistribution of electron intensity for proton energies as low as 100 keV [1]. At an electron energy of 50 eV, the reduction of DDCS for THF at small angles is due to a sub-millimeter shift in the ion beam position, as explained previously.

At a proton energy of 300 keV, the THF results exhibit a less-peaked angular distribution than hydrocarbons, which is more similar to that of water vapor. The reason for this is the target electrons in the outer orbitals of THF and water molecules have higher average kinetic energies than those of hydrocarbons, resulting in a broader momentum distribution, and

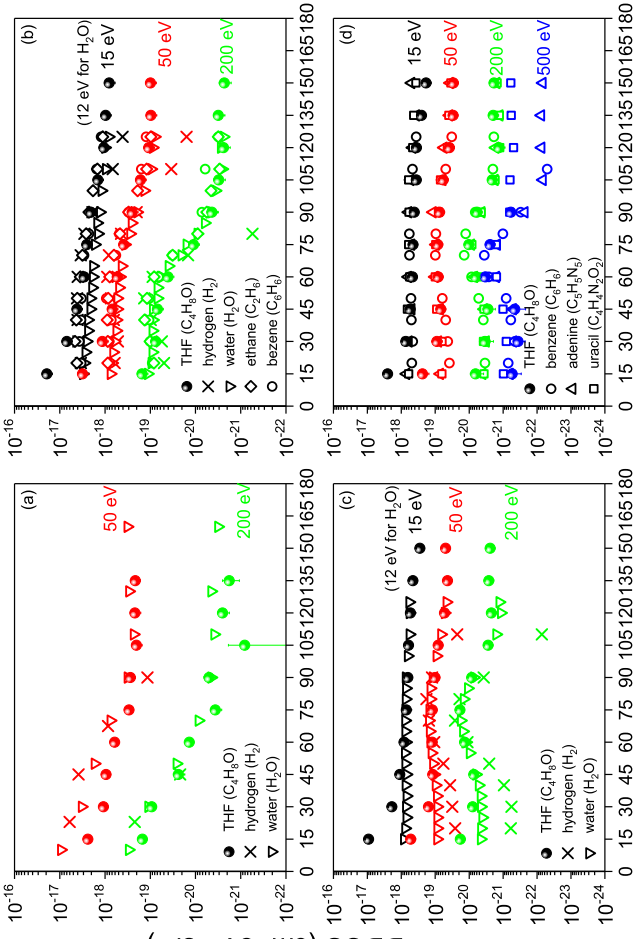

Figure 6.11 Experimental double-differential cross sections (DDCS) for ionization of THF (dots) by protons with incident energies of (**a**) 105 keV, (**b**) 300 keV, (**c**) 1550 keV and (**d**) 2000 keV. The results are compared to the DDCS of hydrogen [12, 108], water [47, 50], ethane and benzene as hydrocarbons [106], adenine [31] and uracil [30] for different proton energies: (**a**) 100 keV, (**b**) 300 keV, (**c**) 1.5 MeV and (**d**) 2 MeV. The data are shown as a function of emission angle for secondary electron energies 15 eV (black), 50 eV (red), 200 eV (green) and 500 eV (blue). The data sets of other molecules were multiplied by the ratio of the number of valence electrons of THF to that of their valence electrons.

thus, initial velocity distribution [2]. This broadening effect means that the electrons are emitted over a relatively wide angular range [1]. The difference in angular distributions of water and hydrocarbons has been intensively studied by Wilson and Toburen [106]. Unfortunately, Iriki et al. [29] did not include their data at 0.5 MeV in the comparison, which may have shed light on the difference in the angular distribution due to the lower proton energy, and hence, greater contribution of two-center effects.

As the incident proton energy increases, the angular distribution of lower electron energies appears more isotropic since those electrons below a few tens of eV are produced predominantly by soft collisions. For higher electron energies, the binary-encounter peak becomes relatively more apparent and sharper. This is due to the decreasing influence of the binding energy on the target electron, where the binding energy becomes negligible compared to the energy transferred in a hard collision. At a proton energy of 2000 keV, a comparison of the experimental data for THF to those for other complex targets reveals that they are almost identical at electron energies of 15 eV, 50 eV and 200 eV. The disagreement between uracil and the other molecules at higher electron energy $W = 500$ eV, especially for large angles $\theta \geq 105°$, arises from the Auger electron emissions of the oxygen atom in the uracil molecule.

6.5.2 Energy distribution of cross section data

The energy dependence of DDCS by proton impact of 2000 keV is briefly described. The experimental DDCS of THF are compared to those of adenine [31] and uracil [30]. To enable a comparison independent of the molecular size, the data sets of adenine and uracil were scaled with a factor 30/50 and 30/42, respectively, representing the ratio of the number of valence electrons. As depicted in figure 6.12, the experimental DDCS of THF agree well with the scaled data of adenine and uracil.

As shown in figure 6.13, in order to check the scalability of SDCS at few hundred keV protons, the data for THF are compared to those for adenine [29, 31] and uracil [30] multiplied by the ratio of the number of THF valence electrons to that of their valence electrons. The nitrogen Auger peak occurs at about $W = 350$ eV, since both adenine and uracil contain nitrogen. The SDCS for ionization of THF by 2000 keV proton impact are

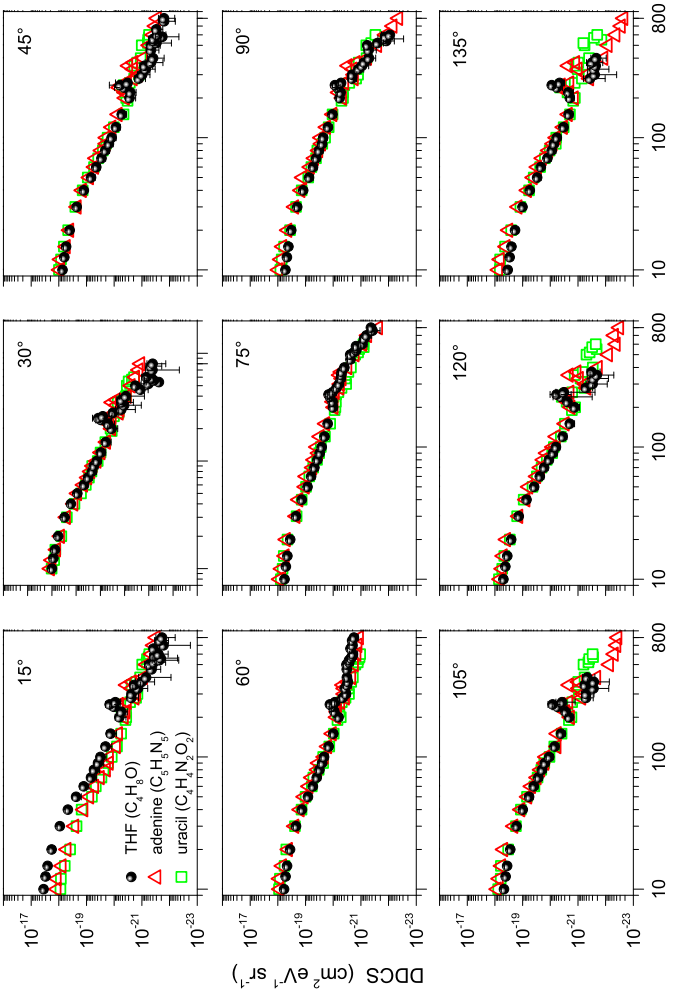

Figure 6.12 Experimental double-differential cross sections (DDCS) for ionization of THF (black dots) by 2000 keV protons in comparison to the DDCS of adenine (red open triangles) [31] and uracil (green open squares) [30]. The data are shown as a function of secondary electron energy for a sequence of emission angles from 15° to 135° in steps of 15°. The data sets of adenine and uracil were scaled with a factor 30/50 and 30/42 representing the ratio of the number of valence electrons.

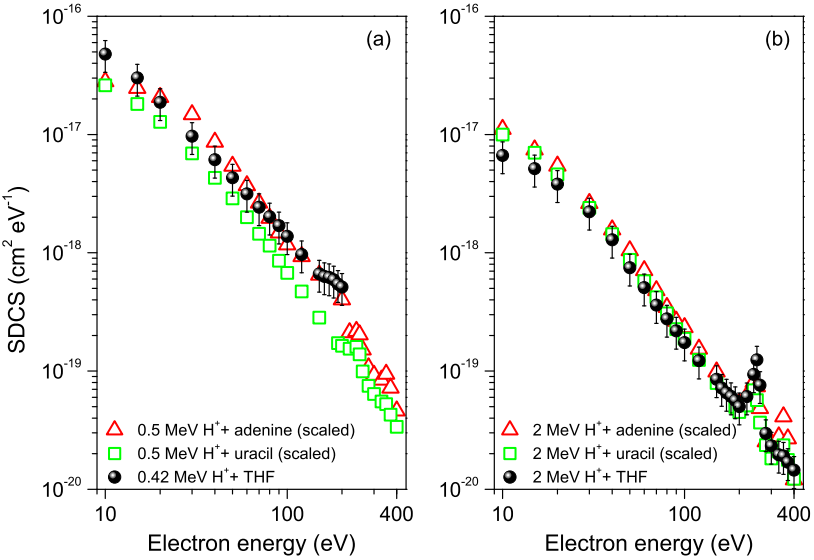

Figure 6.13 Experimental (black dots) single-differential cross sections (SDCS) for ionization of THF by protons with incident energies of (**a**) 420 keV and (**b**) 2000 keV. The results are compared to the SDCS of adenine [29, 31] (red open triangles) and uracil [30] (green open squares) for different proton energies: (**a**) 0.5 MeV and (**b**) 2 MeV. The data sets of adenine and uracil were multiplied by the ratio of the number of the valence electrons of THF to that of their valence electrons.

in good agreement with those of uracil except at $W = 10$ eV, where the latter are higher by a factor of 2. When the data for ionization of THF by 420 keV protons are compared to literature data for 0.5 MeV proton energy, a good agreement between the data for THF and the scaled data for adenine is observed for electron energies above 50 eV. At lower electron energies ($W < 50$ eV), however, they disagree by up to a factor of 2. The scaled SDCS of uracil are consistently lower than those of adenine for 0.5 MeV protons, which suggests that the scaling procedure may be inadequate for representation of electron spectra at proton energies around 0.5 MeV. From figure 6.3a, the SDCS of THF were scalable to those of TMP and PY at 75 keV and 135 keV protons. This conflict implies that it may be questionable to apply the scaling procedure to protons below the MeV-range, as addressed by Toburen and Wilson [47] in the study of water molecules.

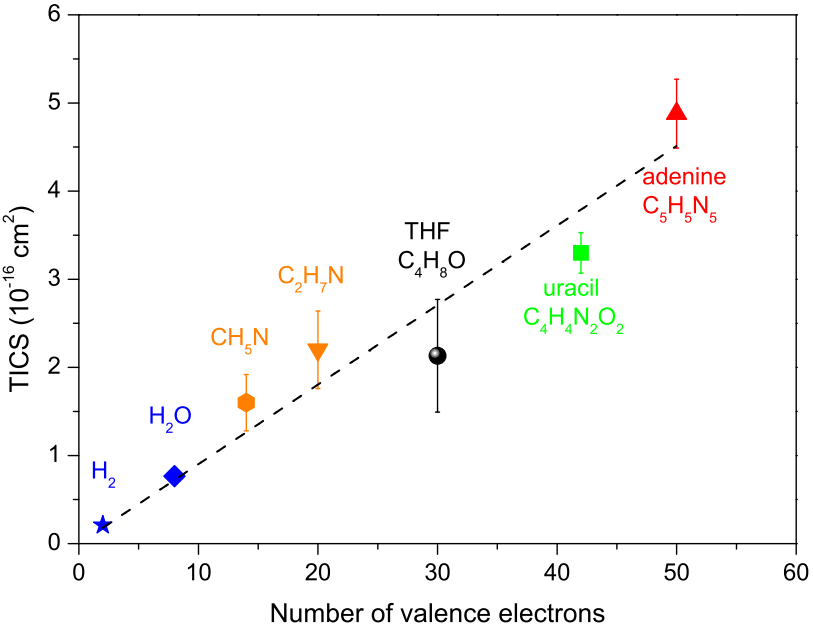

Figure 6.14 Experimental total ionization cross sections (TICS) of various molecules by 2 MeV protons as a function of the number of valence electrons. The data are taken from [89] for molecular hydrogen (H_2), from [48] for water (H_2O), from [107] for monomethylamine (CH_5N) and dimenthylamine (C_2H_7N), from [30] for uracil ($C_4H_4N_2O_2$) and from [31] for adenine ($C_5H_5N_5$). The TICS of THF is also plotted.

Finally, a brief discussion is given for the scaling property of TICS, which is expected to be proportional to the number of valence electrons n_v. This property has been previously studied for polyatomic [89] and amine [107] molecules and recently verified for adenine [29, 31] ($n_v = 50$) and uracil [30] ($n_v = 42$). Figure 6.14 illustrates the TICS of these molecules as a function of the number of valence electrons at 2 MeV proton impact, together with the present TICS for THF ($n_v = 30$). The dashed line represents the results of linear regression (with intercept zero). The fit was obtained by weighting the data points with the inverse square of the uncertainties. The slope of the fitted line is $(0.090 \pm 0.005) \times 10^{-16}\,\mathrm{cm}^2$, which is comparable to the value of $0.094 \times 10^{-16}\,\mathrm{cm}^2$ given by Itoh et al. in their work [30].

Chapter 7

Conclusions and Outlook

This thesis deals with an experimental determination of cross sections for proton-impact ionization of DNA constituents. The investigated molecules were pyrimidine, tetrahydrofuran, and trimethyl phosphate, which are structural analogues to the nucleic bases, the sugar and the phosphate residue of the DNA back bone, respectively. The experiments were based on the principle of a double-differential measurement using crossed-beam geometry, where the proton beam intersects the target gas jet perpendicularly in a high-vacuum chamber.

The primary energy of the proton beam ranged from 75 keV to 135 keV, covering energies within the Bragg peak region. Delivery of the proton beam was accomplished with the construction of a 155 kV laboratory accelerator [80] and the development of a control system for the beamline of this low-energy ion accelerator. This system realized the features of remote controlling to the beamline components during the measurement, including monitoring the ion beam as well as setting up the operating parameters of the ion source and the accelerator. For tetrahydrofuran, measurements were extended to higher primary proton energies between 300 keV and 3000 keV. The proton beam at these higher energies was generated by a 3.75 MV Van de Graaff generator at the PTB ion accelerator facility [67].

Electron spectroscopy technique was used to detect the secondary electrons ejected from proton collisions. An electron spectrometer, equipped with a hemispherical electrostatic analyzer, was mounted on a rotation stage such that it could be positioned around the axis of the gas jet at any angle. The energy spectra of secondary electrons were recorded at observation angles which ranged from 15° to 135° in steps of 15° relative to the direction of incident proton beam. Measurements at 150° were also obtained for higher proton energies of 300 keV and above. These spectra were converted indirectly into absolute values of experimental DDCS by means of literature cross section data [22, 53, 82].

Experimental cross section data were compared with several theoretical models [23, 25, 27]. For proton energies between 75 keV and 135 keV, the quantum mechanical CB1 calculation [27] agreed well with the measured DDCS, but underestimated the cross sections in the backward direction and at small angles where the two-center effects play a role. The HKS model [23]

was found to be reliable only for DDCS in the vicinity of the binary encounter peak. At proton energies between 300 keV and 3000 keV, both of the HKS and DRF models [23, 25] reproduced the general trends exhibited by the experimental DDCS. The DRF calculation showed a better agreement with the experimental results than HKS model in the region of binary peak and for small angles. The deviation from measured values exhibited by the HKS model indicates that the use of atomic models for a complex target is insufficient for reproducing the experimental DDCS. The DRF model, however, also failed for large emission angles. This underestimation of experimental DDCS by theoretical models is due to the simplified description of the backscattering process close to the nucleus.

SDCS were obtained by integration of DDCS over all emission angles. As the SDCS were governed by low-energy electrons from soft collisions, the differences in backward scattering observed in the DDCS play a minor role here. Thus, better agreement of the experimental data with theoretical models [23, 24, 27] were observed for SDCS within the experimental uncertainties. A further integration of SDCS over the electron energies yields TICS. Experimental results of TICS showed an acceptable agreement with several theoretical calculations [1, 23, 24, 27] over the entire range of proton energy.

The scalability of cross sections in terms of the number of valence shell electrons was also investigated. For experimental DDCS, this is achieved by comparing the angular distribution of THF with that of a single target such as molecular hydrogen [108] as well as with that of a variety of polyatomic molecules [29–31, 47, 106]. While the DDCS data of molecular hydrogen were similar only near the binary peak, the data of other polyatomic molecules containing THF for proton energies above 420 keV scaled fairly over a wide range of the emission angles, despite differences in the individual chemical structures of molecules.

According to few experimental investigations [29–31, 47, 106–108], the scaling property of SDCS seems valid for proton impact at MeV energies. For lower proton energies, it was found that the SDCS data of THF were scalable to those of TMP and PY at 75 keV and 135 keV protons, but not those of uracil [30] at 0.5 MeV. Therefore, it may be questionable to apply the scaling procedure at low proton energies.

At 2 MeV, the TICS of various molecules [30, 31, 48, 89, 107] containing THF confirmed the scaling law [89], which means that the TICS linearly increases with the number of weakly bound electrons. This is due to the fact that the largest contribution to the ionization cross sections is from collisions between protons and valence shell electrons.

A future extension of this work would include the measurements of other DNA constituents such as purine, which is the precursor of nucleobases adenine and guanine. Furthermore, not only proton-collision cross sections, but also cross section data for the interaction of other light ions such as carbon ions with DNA constituents are also urgently required to improve the accuracy of track structure simulations for carbon beam cancer therapy. The experimental setup used in this work, in particular the 155 kV ion accelerator, would be suitable to deliver an incident beam of other light ions in order to conduct such measurements.

References

[1] N. Stolterfoht, R. D. DuBois, and R. D. Rivarola, *Electron emission in heavy ion-atom collisions*. Springer Science & Business Media, 1997, vol. 20.

[2] M. Rudd, Y.-K. Kim, T. Märk, J. Schou, N. Stolterfoht, and L. Toburen, *Secondary Electron Spectra from Charged Particle Interactions*. Bethesda: International Commission on Radiation Units and Measurements, 1996, no. 55.

[3] E. Rutherford, "The scattering of α and β particles by matter and the structure of the atom," *Philos. Mag. Series 6*, vol. 21, no. 125, pp. 669–688, 1911.

[4] M. Gryziński, "Classical theory of electronic and ionic inelastic collisions," *Phys. Rev.*, vol. 115, no. 2, p. 374, 1959.

[5] R. Abrines and I. Percival, "Classical theory of charge transfer and ionization of hydrogen atoms by protons," *Proc. Phys. Soc.*, vol. 88, no. 4, p. 861, 1966.

[6] H. Bethe, "Zur Theorie des Durchgangs schneller Korpuskularstrahlen durch Materie," *Ann. Phys.*, vol. 397, no. 3, pp. 325–400, 1930.

[7] I. Cheshire, "Continuum distorted wave approximation; resonant charge transfer by fast protons in atomic hydrogen," *Proc. Phys. Soc.*, vol. 84, no. 1, p. 89, 1964.

[8] D. Belkic, "A quantum theory of ionisation in fast collisions between ions and atomic systems," *J. Phys. B*, vol. 11, no. 20, p. 3529, 1978.

[9] D. Crothers and J. McCann, "Ionisation of atoms by ion impact," *J. Phys. B*, vol. 16, no. 17, p. 3229, 1983.

[10] E. Blauth, "Zur Energieverteilung der von Protonen in Gasen ausgelösten Sekundärelektronen," *Z. Phys.*, vol. 147, no. 2, pp. 228–240, 1957.

[11] D. E. Moe and O. H. Petsch, "Energy spectrum of electrons emitted from gases bombarded by positive ions," *Phys. Rev.*, vol. 110, no. 6, p. 1358, 1958.

[12] C. Kuyatt and T. Jorgensen Jr., "Energy and angular dependence of the differential cross section for production of electrons by 50–100 keV protons in hydrogen gas," *Phys. Rev.*, vol. 130, no. 4, p. 1444, 1963.

[13] M. E. Rudd and T. Jorgensen Jr., "Energy and angular distribution of electrons ejected from hydrogen and helium gas by protons," *Phys. Rev.*, vol. 131, no. 2, p. 666, 1963.

[14] M. Rudd, C. Sautter, and C. Bailey, "Energy and angular distributions of electrons ejected from hydrogen and helium by 100- to 300-keV protons," *Phys. Rev.*, vol. 151, no. 1, p. 20, 1966.

[15] M. E. Rudd, T. Jorgensen Jr., and D. Volz, "Electron energy spectrum from Ar^+-Ar and H^+-Ar collisions," *Physical Review*, vol. 151, no. 1, p. 28, 1966.

[16] N. Stolterfoht, "Angular and energy distribution of electrons produced by 200–500 keV protons in gases," *Z. Phys.*, vol. 248, no. 1, pp. 81–91, 1971.

[17] L. Toburen, "Distributions in energy and angle of electrons ejected from molecular nitrogen by 0.3- to 1.7-MeV protons," *Phys. Rev. A*, vol. 3, no. 1, p. 216, 1971.

[18] M. E. Rudd, Y.-K. Kim, D. Madison, and T. J. Gay, "Electron production in proton collisions with atoms and molecules: energy distributions," *Rev. Mod. Phys.*, vol. 64, no. 2, p. 441, 1992.

[19] H. Rabus, H. Palmans, G. Hilgers, P. Sharpe, M. Pinto, C. Villagrasa, H. Nettelbeck, D. Moro, A. Pola, S. Pszona *et al.*, "Biologically weighted quantities in radiotherapy: an EMRP joint research project," *EPJ Web Conf.*, vol. 77, p. 00021, 2014.

[20] H. Palmans, H. Rabus, A. Belchior, M. Bug, S. Galer, U. Giesen, G. Gonon, G. Gruel, G. Hilgers, D. Moro *et al.*, "Future development of biologically relevant dosimetry," *Br. J. Radiol.*, vol. 88, no. 1045, p. 20140392, 2014.

[21] P. de Vera, "Charged particle interaction with biological materials: modelling and application to ion beam cancer therapy," Ph.D. dissertation, Universidad de Alicante, 2016.

[22] M. U. Bug, "Nanodosimetric particle track simulation in water and DNA media," Ph.D. dissertation, University of Wollongong, 2014.

[23] M. Bernal and J. Liendo, "The HKS model for electron production in liquid water by light ions," *Nucl. Instr. Meth. Phys. Res. B*, vol. 251, no. 1, pp. 171–176, 2006.

[24] P. de Vera, R. Garcia-Molina, I. Abril, and A. V. Solov'yov, "Semiempirical model for the ion impact ionization of complex biological media," *Phys. Rev. Lett.*, vol. 110, no. 14, p. 148104, 2013.

[25] P. de Vera, R. Garcia-Molina, and I. Abril, "Angular and energy distributions of electrons produced in arbitrary biomaterials by proton impact," *Phys. Rev. Lett.*, vol. 114, no. 1, p. 018101, 2015.

[26] C. Champion, H. Lekadir, M. Galassi, O. Fojón, R. Rivarola, and J. Hanssen, "Theoretical predictions for ionization cross sections of DNA nucleobases impacted by light ions," *Phys. Med. Biol.*, vol. 55, no. 20, p. 6053, 2010.

[27] C. Champion, J. Hanssen, and R. D. Rivarola, "The First Born Approximation for Ionization and Charge Transfer in Energetic Collisions of Multiply Charged Ions with Water," *Adv. Quantum Chem.*, vol. 65, pp. 269–313, 2013.

[28] J. Tabet, S. Eden, S. Feil, H. Abdoul-Carime, B. Farizon, M. Farizon, S. Ouaskit, and T. Märk, "Absolute total and partial cross sections for ionization of nucleobases by proton impact in the Bragg peak velocity range," *Phys. Rev. A*, vol. 82, no. 2, p. 022703, 2010.

[29] Y. Iriki, Y. Kikuchi, M. Imai, and A. Itoh, "Absolute doubly differential cross sections for ionization of adenine by 1.0-MeV protons," *Phys. Rev. A*, vol. 84, no. 3, p. 032704, 2011.

[30] A. Itoh, Y. Iriki, M. Imai, C. Champion, and R. Rivarola, "Cross sections for ionization of uracil by MeV-energy-proton impact," *Phys. Rev. A*, vol. 88, no. 5, p. 052711, 2013.

[31] Y. Iriki, Y. Kikuchi, M. Imai, and A. Itoh, "Proton-impact ionization cross sections of adenine measured at 0.5 and 2.0 MeV by electron spectroscopy," *Phys. Rev. A*, vol. 84, no. 5, p. 052719, 2011.

[32] D. Schardt, T. Elsässer, and D. Schulz-Ertner, "Heavy-ion tumor therapy: physical and radiobiological benefits," *Rev. Mod. Phys.*, vol. 82, no. 1, p. 383, 2010.

[33] W. H. Bragg and R. Kleeman, "XXXIX. On the α particles of radium, and their loss of range in passing through various atoms and molecules," *Philos. Mag. Ser. 6*, vol. 10, no. 57, pp. 318–340, 1905.

[34] R. R. Wilson, "Radiological use of fast protons," *Radiology*, vol. 47, no. 5, pp. 487–491, 1946.

[35] E. Fokas, G. Kraft, H. An, and R. Engenhart-Cabillic, "Ion beam radiobiology and cancer: time to update ourselves," *BBA Reviews on Cancer*, vol. 1796, no. 2, pp. 216–229, 2009.

[36] G. Hilgers, M. U. Bug, E. Gargioni, and H. Rabus, "Secondary ionisations in a wall-less ion-counting nanodosimeter: quantitative

analysis and the effect on the comparison of measured and simulated track structure parameters in nanometric volumes," *Eur. Phys. J. D*, vol. 69, no. 10, pp. 1–18, 2015.

[37] M. Scholz, "Heavy ion tumour therapy," *Nucl. Instr. Meth. Phys. Res. B*, vol. 161, pp. 76–82, 2000.

[38] B. F. Hasson, D. Yeung, and J. Palta, "Bragg peak," in *Encyclopedia of Radiation Oncology*. Springer, 2013, pp. 63–64.

[39] H. O. Wyckoff, *Stopping Powers and Ranges for Protons and Alpha Particles*. Bethesda: International Commission on Radiation Units and Measurements, 1993, no. 49.

[40] H. Nikjoo, "Radiation track and DNA damage," *Iran. J. Radiat. Res.*, vol. 1, no. 1, pp. 3–16, 2003.

[41] S. Incerti, G. Baldacchino, M. Bernal, R. Capra, C. Champion, Z. Francis, P. Guèye, A. Mantero, B. Mascialino, P. Moretto *et al.*, "The Geant4-DNA project," *Int. J. Model. Simul. Sci. Comput.*, vol. 1, no. 02, pp. 157–178, 2010.

[42] M. U. Bug, H. Rabus, and A. B. Rosenfeld, "Electron emission from amorphous solid water after proton impact: Benchmarking PTra and Geant4 track structure Monte Carlo simulations," *Radiat. Phys. Chem.*, vol. 81, no. 12, pp. 1804–1812, 2012.

[43] J. D. Watson and F. H. C. Crick, "Molecular structure of nucleic acids," *Nature*, vol. 171, no. 4356, pp. 737–738, 1953.

[44] M. Chaplin, "Do we underestimate the importance of water in cell biology?" *Nat. Rev. Mol. Cell Biol.*, vol. 7, no. 11, pp. 861–866, 2006.

[45] D. T. Goodhead, "Initial events in the cellular effects of ionizing radiations: clustered damage in DNA," *Int. J. Rad. Biol.*, vol. 65, no. 1, pp. 7–17, 1994.

[46] J. G. Watterson, "The role of water in cell architecture," *Mol. Cell. Biochem.*, vol. 79, no. 2, pp. 101–105, 1988.

[47] L. Toburen and W. Wilson, "Energy and angular distributions of electrons ejected from water vapor by 0.3–1.5 MeV protons," *J. Chem. Phys.*, vol. 66, no. 11, pp. 5202–5213, 1977.

[48] M. E. Rudd, T. Goffe, R. DuBois, and L. Toburen, "Cross sections for ionization of water vapor by 7–4000-keV protons," *Phys. Rev. A*, vol. 31, no. 1, p. 492, 1985.

[49] M. Bolorizadeh and M. E. Rudd, "Angular and energy dependence of cross sections for ejection of electrons from water vapor. I. 50–2000-eV electron impact," *Phys. Rev. A*, vol. 33, no. 2, p. 882, 1986.

[50] M. Bolorizadeh and M. E. Rudd, "Angular and energy dependence of cross sections for ejection of electrons from water vapor. II. 15–150-keV proton impact," *Phys. Rev. A*, vol. 33, no. 2, p. 888, 1986.

[51] B. Grosswendt, "Nanodosimetry, from radiation physics to radiation biology," *Radiat. Protec. Dosim.*, vol. 115, no. 1-4, pp. 1–9, 2005.

[52] D. G. Nikjoo, P. O'Neill and M. Terrissol, "Computational modelling of low-energy electron-induced dna damage by early physical and chemical events," *Int. J. Rad. Biol.*, vol. 71, no. 5, pp. 467–483, 1997.

[53] W. Baek, M. Bug, H. Rabus, E. Gargioni, and B. Grosswendt, "Differential elastic and total electron scattering cross sections of tetrahydrofuran," *Phys. Rev. A*, vol. 86, no. 3, p. 032702, 2012.

[54] W. Y. Baek, A. Arndt, M. Bug, H. Rabus, and M. Wang, "Total electron-scattering cross sections of pyrimidine," *Phys. Rev. A*, vol. 88, no. 3, p. 032702, 2013.

[55] W. Baek, M. Bug, and H. Rabus, "Differential elastic electron-scattering cross sections of pyrimidine in the energy range between 20 eV and 1 keV," *Phys. Rev. A*, vol. 89, no. 6, p. 062716, 2014.

[56] B. Rudek, A. Arndt, D. Bennett, M. Wang, and H. Rabus, "Ion induced fragmentation cross sections of DNA constituents," *Eur. Phys. J. D*, vol. 69, no. 10, pp. 1–9, 2015.

[57] A. Arndt, B. Rudek, W. Y. Baek, and H. Rabus, "Measurements of the fragmentation cross sections of pyrimidine and tetrahydrofuran for electron energies of 50 eV, 100 eV and 300 eV," *J. Phys. Conf. Ser.*, vol. 635, no. 7, p. 072076, 2015.

[58] E. Alizadeh, T. M. Orlando, and L. Sanche, "Biomolecular damage induced by ionizing radiation: the direct and indirect effects of low-energy electrons on DNA," *Annu. Rev. Phys. Chem*, vol. 66, pp. 379–398, 2015.

[59] B. Boudaïffa, P. Cloutier, D. Hunting, M. A. Huels, and L. Sanche, "Resonant formation of DNA strand breaks by low-energy (3 to 20 eV) electrons," *Science*, vol. 287, no. 5458, pp. 1658–1660, 2000.

[60] C. König, J. Kopyra, I. Bald, and E. Illenberger, "Dissociative electron attachment to phosphoric acid esters: the direct mechanism for single strand breaks in DNA," *Phys. Rev. Lett.*, vol. 97, no. 1, p. 018105, 2006.

[61] P. Auger, "The Auger effect," *Surf. Sci.*, vol. 48, no. 1, pp. 1–8, 1975.

[62] E. G. Cavalcanti, G. Sigaud, E. Montenegro, and H. Schmidt-Böcking, "Absolute cross sections for multiple ionization of noble gases by swift proton impact," *J. Phys. B*, vol. 36, no. 14, p. 3087, 2003.

[63] W. Wien, "Untersuchungen über die electrische Entladung in verdünnten Gasen," *Ann. Phys.*, vol. 301, no. 6, pp. 440–452, 1898.

[64] R. Brun and F. Rademakers, "ROOT—an object oriented data analysis framework," *Nucl. Instr. Meth. Phys. Res. A*, vol. 389, no. 1, pp. 81–86, 1997.

[65] O. Etzion and P. Niblett, *Event processing in action.* Manning Publications Co., 2010.

[66] R. Böttger, "Energy calibration of the PTB-VdG Accelerator," Physikal.-Techn. Bundesanstalt, Braunschweig, Tech. Rep., 2002.

[67] H. Brede, M. Cosack, G. Dietze, H. Gumpert, S. Guldbakke, R. Jahr, M. Kutscha, D. Schlegel-Bickmann, and H. Schölermann, "The Braunschweig accelerator facility for fast neutron research: 1: Building design and accelerators," *Nucl. Instr. Meth.*, vol. 169, no. 3, pp. 349–358, 1980.

[68] D. Seccombe, S. Collins, and T. Reddish, "The design and performance of an effusive gas source of conical geometry for photoionization studies," *Rev. Sci. Instrum.*, vol. 72, no. 6, pp. 2550–2557, 2001.

[69] C. Edelmann, *Vakuumphysik*. Heidelberg/Berlin: Spektrum Akademischer Verlag, 1996.

[70] V. Schmidt, *Electron spectrometry of atoms using synchrotron radiation*. Cambridge University Press, 1997, vol. 6.

[71] P. M. Mayer, M. F. Guest, L. Cooper, L. G. Shpinkova, E. E. Rennie, D. M. Holland, and D. A. Shaw, "Does tetrahydrofuran ring open upon ionization and dissociation? A TPES and TPEPICO investigation," *J. Phys. Chem. A*, vol. 113, no. 41, pp. 10 923–10 932, 2009.

[72] K. Jousten, Ed., *Wutz Handbuch Vakuumtechnik*. Braunschweig/Wiesbaden: Vieweg Verlag, 2004.

[73] R. Phaneuf, "Ion–Atom Scattering Experiments: Low Energy," in *Springer handbook of atomic, molecular, and optical physics*, D. G. WF, Ed. Springer Science & Business Media, 2006, ch. 64, pp. 943–948.

[74] R. Strattan and F. Young, "Fields in square helmholtz coils," *Appl. Sci. Res. B*, vol. 9, no. 2, pp. 117–124, 1961.

[75] E. M. Purcell, "The focusing of charged particles by a spherical condenser," *Phys. Rev.*, vol. 54, no. 10, p. 818, 1938.

[76] P. Dahl, M. Rodbro, B. Fastrup, and M. Rudd, "Auger spectroscopy on heavy-ion-atom collisions. I. Kinematic effects and apparatus," *J. Phys. B*, vol. 9, no. 9, p. 1567, 1976.

[77] M. O. Krause and J. Oliver, "Natural widths of atomic K and L levels, $K\alpha$ X-ray lines and several KLL Auger lines," *J. Phys. Chem. Ref. Data*, vol. 8, no. 2, pp. 329–338, 1979.

[78] W. Mehlhorn and D. Stalherm, "Die Auger-Spektren der L_2– und L_3–Schale von Argon," *Z. Phys.*, vol. 217, no. 3, pp. 294–303, 1968.

[79] A. Jablonski, F. Salvat, and C. J. Powell, *NIST Electron Elastic-Scattering Cross-Section Database*, 3rd ed. Gaithersburg: National Institute of Standards and Technology, 2010.

[80] B. Rudek, D. Bennett, M. U. Bug, M. Wang, W. Y. Baek, T. Buhr, G. Hilgers, C. Champion, and H. Rabus, "Double differential cross sections for proton induced electron emission from molecular analogues of DNA constituents for energies in the Bragg peak region," *J. Chem. Phys.*, vol. 145, no. 10, p. 104301, 2016.

[81] M. Wang, B. Rudek, D. Bennett, P. de Vera, M. Bug, T. Buhr, W. Y. Baek, G. Hilgers, and H. Rabus, "Cross sections for ionization of tetrahydrofuran by protons at energies between 300 and 3000 keV," *Phys. Rev. A*, vol. 93, no. 5, p. 052711, 2016.

[82] M. Rudd, L. Toburen, and N. Stolterfoht, "Differential cross sections for ejection of electrons from argon by protons," *At. Data Nucl. Data Tables*, vol. 23, no. 5, pp. 405–442, 1979.

[83] M. E. Rudd, "Differential and total cross sections for ionization of helium and hydrogen by electrons," *Phys. Rev. A*, vol. 44, no. 3, p. 1644, 1991.

[84] E. Grusell, U. Isacsson, A. Montelius, and J. Medin, "Faraday cup dosimetry in a proton therapy beam without collimation," *Phys. Med. Biol.*, vol. 40, no. 11, p. 1831, 1995.

[85] M. Gryziński, "Two-particle collisions. I. General relations for collisions in the laboratory system," *Phys. Rev.*, vol. 138, no. 2A, p. A305, 1965.

[86] M. Gryziński, "Classical theory of atomic collisions. I. Theory of inelastic collisions," *Phys. Rev.*, vol. 138, no. 2A, p. A336, 1965.

[87] M. Gryziński, "Two-particle collisions. II. Coulomb collisions in the laboratory system of coordinates," *Phys. Rev.*, vol. 138, no. 2A, p. A322, 1965.

[88] R. Abrines and I. Percival, "A generalized correspondence principle and proton-hydrogen collisions," *Proc. Phys. Soc.*, vol. 88, no. 4, p. 873, 1966.

[89] M. E. Rudd, Y.-K. Kim, D. Madison, and J. Gallagher, "Electron production in proton collisions: total cross sections," *Rev. Mod. Phys.*, vol. 57, no. 4, p. 965, 1985.

[90] M. A. Bernal-Rodriguez, J. A. Liendo *et al.*, "Single ionization of liquid water by protons, alpha particles, and carbon nuclei: Comparative analysis of the continuum distorted wave methodologies and empirical models," *Adv. Quantum Chem.*, vol. 65, pp. 203–229, 2013.

[91] L. Vriens, "Binary-encounter proton-atom collision theory," *Proc. Phys. Soc.*, vol. 90, no. 4, p. 935, 1967.

[92] C. Champion, M. E. Galassi, H. Lekadir, S. Incerti, O. A. Fojón, R. D. Rivarola, and J. Hanssen, "Theoretical ionization and capture cross sections for DNA nucleobases impacted by light ions," *Int. J. Rad. Biol.*, vol. 88, no. 1-2, pp. 62–65, 2012.

[93] M. W. Schmidt, K. K. Baldridge, J. A. Boatz, S. T. Elbert, M. S. Gordon, J. H. Jensen, S. Koseki, N. Matsunaga, K. A. Nguyen, S. Su *et al.*, "General atomic and molecular electronic structure system," *J. Comput. Chem.*, vol. 14, no. 11, pp. 1347–1363, 1993.

[94] B. Bransden and C. Joachain, *Physics of Atoms and Molecules*. London and New York: Longman, 1983.

[95] N. Kishimoto and K. Ohno, "Collision Energy Resolved Penning Ionization Electron Spectroscopy of Azines: Anisotropic Interaction of Azines with He*(2^3S) Atoms and Assignments of Ionic States," *J. Phys. Chem. A*, vol. 104, no. 30, pp. 6940–6950, 2000.

[96] K. Tasaki, X. Yang, S. Urano, S. Fetzer, and P. R. LeBreton, "UV photoelectron and ab initio quantum mechanical characterization of nucleotides: the valence electronic structures of 2'-deoxycytidine 5'-phosphate," *J. Am. Chem. Soc.*, vol. 112, no. 2, pp. 538–548, 1990.

[97] J. Lindhard, "On the properties of a gas of charged particles." *K. Dan. Vidensk. Selsk. Mat. Fys. Medd*, vol. 28, no. 8, pp. 1–57, 1954.

[98] U. Fano, "Penetration of protons, alpha particles, and mesons," *Ann. Rev. Nucl. Sci.*, vol. 13, no. 1, pp. 1–66, 1963.

[99] J. Hansen and L. Kocbach, "Ejection angles of fast delta electrons from K-shell ionisation induced by energetic ions," *J. Phys. B*, vol. 22, no. 3, p. L71, 1989.

[100] L. D. Landau, E. M. Lifshitz, J. Sykes, J. S. Bell, and M. Rose, "Quantum mechanics, non-relativistic theory," *Physics Today*, vol. 11, p. 56, 1958.

[101] R. Ritchie, "Plasma losses by fast electrons in thin films," *Phys. Rev.*, vol. 106, no. 5, p. 874, 1957.

[102] A. Salin, "Ionization of atomic hydrogen by proton impact," *J. Phys. B*, vol. 2, no. 6, p. 631, 1969.

[103] M. Dingfelder, "Cross Secion Calculations in Condensed Media: Charged Particles in Liquid Water," *Radiat. Prot. Dosim.*, vol. 99, no. 1-4, pp. 23–27, 2002.

[104] Z. Tan, Y. Xia, M. Zhao, X. Liu, F. Li, B. Huang, and Y. Ji, "Electron stopping power and mean free path in organic compounds over the energy range of 20–10,000 eV," *Nucl. Instr. Meth. Phys. Res. B*, vol. 222, no. 1, pp. 27–43, 2004.

[105] W. Wolff, H. Luna, L. Sigaud, A. C. Tavares, and E. C. Montenegro, "Absolute total and partial dissociative cross sections of pyrimidine at electron and proton intermediate impact velocities," *J. Chem. Phys.*, vol. 140, no. 6, p. 064309, 2014.

[106] W. Wilson and L. Toburen, "Electron emission from proton-hydrocarbon-molecule collisions at 0.3–2.0 MeV," *Phys. Rev. A*, vol. 11, no. 4, p. 1303, 1975.

[107] D. Lynch, L. Toburen, and W. Wilson, "Electron emission from methane, ammonia, monomethylamine, and dimethylamine by 0.25 to 2.0 MeV protons," *J. Chem. Phys.*, vol. 64, no. 6, pp. 2616–2622, 1976.

[108] L. Toburen and W. Wilson, "Distributions in energy and angle of electrons ejected from molecular hydrogen by 0.3–1.5-MeV protons," *Phys. Rev. A*, vol. 5, no. 1, p. 247, 1972.

[109] W. Cheng, M. E. Rudd, and Y. Hsu, "Differential cross sections for ejection of electrons from rare gases by 7.5–150-keV protons," *Phys. Rev. A*, vol. 39, no. 5, p. 2359, 1989.

List of Publications

[I] W. Y. Beak, A. Arndt, M. U. Bug, H. Rabus, and M. Wang, "Total electron-scattering cross sections of pyrimidine," *Phys. Rev. A*, vol. 88, no. 3, p. 032702, 2013.

[II] M. Wang, B. Rudek, T. Buhr, D. Bennett, G. Hilgers, and H. Rabus, "Cross sections for the ionization of tetrahydrofuran by light ions," *J. Phys. Conf. Ser.*, vol. 635, no. 3, p. 032050, 2015.

[III] T. Buhr, S. Ricz, L. Ábrók, A. Kövér, M. Wang, G. Hilgers, and H. Rabus, "Double differential ionization cross section of tetrahydrofuran for proton impact," *J. Phys. Conf. Ser.*, vol. 635, no. 3, p. 032047, 2015.

[IV] B. Rudek, A. Arndt, D. Bennett, M. Wang, and H. Rabus, "Ion induced fragmentation cross-sections of DNA constituents," *Eur. Phys. J. D*, vol. 69, no. 10, p. 1, 2015.

[V] M. Wang, B. Rudek, D. Bennett, P. de Vera, M. Bug, T. Buhr, W. Y. Baek, G. Hilgers, and H. Rabus, "Cross sections for ionization of tetrahydrofuran by protons at energies between 300 and 3000 keV," *Phys. Rev. A*, vol. 93, no. 5, p. 052711, 2016.

[VI] B. Rudek, D. Bennett, M. U. Bug, M. Wang, W. Y. Baek, T. Buhr, G. Hilgers, C. Champion, and H. Rabus, "Double differential cross sections for proton induced electron emission from molecular analogues of DNA constituents for energies in the Bragg peak region," *J. Chem. Phys.*, vol. 145, no. 10, p. 104301, 2016.

List of Conference contributions

[I] M. Wang, T. Buhr, G. Hilgers, and H. Rabus, “Electron Spectroscopy for Ion Cross-Section Measurement,” International summer school on metrology 2012, Burg Warberg, Germany, 2012

[II] M. Wang, B. Rudek, D. Bennett, M. Bug, T. Buhr, G. Hilgers, and H. Rabus, “Characterization of a new setup for the measurement of cross sections for ionization of DNA constituents by light ions,” German Conference for Research with Synchrotron Radiation, Neutrons and Ion Beams, Bonn, Germany, 2014

[III] M. Wang, D. Bennett, T. Buhr, B. Rudek, G. Hilgers, H. Rabus, “Ionization cross sections of biomolecules by light ions,” 3rd International Conference Radiation Damage in Biomolecular Systems: Nanoscale Insights into Ion-Beam Cancer Therapy, Boppard, Germany, 2014

[IV] M. Wang, B. Rudek, D. Bennett, M. Bug, T. Buhr, G. Hilgers, and H. Rabus, “Ionization cross sections of DNA constituents by light ions," DPG-Frühjahrstagung der Sektion Atome, Moleküle, Quantenoptik und Plasmen, Heidelberg, Germany, 2015

[V] M. Wang, B. Rudek, D. Bennett, M. Bug, T. Buhr, G. Hilgers, and H. Rabus, “Cross sections for the ionization of tetrahydrofuran by light ions,” International summer school on metrology 2015, Drübeck, Germany, 2015

[VI] M. Wang, B. Rudek, D. Bennett, M. Bug, T. Buhr, W. Y. Baek, G. Hilgers, and H. Rabus, “Proton-impact ionization cross sections of tetrahydrofuran measured from 0.3 to 3.0 MeV by electron spectroscopy," DPG-Frühjahrstagung der Sektion Atome, Moleküle, Quantenoptik und Plasmen, Hannover, Germany, 2016

Acknowledgments

I would like to express my deepest thanks to my mentor, Dr. Hans Rabus. Thank you very much for providing productive guidance through my PhD period.

I am extremely grateful to my supervisors at the TU Brauschweig, Prof. Dr. Meinhard Schilling and Prof. Dr. Jochen Litterst, whose care and concern I constantly felt. I would like to thank PD Dr. Frank Ludwig for taking over the chairmanship of the examination committee.

My special thanks goes to Dr. Marion Bug, Dr. Gerhard Hilgers and Dr. Woon Yong Baek for the advice, encouragement and readiness to help at any moment. I am also thankful to the PostDocs in my working group, Dr. Ticia Buhr, Dr. Benedikt Rudek and Dr. Daniel Bennett. Thanks so much for all the useful tips and ideas from countless discussions that we had.

I also want to thank Dr. Pablo de Vera of Open University, Milton Keynes, UK and Dr. Christophe Champion of University of Bordeaux, France for performing the calculations of the DRF and CB1 theories, respectively.

My thanks would not be complete if I did not mention Dr. Heidi Nettelbeck who gave the advice on grammar and stylistics in my thesis. The help with the drawings by Heike Nittmann is greatly appreciated.

I also wish to thank Andreas Pausewang, Wolfgang Helms and Vincent Hahn for the technical support.

A lot of thanks to the colleagues in Department 6.5 and the staff of the PIAF group in Department 6.4 at the PTB Braunschweig.

And foremost, I must acknowledge and give a special thank you to my parents, who unconditionally supported me in every decision. And finally, my loving girlfriend Mingjia, thank you so much for always standing by my side.

Thank you all.